Institut de Physique de l'Université de Neuchâtel (Suisse)

Dynamics of Josephson junctions in a superconducting ring using a 'Three-Coils' technique

Thèse

Présentée à la Faculté des Sciences
de l'Université de Neuchâtel

Pour l'obtention du grade de Docteur ès Sciences

Par

Oscar Jesús Cubero García

En présence du directeur de thèse
Prof. Piero MARTINOLI

et des rapporteurs
Prof. Christophe BALLIF
et
Prof. Jean-Marc TRISCONE

26 Septembre 2007

Université
de Neuchâtel

FACULTE DES SCIENCES
Secrétariat-Décanat de la faculté
- Rue Emile-Argand 11
- CP 158
- CH-2009 Neuchâtel

IMPRIMATUR POUR LA THESE

Dynamics of Josephson Junctions in a superconducting ring using a three-coils technique

Oscar CUBERO GARCIA

UNIVERSITE DE NEUCHATEL

FACULTE DES SCIENCES

La Faculté des sciences de l'Université de Neuchâtel,
sur le rapport des membres du jury

MM. P. Martinoli (directeur de thèse),
C. Ballif,
et J.-M. Tricone (Genève)

autorise l'impression de la présente thèse.

Neuchâtel, le 15 janvier 2008

Le doyen :
F. Kessler

Félix Kessler

■ Téléphone : +41 32 718 21 00 ■ Fax : +41 32 718 21 03 ■ E-mail : secretariat.sciences@unine.ch ■ www.unine.ch/sciences

Contents

Keywords: Superconductivity; Josephson junction; Josephson junctions array; BKT transition; critical current; two-coils technique; tree-coils technique; SQUID; inductive measurements; inductance; photolithography.

Mot clès: Supraconductivité; jonction Josephson; réseaux de jonctions Josephson; transition BKT; courant critique; technique à deux-bobines; technique à trois bobines; SQUID; mesures inductives; inductance; photolithographie.

Summary

The aim of this thesis is to observe the Berezinskii-Kosterlitz-Thouless (BKT) transition on a magnetically shielded array of Josephson Junctions using an inductive technique.

A major component of this work was the design, fabrication and investigation of the dynamics of a Superconductor-Normal-Superconductor (SNS) Josephson junction embedded in a coplanar and gradiometric superconducting coil. The fabrication process involved a series of steps combining different thin film techniques, such as, photolithography, sputtering, Plasma Enhanced Chemical Vapor Deposition (PECVD) and Reactive Ion Etching (RIE). Furthermore, to extract physical magnitudes, namely the sample coil current, we carried out exact calculations of the self and mutual inductances between the coils of the measurement system.

In order to understand the response of our device we started with a lumped circuit model consisting of a Josephson junction in series with a superconducting ring of self inductance L. This model leads to a useful graphical representation which explains qualitatively the principal features of the DC and AC measurements. In particular, it has been demonstrated that the source of the observed dissipation in the AC measurements is a series of jumps in the total flux and a series of hysteresis cycles that the sample undergoes when subjected to an alternating magnetic field.

A lumped circuit model that also takes into account the normal resistance of the junction, and then the dissipation, has been implemented. The numerical solution of the corresponding differential equation is in very good quantitative agreement with the AC measurements.

On the other hand, it was possible, for the first time with a contactless technique, to extract the critical current of a Josephson junction. Two principal features were observed using the device consisting of a single Josephson junction embedded in a superconducting ring. Firstly, a sudden fall in the critical current near the temperature at which dissipation appears, and secondly, a dependence of this transition temperature on the thickness of the junction's normal metal.

Both behaviors were also observed when the single junction was substituted for an array of Josephson junctions. As a result, the possible contribution to dissipation due to the unbinding of vortex-antivortex pairs, as predicted by the BKT theory, may be hidden by the aforementioned dissipation mechanism. No clear signature of the BKT transition was found.

Chapter 1

Introduction

1.1 Motivation

The humble prediction of the Josephson effect in 1962[1], and its experimental verification one year later[2], rose up a new cornerstone in the world of physics. Josephson's effect has contributed not only to the understanding of superconductivity, but it has also broaden our knowledge in quantum physics and statistical mechanics. On the other hand, from an experimental point of view, it has opened new paths through unexplored novel and unique applications in metrology[3], superconducting microelectronics[4] and quantum computation[5]. As well as Ohm's and Faraday's laws inaugurated the first electronic era (the Copper Age), where resistances and loops were the masterpieces of the puzzle, and the discovery of semiconductors materials inaugurated the second electronic era (the Silicon Age), with the transistor as its masterpiece, we can say the third electronic era started with the incredible phenomena of superconductivity, with the humble Josephson junction as its masterpiece.

I am confident that the search for a non-contaminant and mobile energy source will be based on a combination of two great challenges: room temperature superconducting materials and solar energy. It is possible to imagine a world where the electrical energy is efficiently converted from the sun to be stored and transmitted by superconducting wires in order to move little but powerful superconducting motors. It is possible to imagine a world were millions and millions of data are transmitted and manipulated thanks to very fast computers made of trillions and trillions of Josephson junctions. This day, a new age will have started: the Room Temperature Superconducting Material Age.

---

[1]B. D. Josephson, *Possible new effects in superconductive tunnelling*, Phys. Lett. **1**, 251 (1962).

[2]P. W. Anderson and J. M. Rowell, *Probable observation of the Josephson superconducting tunneling effect*, Phys. Rev. Lett. **10**, 230 (1963).

[3]S. P. Benz and C. A. Hamilton, *Application of the Josephson effect to voltage metrology*, IEEE Proc. **92**, 1617 (2004).

[4]www.hypres.com

[5]Y. Makhlin, G. Schon and A. Shnirman, *Quantum-state engineering with Josephson junction devices*, Rev. Mod. Phys. **73**, 357 (2001).

This is then the main motivation of this work, to enlighten a little the path towards that day, like a lot of people did before.

1.2 Historical background

In this work we will deal with Superconductor-Normal-Superconductor (SNS) Josephson junctions which consist of two superconducting electrodes weakly coupled by a normal metal, and therefore with a very low capacitance (overdamped junctions)[6]. In this kind of junctions, the superconducting electrode in contact with the normal metal do influence each other via the proximity effect: "just as superconducting electrons can drift into an adjoining normal conducting layer and make it superconducting, normal electrons can drift into an adjoining superconducting layer and prevent superconductivity"(sic)[7]. Theses weak links are ideal elements to study macroscopic quantum effects in superconductors and allow to understand the way in which the transition from the superconductor to the normal state takes place.

Since 1970, by using photolithographic techniques borrowed from the semiconductor industry, two-dimensional arrays of Josephson junctions (AJJs) have been fabricated, which provide unique and controllable model systems for the experimental investigation of fundamental concepts in condensed matter physics and statistical mechanics: non-linear dynamics, classical or quantum critical behavior, effects due to disorder and geometry, percolation, etc.

Extensive reviews of the work accumulated on AJJs over the last few decades have been written by Newrock *et al.*[8] and by Fazio *et al.*[9], whereas a more specific review focusing on their dynamical aspects, characterized by ac conductance measurements, has been written by Martinoli *et al.*[10].

The group of Prof. P. Martinoli at the University of Neuchâtel, where this work has been developed, has made in the last twenty years original and significant contribution to the physics of classical AJJs. We will focus first on some aspects of their researches in order to describe later the framework of the present work.

The critical behavior of regular AJJs is described by a quasi-long-range order (topological order) at low temperature, with increasing the temperature this topological order is lost due to the formation of vortex-antivortex pairs. As the temperature increases more, more and more pairs of larger and larger separation are present. Above a certain critical temperature, the

[6]Typical normal state resistance and capacitance values are $\sim$10 mΩ and $\sim$1 fF, respectively.

[7]H. Meissner, *Superconductivity of contacts with interposed barriers*, Phys. Rev. **117**, 672 (1962).

[8]R. S. Newrock, C. J. Lobb, U. Geigenmller and M. Octavio, *The two-dimensional physics of Josephson junction arrays*, Sol. State Phys. **54**, 253 (2000).

[9]R. Fazio and H. van der Zant, *Quantum phase transitions and vortex dynamics in superconducting networks*, Phys. Rep. **355**, 235 (2001).

[10]P. Martinoli and Ch. Leemann, *Two dimensional Josephson junction arrays*, J. Low Temp. Phys. **118**, 699 (2000).

Berezinskii-Kosterlitz-Thouless (BKT)[11] transition temperature, a phase transition occurs and free single vortices appear owing to the unbinding of vortex-antivortex pairs.

In *zero magnetic field* the static critical behavior of classical 2D arrays is well understood in the framework of the BKT theory. However, the dynamical aspects of the BKT transition is not so clear after all. From a theoretical point of view, there are two descriptions, both based on a Coulomb gas model, to predict the dynamics of vortex-antivortex pairs: the Ambegaokar-Halperin-Nelson-Siggia (AHNS) theory[12] and the P.Minnhagen (PM) theory[13]. While AHNS predict a power-law behavior with a temperature-dependent exponent, a nonconvetional response, implying anomalous vortex diffusion, emerges from the PM treatment. The AC measurements carried out until now have never reflected the AHNS prediction, while some evidence for nonconventional behavior was found by R. Théron *et al.*[14].

On the other hand, there has always been a discrepancy between predicted and measured BKT transition temperature values. The origin for this discrepancy could be the impossibility of having a genuine zero magnetic field due to the experimental arrangement of the 'Two-Coils' technique, where the excitation and detection coils are placed on the sample. This residual field will induce free vortices which are not taken into account by the theory. The presence of these non-thermally induced vortices leads, seemingly, to a disagreement between theory and experiments. Moreover, and combined with the preceding problem, one has the disorder in the coupling energy of the junctions, which is neither taken into account by the theory. This disorder introduces an unavoidable randomness, whose origin is intrinsic to the fabrication process and the nature of the coupling energy in a SNS junction, with an exponential dependence on the distance between the superconducting electrodes, which transforms weak random variations of the junction geometrical parameters in strong fluctuations of the coupling energy.

Martinoli's group has also carried out AC measurements, down to 10 mK, on aluminum tunnel junction arrays to study the quantum Superconductor-Insulator transition[15]. Unfortunately, the response signal was not only extremely weak, but also exceptionally sensitive to the magnetic field. These early measurements clearly showed the experimental problems to be solved in order to explore, with the "two-coil" technique, the quantum regime of the tunnel junction arrays.

[11] J. M. Kosterlitz and D. J. Thouless, *Ordering, metastability and phase transitions in two-dimensional systems*, J. Phys. C **6**, 1181 (1973).

[12] V. Ambegaokar, B. I. Halperin, D. R. Nelson and E. D. Siggia, *Dynamics of superfluid films*, Phys. Rev. B **21**, 1806 (1980).

[13] P. Minnhagen, *The two-dimensional Coulomb gas, vortex unbinding, and superfluid-superconducting films*, Rev. Mod. Phys. **59**, 1001 (1987).

[14] R. Théron, J. B. Simond, Ch. Leemann, H. Beck, P. Martinoli and P. Minnhagen, *Evidence for nonconventional vortex dynamics in an ideal two-dimensional superconductor*, Phys. Rev. Lett. **71**, 1246 (1993).

[15] H. van der Zant, F. C. Fritschy, W. J. Elion, L. J. Geerligs and J. E. Mooij, *Field-induced superconductor-to-insulator transitions in Josephson-junction arrays*, Phys. Rev. Lett. **69**, 2971 (1992).

1.3 Setting up the problem

As said before, in order to observe the genuine vortex-antivortex dynamics predicted by the different theories, the residual field-induced vortices must be suppressed. This is the main requirement which has been taken into account in conceiving the new experimental set up. Therefore, it is desirable to be able to shield the array from the ambient magnetic field and, at the same time, to be able to perform inductive measurements. We also hope the new experimental set up could eliminate the harmful effects observed on quantum arrays resulting from magnetic interferences to thereby improving the signal to noise ratio of the sample response, which would allow to explore, for the first time, quantum effects on the dynamics of Josephson junctions.

The set up of the new inductive measurement configuration has been a hard task, but also a very exiting experience. In order to achieve the proposed goal we needed to overcome the following challenges: a) it has been necessary to carry out detailed inductances calculations in order to design the optimal sample geometry as well as the excitation-receive coils configuration, b) it has been necessary to implement and test a series of photolithografic and thin film processes in order to fabricate working samples, and c) it has been necessary to take extreme precautions to perform very low temperature and very sensitive measurements.

1.4 Outline of this thesis

Figure 1.1 shows a schematic outlook on the work performed during the last four years. This thesis is organized as follow:

Chapter 2 is devoted to the new "three-coils" technique we have developed. The design of the sample coil geometry and a detailed quantitative analysis of the measurement configuration are presented. Exact calculations and measurements of self and mutual inductances of the "three-coils" set up are also presented. This chapter is important to understand the relationship between the response of the sample and the signal we actually measure.

In *Chapter 3* we present the different stages necessary to fabricate the samples (design of the nine masks, photolithography and thin film processes). In a series of 'experimental notes' we point out the main difficulties we found to achieve our goal: fabricate working samples. Notice that with the same implemented process we are able to fabricate a single Josephson junction (OD), a series of Josephson junctions (1D) or an array of Josephson junctions (2D) embedded in a gardiometric coplanar superconducting coil. This chapter may be useful to someone interested in reproducing the fabrication process.

Chapter 4 is devoted to the study of the dynamics of a Josephson junction in a superconducting coil. The measured data are first interpreted on the basis of a simple physical model. The critical current of the junction is extracted from the experimental data as well as some microscopic parameters of the junction. Finally, detailed numerical calculations are presented and the results are compared with the experiments.

Chapter 5 is devoted to the study of the dynamics of an array of Josephson junctions embedded in a superconducting coil. The experimental data, critical current and an analysis based on the BKT theory are presented.

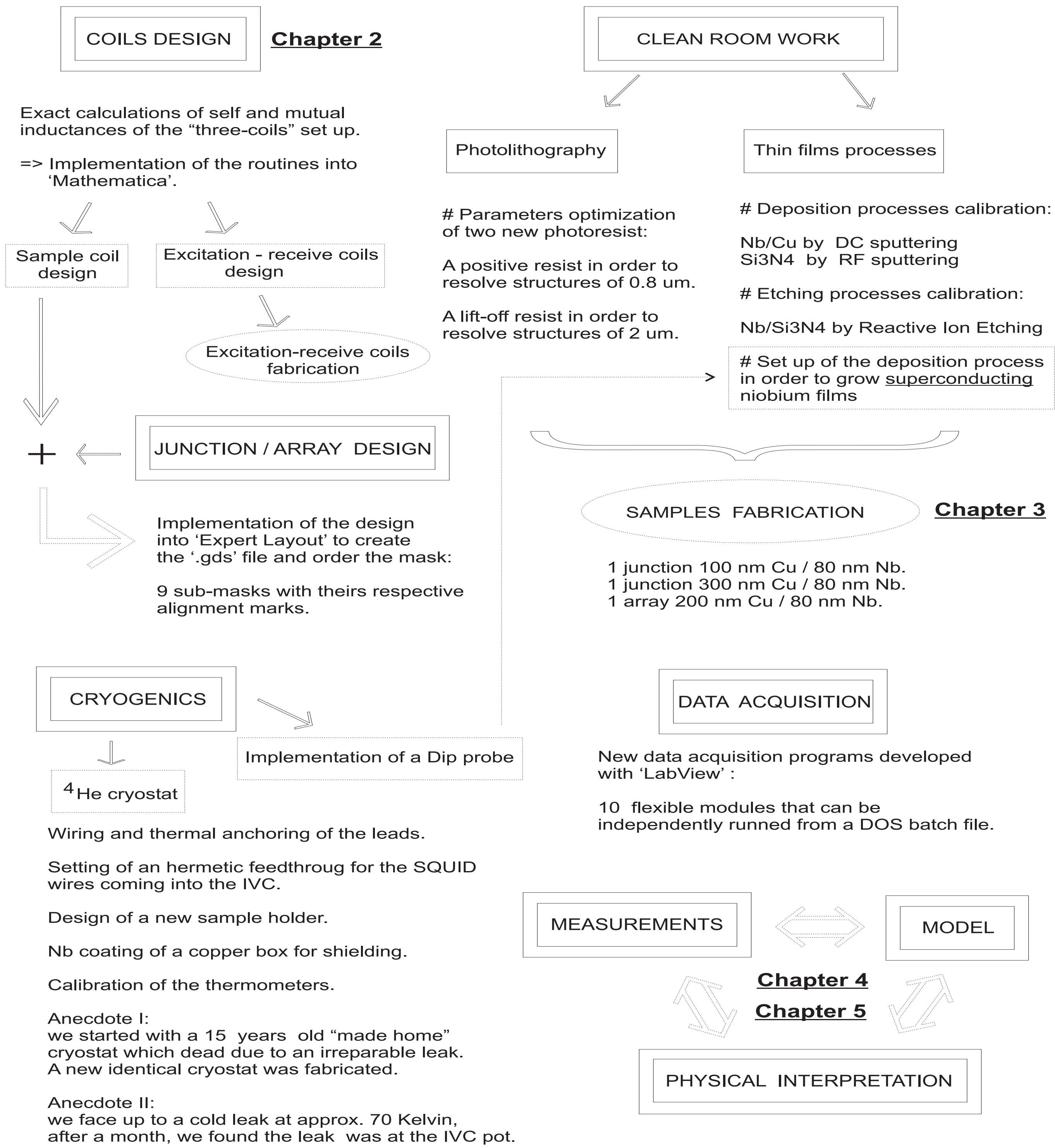

Figure 1.1: Outlook on the work.

Chapter 2

The Three-Coils Technique

2.1 Introduction

The new measurement technique developed in this work is based on the Two-Coils geometry[1] used in the group of Prof. Piero Martinoli to study the physics of two-dimensional systems, namely Josephson junction arrays and high temperature superconducting thin films. This is an inductive technique based on the excitation of the sample by a drive coil and the detection of its response by a receive coil placed directly on the sample.

This measurement technique allows to study the response of the sample not only to AC magnetic fields, but also to *static* magnetic fields, if used in combination with an SQUID. It is thereby possible to study the dynamic response of the sample as a function of a wide range of measuring frequencies. As a last advantage, this inductive technique is contactless, allowing to avoid problems arising from electrical contacts. On the other hand, the only drawback we can mention is its sensitivity to Foucault currents, but fortunately this contribution is only important when the sample is driven with high frequencies.

Despite the fact that the fabrication of the sample becomes more difficult in this new mutual inductance technique owing to the incorporation of an additional gradiometric coil coplanar with the sample, it has the advantage of providing a more direct readout of the sample signal as it is not necessary to unfold a complicated integral relation[2]. As we shall deduce in Sec. 2.4, with this new configuration we are able to establish a direct relationship between the current circulating through the sample loop and the measured signal.

An additional advantage due to the integration of the junction(s) with a coplanar coil is that it allows for the magnetic shielding of the junction(s) from residual magnetic fields. As

[1] A. T. Fiory and A. F. Hebard, AIP Conf. Proc., **58**, 293 (1980). A. F. Hebard and A. T. Fiory, *Evidence for the Kosterlitz-Thouless transition in thin superconducting aluminum films*, Phys. Rev. Lett. **44**, 291, (1980).

[2] B. Jeanneret, J. L. Gavilano, G. A. Racine, Ch. Leemann, and P.Martinoli, *Inductive conductance measurements in two-dimensional superconducting systems*, Appl. Phys. Lett. **55(22)**, 2336 (1989).

mentioned in Chap. 1, this is particularly important for the study of the dynamics of AJJ at *zero magnetic field*.

The fabricated physical system consists of a single Josephson junction[3] embedded in a superconducting loop, which is the basic element of an AC-SQUID. In chapter 4 the physics of this system is presented in detail. For now however the system is considered a "black-box" loop which is able to respond to an external excitation and where the physical quantity of interest is the current flowing through the sample loop.

The aim of this chapter is twofold:

First, to determine the best geometry for the sample coplanar coil.

Second, to extract the current circulating through the sample coplanar coil from the measured signal.

Before discussing the topics above in more detail, we wish to present some notes about self inductances and gradiometers, the kernel of our measurement technique.

2.1.1 Total self inductance

In Appendix A we present expressions to determine the self inductance of a loop and the mutual inductance between two coaxial loops. A question arises: which will be the total self inductance of a system consisting of two loops?

Let us consider the system shown in Fig. 2.1(A) and let us suppose a current is flowing from A to B.

The e.m.f. between A and B can be written as

$$\epsilon_A - \epsilon_B = \epsilon_A - \epsilon_C + \epsilon_C - \epsilon_B = -\frac{d}{dt}\oint \vec{B}_{total} \cdot d\vec{a_1} - \frac{d}{dt}\oint \vec{B}_{total} \cdot d\vec{a_2}$$

where $d\vec{a_1}$ and $d\vec{a_2}$ are unitary vectors perpendicular to the surface. The only magnetic field is the one produced by the current i flowing in the filament, one has then

$$\epsilon_A - \epsilon_B = -\frac{d}{dt}\left[\oint \vec{B}_1 \cdot d\vec{a}_1 + \oint \vec{B}_2 \cdot d\vec{a}_1 + \oint \vec{B}_1 \cdot d\vec{a}_2 + \oint \vec{B}_2 \cdot d\vec{a}_2\right] \equiv -\frac{d}{dt}\Phi_{total} \tag{2.1}$$

where $\vec{B}_1$ and $\vec{B}_2$ are the fields produced by the filaments 1 and 2, respectively. The above equation allows us to identify Φ_{total} with the expression between brackets. On the other hand,

[3]Regarding the results of this chapter nothing changes if we replace the Josephson junction by an array of Josephson junctions.

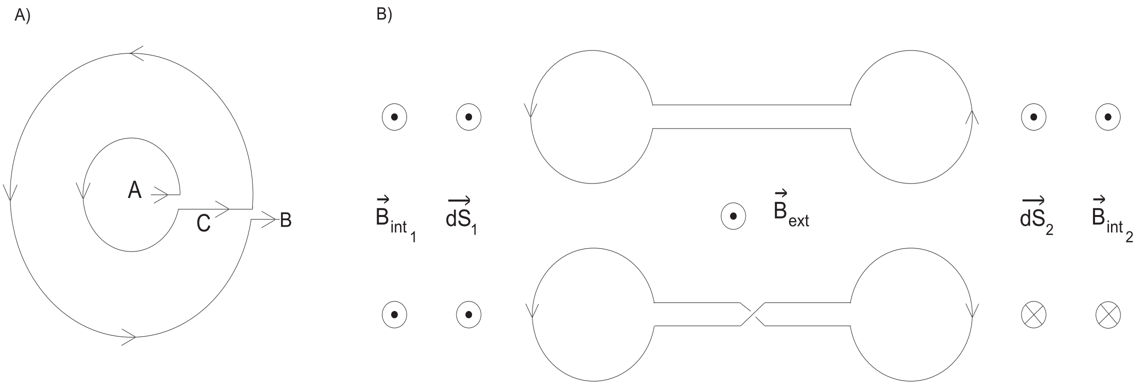

Figure 2.1: A) Geometry used to determine the total inductance of two loops. B) Geometry used to determine the total flux through a gradiometric configuration (bottom).

the total self inductance is defined by $\Phi_{total} = L_{total}\ i$, and if we consider, without loss of generality, a current of one ampere we will have

$$L_{total} = \Phi_{total} = \underbrace{\oint \vec{B}_1 \cdot d\vec{a}_1}_{L_{11}} + \underbrace{\oint \vec{B}_2 \cdot d\vec{a}_1}_{L_{21}} + \underbrace{\oint \vec{B}_1 \cdot d\vec{a}_2}_{L_{12}} + \underbrace{\oint \vec{B}_2 \cdot d\vec{a}_2}_{L_{22}} \tag{2.2}$$

We can note that L_{ii} is always positive because a change in the direction of the current and then in $d\vec{a}$ implies also a change in the vector $\vec{B}$. However, this is not the case for L_{ij}, whose sign depends on the relative direction of the currents; it is positive if both currents flow in the same direction, otherwise is negative. On the other hand, $L_{ij} = L_{ji}$, which is evident if we remember the Neumann's expression [A.16] for the mutual inductance.

In summary, the self inductance of a system of loops is written like

$$L_{total} = \sum_{i,j=1}^{N} L_{ij} = \sum_{i=1}^{N} L_{ii} + 2\sum_{j>i}^{N} L_{ij}. \tag{2.3}$$

If one considers that the N loops are coincident we shall have $L_{ii} = L_{ij}\ \ \forall i, j$ which leads to the familiar expression $L_{total} = N^2 L_{11}$.

2.1.2 Effective self inductance

Let us consider a loop with a self inductance L. What will be the effect of bringing closer another loop?

The answer depends on whether the loop that we are bringing closer is able or not to carry out a current, that is, if it is closed or open. Let us imagine we want to measure the self inductance of a loop. To do that, the loop is fed with an alternating current i(t), which produces a flux $\Phi(t)$, and hence, an e.m.f $\epsilon = -\frac{d\Phi(t)}{dt} = -L\frac{di(t)}{dt}$ is induced; from which we can get L. But, if there is near by another closed loop this one will react according to the Faraday-Lenz's law to compensate the flux produced by the first loop. As a result of that, the flux through the first loop will decrease, and because of the relation $\Phi(t) = Li(t)$ (we have not changed the excitation current) it is equivalent to consider that the self inductance of the loop we are measuring has "decreased". It is usual then, when one wants to consider this effect, to talk about an *effective* self inductance.

Let be L_1 the self inductance of the loop 1 when the loop 2 is open. Once the later loop is closed the flux through it will be $M\ i(t)$, where M is the mutual inductance, hence the corresponding current in the loop 2 will be $\frac{M\ i(t)}{L_2}$ which, in its turn, will produce a flux $\frac{M\ i(t)}{L_2}M$ through the loop 1. Hence, the total flux through the loop 1 in response to the current $i(t)$ can be written as

$$L_{eff} = L_1 - \frac{M^2}{L_2}. \tag{2.4}$$

The behavior of the loop 1, due to the presence of the loop 2, is like if it had a self inductance L_{eff}. It is also usual to define a coupling parameter $k = \left(1 - \frac{L_{eff}}{L_1}\right)^{1/2}$ and using 2.4 the mutual inductance can be written as $M = k\sqrt{L_1 L_2}$. We remark that this expression is only valid if the second loop has not resistance, like in a superconducting wire.

2.1.3 Gradiometric configuration

Let us consider the configuration shown in Fig. 2.1(B)(up) consisting of two loops with a current I flowing through them. This current produces a magnetic field $\mathbf{B}_{int}$ onto the surface limited by each loop. Let us suppose an uniform external magnetic field $\mathbf{B}_{ext}$ is applied throughout. Under these conditions the total flux through the double loop is

$$\Phi_{total} = \underbrace{\oint \vec{B}_{ext} \cdot d\vec{S}_1}_{\Phi_1 > 0} + \underbrace{\oint \vec{B}_{int_1} \cdot d\vec{S}_1}_{L_1 I > 0} + \underbrace{\oint \vec{B}_{ext} \cdot d\vec{S}_2}_{\Phi_2 > 0} + \underbrace{\oint \vec{B}_{int_2} \cdot d\vec{S}_2}_{L_2 I > 0}. \tag{2.5}$$

We remark that Φ_1 and Φ_2 have the same sign. But now, if one turns over the second loop, see Fig. 2.1(B)(bottom), the total flux converts to

$$\Phi_{total} = \underbrace{\oint \vec{B}_{ext} \cdot d\vec{S}_1}_{\Phi_1 > 0} + \underbrace{\oint \vec{B}_{int_1} \cdot d\vec{S}_1}_{L_1 I > 0} + \underbrace{\oint \vec{B}_{ext} \cdot d\vec{S}_2}_{\Phi_2 < 0} + \underbrace{\oint \vec{B}_{int_2} \cdot d\vec{S}_2}_{L_2 I > 0}, \tag{2.6}$$

hence, the only change has been that Φ_1 and Φ_2 have now opposite sign. Note that the contribution to the total flux due to the magnetic field $\mathbf{B}_{int}$ produced by the current flowing in the loops is always positive. Finally, if both loops have the same area, Φ_1 and Φ_2 cancel each other out, and therefore, there will be no contribution of the external magnetic field on the total flux. It is said both loops are in a gradiometric configuration, *i.e.*, in a configuration that is insensitive to an uniform external magnetic field.

2.2 Design of the gradiometric sample coil

In order to study our system it is necessary to find a way to drive it and to detect its response. In our case, an inductive coupling between the sample loop and the drive and receive coils is implemented. This method however raises the following questions concerning the design of the sample coil and the measurement system:

a) How can we excite the sample and detect its response without the excitation affecting the receive coil?

b) How can we make the sample insensitive to a homogeneous external magnetic field but able to respond to the driven coil?

c) What is the optimal geometrical configuration of the different coils in order to get a maximal sensitivity?

The answers to questions a) and b) can be found in Fig. 2.2. The Josephson junction is connected to a coplanar loop in a gradiometric configuration (2D-gradiometer): on the loops of radii $R_1 = 1\ mm$ and $R_2 = 2\ mm$ the current flows in the same direction but opposite to the one flowing on the loop of radius $R_3 = \sqrt{5}\ mm$. Furthermore, as described in Sec. 2.1.3, the fact that $\pi R_1^2 + \pi R_2^2$ equals πR_3^2 means that the configuration is not sensitive to an homogeneous external magnetic field applied on the surface of the planar gradiometer. The large size of the width of the stripe line (160 μm) and the use of a minimum number of turns lowers the value of the self inductance of the planar gradiometer, see A.3.2. The advantage of having a low self inductance will be understood when the physics of the device is dealt with in Chap. 4. The stripe line marked as 'short circuit' in Fig. 2.2 serves to close the gradiometric loop.

The system is excited through the inner loop R_1 of the coplanar gradiometer by a 3D non-superconducting drive coil placed upon it. The detection is made through another 3D receive superconducting coil in a gradiometric configuration (astatically wound coil) that is placed in the same axis as that of the driving coil. This configuration enables the excitation of the sample without detecting the excitation and, at the same time, allows the detection of the sample response (current flowing in the loop R_1) through the flux coupled to the bottom of the coil of the receive gradiometer. In fact, a signal is picked-up in the absence of the sample due to a small asymmetry in the position of one of the two coils forming the gradiometer; the top coil is shifted 100 μm away from its symmetrical position allowing to have a reference signal at high temperature in order to fix the phase and to normalize the signal.

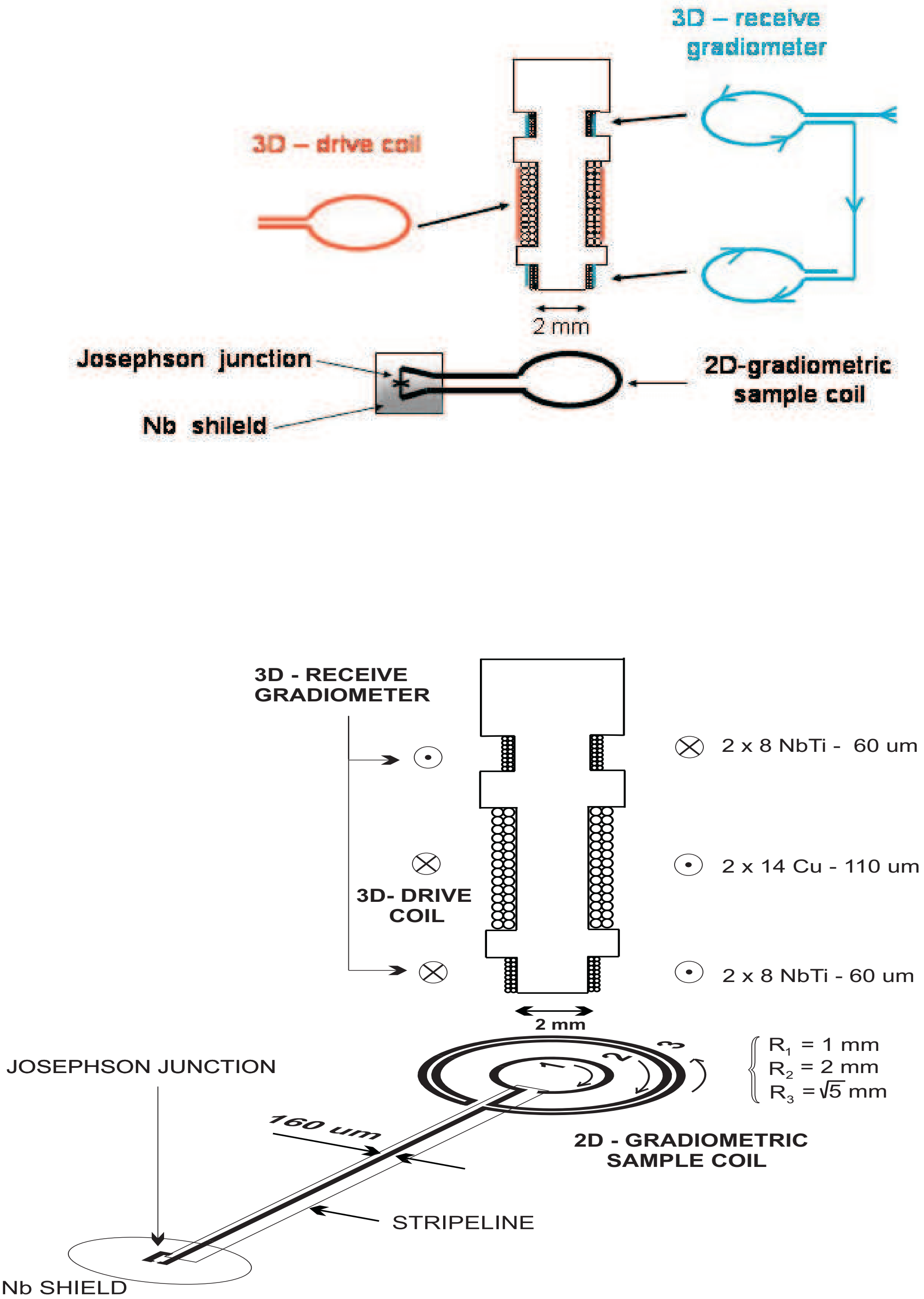

Figure 2.2: Schema of the three-coils configuration: the 3D-drive coil, the 2D-gradiometric sample coil, and the 3D-receive gradiometer.

The drive coil has two layers, each consisting of fourteen turns of 110 μm diameter copper wire. The receive gradiometer also has two layers, each consisting of eight turns of 60 μm Niobium-Titanium superconducting wire[4]. Both coils are wound around a grooved cylinder made of epoxy resin which in turn is embedded in the same resin in order to fix the coils to the cylinder.

2.3 The measurement electrical configuration

In Fig. 2.3 a schematic diagram of the measurement electrical configuration is shown. It allows to measure the response of the sample as a function of temperature and of the amplitude and frequency of the driven magnetic field. It is based on a lock-in detection system which uses an intermediate amplification stage implemented by a RF-SQUID[5]. The lock-in feeds the drive coil with a sinusoidal current which is filtered at room temperature before it enters the cryostat; typical drive current amplitudes in our experiment range between 2 μA and 500 μA with frequencies between 1 Hz and 2 KHz. The lock-in detects, at the driven frequency, the amplitude and the phase difference of the signal at the RF-SQUID. The coupling between the RF-SQUID and the sample is achived by a superconducting transformer which consists of the superconducting receive gradiometer and the RF-SQUID superconducting input coil. The superconducting contact between both coils is assured by screwing the NbTi wire of the receive gradiometer down on two Nb pads which connect to the RF-SQUID input coil. The pair of twisted superconducting wires coming from the receive and excitation coils are screened from external magnetic fields by superconducting PbSn tubes.

The incorporation of a SQUID as an intermediate stage in the measurement system has two advantages. First, the signal from the sample is amplified by a factor which would otherwise be impossible to obtain using an electronic system[6]. Secondly, the incorporation of the SQUID turns the response of the whole measurement system frequency independent. This allows measurements at low frequencies without decreasing the magnitude of the signal and, also simplifies the interpretation of the measurements as a function of the frequency.

2.4 Obtaining the current through the sample coil from the measured signal

In this section the results of Appendix A about inductances calculations, namely expressions A.22 and A.15 for the mutual and self inductance are used. Since we actually deal with coils we have implemented in Mathematica an algorithm to apply the above expressions recursively

[4]The superconductor wire of the gradiometer consists of a 36μm diameter Nb/Ti superconducting filament kernel inside a 50μm diameter copper matrix, which are surrounded by a 5μm thickness insulating layer.

[5]From Quantum Design (www.qdusa.com) with BTI electronics (model 30)

[6]If one considers that a lock-in is able to pick-up signals of the order of a nanovolt, and that the output of the SQUID is about 31 mV for a current of 0.2 μA on its input coil, one finds that it is possible to detect currents as low as 10^{-8} A.

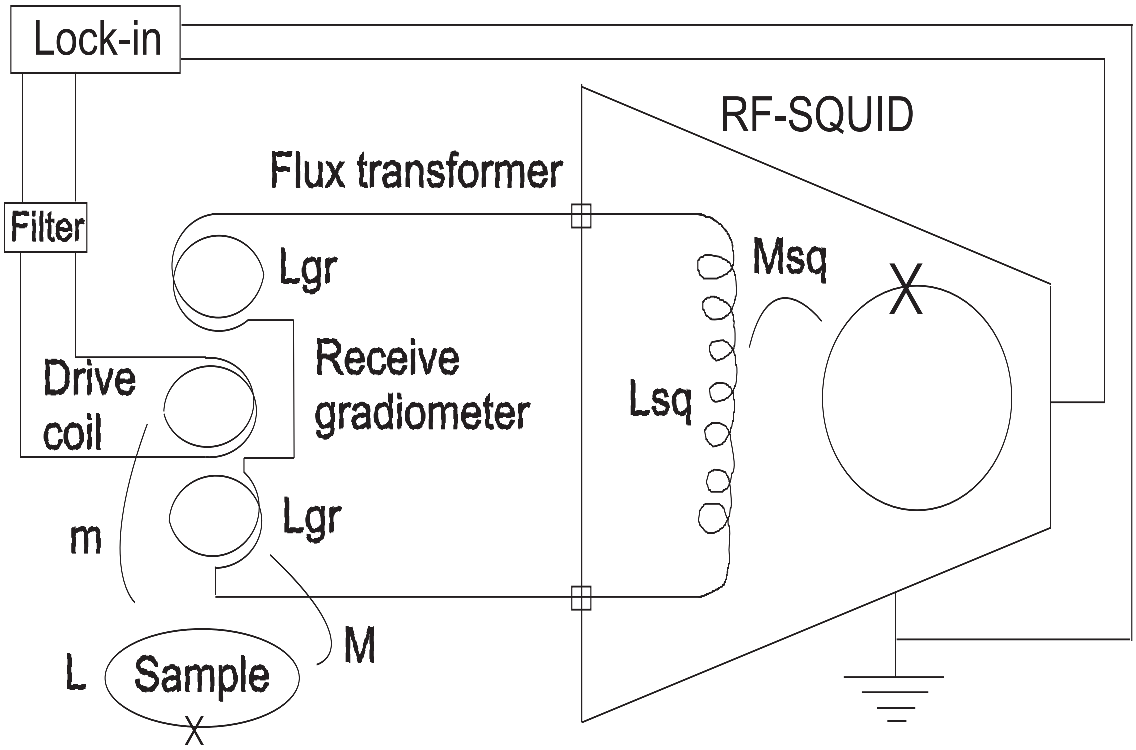

Figure 2.3: Coupling of the 3D receive gradiometer to the RF-SQUID through a flux transformer.

between the turns of the different coils according to Eq. 2.3. Figure 2.4 shows the experimental results for the measured mutual inductance between the coils indicated inside both figures. In both cases, the experimental set up was the same as that used in section A.5: an AC current of 5 mA was used to feed a loop of 2 mm diameter placed under the cylinder where the the excitation and receive coils are located. The experimental mutual inductance is calculated as

$$L_{21} = \frac{b}{2\pi \frac{V_{01}}{R}} = \frac{b}{2\pi\ (5 \times 10^{-3})}, \tag{2.7}$$

where b is the slope of the magnitude versus frequency line. In this way, the measured mutual inductance between the excitation coil and the sample loop[7] was 1.16 nH, that is, a current of 1.7 μA in the excitation coil will produces a flux of one quantum ($\Phi_o = 2.07 \times 10^{-15} Wb$) through the sample loop. Similarly, the measured mutual inductance between the receive gradiometer and the sample loop was 25.9 nH. On the other hand, by taking into account the dimensions for the different coils shown in Fig. 2.2 the calculated values for the mutual inductance between the sample loop and the excitation and receive coils were 1.43 nH and 30.2 nH , respectively. Hence, the measured values are in a good agreement with the calculated values, meaning that we can be confident of both the experimental measurements and the theoretical calculations of

[7]It is a reasonable approximation to neglect the coupling with the two external loops of the coplanar gradiometer if one considers that its effects approximately cancel one another out.

inductances.

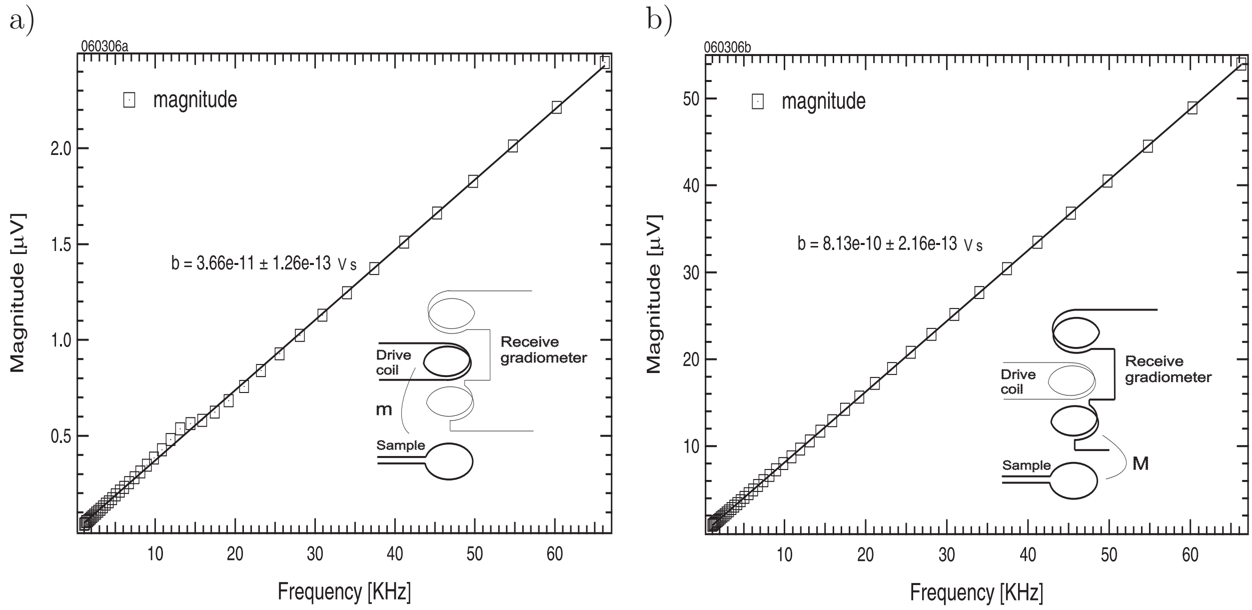

Figure 2.4: a) The measured mutual inductance between the 2 mm diameter sample loop and the drive coil is 1.16 nH. The calculated value is 1.43 nH. b) The measured mutual inductance between the 2 mm diameter sample loop and the receive gradiometer is 25.9 nH. The calculated value is 30.2 nH.

To obtain the self inductance of the gradiometric receive coil we first tried to measure it with an LRC-Measurement System. However this did not give results probably due to the symmetrical configuration of the two coils which cancels the response signal. It was decided that given the good agreement between the calculated and measured values of the mutual inductances, that in this case, the calculated value be used for the self inductance of the gradiometer receive coil, that is, $2 \times 703\ nH = 1.4\ \mu H$.

In order to completely describe the measurement system, the parameters that characterize the RF-Squid itself are required. These are supplied by the manufacturer: the self-inductance of the input coil is 1.84 μH and the mutual inductance between this coil and the integrated squid is 10 nH, which corresponds to a quantum of flux in the SQUID loop for an input coil current of 0.2 μA. Finally, the RF-SQUID supplies a voltage which is proportional to the number of quantum flux through it; this conversion factor can be measured by observing on the oscilloscope the transfer function of the SQUID. The measured conversion factor was[8]

$$\frac{\Delta V_{sq}}{\Delta \Phi_{sq}} = \frac{31\ [mV]}{\Phi_o}. \tag{2.8}$$

Table 2.1 summarizes the above results.

[8]For a sensitivity = 1, this a choice in the electronic set up of the SQUID.

m	M	$2 \times L_{gr}$	L_{sq}	M_{sq}	$\frac{\Delta V_{sq}}{\Delta \Phi_{sq}}$
$1.16\ nH$	$25.9\ nH$	$2 \times 703\ nH$	$1.84\ \mu H$	$10\ nH$	$31\ mV/\Phi_o$
measured	measured	calculated	manufacturer	manufacturer	measured

Table 2.1: Values of the self and mutual inductances corresponding to the coils of Fig. 2.3. The last column is the conversion factor between the number of quantum of flux through the SQUID and its output voltage.

When driven by an external magnetic field the sample reacts by producing a current flowing in the superconducting loop. The question arises: knowing the voltage at the output of the RF-SQUID what is the current in the sample loop? The answer requires us to consider the behavior of the superconductor circuit, namely the fundamental property that the total flux through it is a constant[9]. Then,

$$cte = \Phi_{total} = M\ I_{sa} + 2L_{gr}\ I + L_{sq}\ I, \tag{2.9}$$

where I_{sa} is the current in the sample and I is the current in the flux transformer[10]. If one considers a variation of all quantities involved in Eq. 2.9 one has

$$\Delta I = -\frac{M\ \Delta I_{sa}}{2L_{gr} + L_{sq}}, \tag{2.10}$$

then the flux through the squid is

$$\Delta\Phi_{sq} = M_{sq}\ \Delta I = -M_{sq}\ \frac{M\ \Delta I_{sa}}{2L_{gr} + L_{sq}}, \tag{2.11}$$

and taking into account the conversion factor for the SQUID, see Eq. 2.8, we have

$$\Delta V_{sq} = \frac{31\ [mV]}{\Phi_o}\ \Delta\Phi_{sq} = -\frac{31\ [mV]}{\Phi_o}\ M_{sq}\ \frac{M}{2L_{gr} + L_{sq}}\ \Delta I_{sa}. \tag{2.12}$$

At this point we have two parameters: the mutual inductance M between the sample loop and the receive gradiometer, and its self inductance L_{gr}, which are not independent. By using the algorithm implemented in Mathematica for the calculation of self and mutual inductance between coils we have chosen the geometry for the receive gradiometer in such a way that $\frac{M}{2L_{gr}+L_{sq}}$ is maximum. The geometry that maximizes the sensitivity is the shown in Fig. 2.2.

Substituting the respective values shown in Table 2.1 into Eq. 2.12 we finally obtain

[9] This can be understood if one considers that in a superconducting loop no net voltage can be developed, therefore $0 = RI = V = -\frac{d\Phi}{dt}$, and so $\Phi = cte$.

[10] J. H. Claassen, *Coupling considerations for SQUID devices*, J. Appl. Phys. **46**, 2268 (1975).

$$\frac{1}{K} = \frac{\Delta I_{sa}[\mu A]}{\Delta V_{sq}[mV]} = -0.83, \tag{2.13}$$

which allows us to know the current flowing in the sample from the voltage reading at the RF-SQUID output.

In order to measure not only the magnitude, but also the phase of the signal, a lock-in technique was used. Since the drive coil is fed by the lock-in at a fixed frequency the response of the sample is also time dependent $I_{sa} = I_{sa}(t)$, and as described by the relation 2.13, the RF-SQUID, through the flux transformer, amplifies this signal. After that, its output $V_{sq}(t)$ is read by the lock-in which extracts the in-phase(X_n) and quadrature-phase(Y_n) components of the signal. The product of the lock-in electronic can be expressed as a Fourier Transform, that is

$$V_{sq}(t) = K\ I_{sa}(t) = \frac{X_o}{2} + \sum_{n=1}^{\infty}(X_n \cos(n\omega t) + Y_n \sin(n\omega t), \tag{2.14}$$

where

$$X_n = \frac{2}{T}\int_0^T K\ I_{sa}(t)\cos(n\omega t)dt, \qquad n = 0, 1, 2... \tag{2.15}$$

$$Y_n = \frac{2}{T}\int_0^T K\ I_{sa}(t)\sin(n\omega t)dt, \qquad n = 1, 2... \tag{2.16}$$

X_n and Y_n are just the real and imaginary components measured by the lock-in; $\omega = 2\pi\nu$, where ν is the frequency of excitation and the subindex n corresponds to the order of the detected harmonic. From both components the magnitude and phase are

$$\text{Magnitude}_n(t) = \sqrt{X_n^2 + Y_n^2} \qquad \text{Phase}_n(t) = \arctan\frac{Y_n}{X_n}, \tag{2.17}$$

these values are also measured by the lock-in, and contain the same information that the X_n and Y_n components.

In brief, the different stages the signal is going through are summarized below:

a) DRIVING: a sinusoidal current $I_x(t)$ at a frequency ν is fed through the drive coil which produces a flux $\Phi_x(t)$ on the sample loop. Specifically, a current of 1.7 μA produces a quantum of flux.

b) DEVICE PHYSICS: the sample reacts to the above excitation $\Phi_x(t)$ with a current $I_{sa}(t)$ through the loop.

c) INDUCTIVE DETECTION AND AMPLIFICATION: the current in the sample loop $I_{sa}(t)$ is inductively detected and amplified by the RF-SQUID which finally gives a voltage $K\ I_{sa}(t)$. Specifically, a voltage of 1 mV is detected at the output of the RF-SQUID for a current of 0.83 μA through the sample loop.

d) PHASE SENSITIVE DETECTION: finally, the lock-in makes the Fourier transform of the voltage $K\ I_{sa}(t)$ supplied by the RF-SQUID in order to determine the magnitude and phase difference of the desired harmonic. The first (n=1) harmonic corresponds to the drive frequency.

It is important to keep in mind that although the sample is driven at a fixed frequency its response is generally non linear, and in this case it is not possible to obtain the total current in the sample from only one of the harmonics measured by the lock-in.

2.5 Experimental set-up

The measurements presented in this work were realized in a "home made" ^{4}He cryostat[11]. Except for the computer, the cryostat and the whole electronic equipment was placed in a copper Faraday cage to reduce the effects due to undesirable electromagnetic fields. Moreover, the ambient magnetic field was reduced by using a cylindrical shield of high permeability material ("μ-metal") surrounding the cryostat, additionally an inner lead cylinder was placed in the liquid-He reservoir to provide a superconducting shield against fluctuations in the ambient magnetic field. Last but not least, the sample holder was also surrounded by a "home made" copper box coated with a superconducting niobium film. The leads that go down to the excitation coil were rf filtered at the top of the assembly and consisted of a shielded twisted pair of wires. The main power was also filtered and its earth decoupled from our electronic configuration ground by an isolation transformer in order to prevent ground loops.

The sample is mounted inside an evacuated[12] indium sealed pot (Inner Vacuum Chamber or IVC) on a sapphire plate, which is coupled to the coldplate ("1K pot") by a copper bar on which a heater, made of manganin wire, is wound; the cold and hot sources are weakly decoupled by placing a brass bar between them. The 1K pot is continuously filled with liquid-He through a fixed impedance (capillary) and is connected to a manostat which allows to establish a controlled pressure inside the 1K pot. When it is pumped to a low pressure it is possible to reduce its temperature to approximately 1.3 K[13]. So, with this system, it is possible to perform measurements over a temperature range between 1.3 K and 10 K[14] with a temperature stability better than 1mK for temperatures lower than 4 K. Figure 2.5 demonstrates that we have no leaks in the IVC and that the impedance is working perfectly: after 35 hours of pumping on

[11] L. E. Delong, O. G. Symko and J. C. Wheatley, *Continuously operating ^{4}He evaporation refrigarator*, Rev. Sci. Instr. **42**, 147 (1971).

[12] For this reason, the electrical inputs at the top of the assembly are through vacuum-tight connectors.

[13] To achieve this low temperature the wires entering the IVC are first anchored to its top plate, which has the temperature of the helium bath (4.2 K) and allowing for their thermalization.

[14] This is the critical temperature of the superconducting NbTi wire of the receive graiometer.

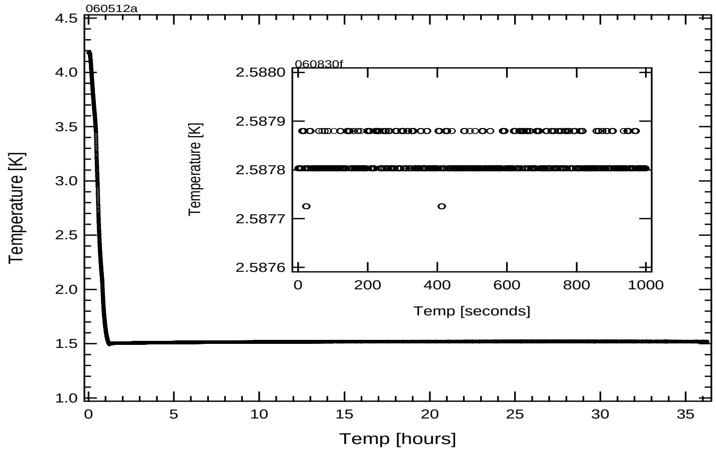

Figure 2.5: Final temperature reached by pumping on the 1K pot, notice that after 35 hours the temperature is maintained at 1.5 K. Inside: typical control temperature accuracy.

the 1K pot the temperature is maintained at 1.5 Kelvin; the inset shows a typical control temperature accuracy. There are two germanium resistance thermometers inside the IVC, one is placed under the 1K pot and the other on the top of the copper box which is thermally linked through three copper bars to the sapphire sample holder. This last thermometer is used to measure and control the temperature of the sample.

2.6 Conclusions

In this chapter we describe the proposed device for fabrication. The device consisted of a Josephson junction embedded in a superconducting coplanar coil. The coil design was based on two criteria: firstly, we wanted a gradiometric configuration making the sample coil insensitive to uniform external magnetic fields; and secondly, its self inductance should be minimal given that we are interested in the energy associated with the junction rather than the coil itself. With these two criteria, and taking into account our investigations about self and mutual inductances, we have concluded that the best geometry consists of a gradiometric coil with a minimal number of turns and with a relatively large stripline.

We also presented the measurement system consisting of a 3D-excitation coil and a 3D-gradiometric detection coil which are placed directly on the coplanar sample coil. We carried out exact calculations of the self and mutual inductances between the different coils in order to extract from the experimental data the physical magnitude we are interested in, that is, the current in the sample coil. These calculations also allowed us to determine the applied flux on the sample coil from the current in the 3D-excitation coil.

Chapter 3

Samples Fabrication

The design and fabrication of the samples was a central issue of the present work. The basic structure of our samples is a single Josephson junction or an array of Josephson junctions[1], consisting of weak links made of copper for the normal (N) bridge, and niobium for the superconducting (S) electrodes, see figure 3.1.

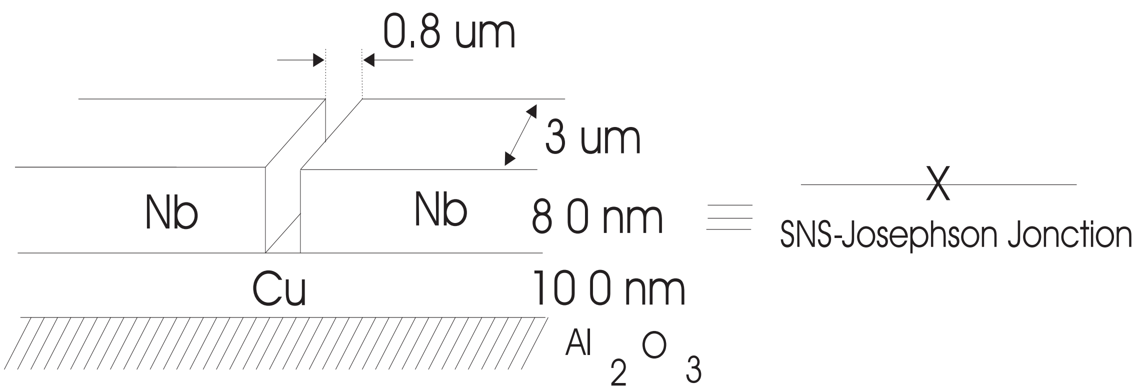

Figure 3.1: Typical geometry and dimensions of the fabricated SNS Josephson junctions.

We have chosen this pair of materials for several reasons. On the one hand, copper has a very low diffusion into niobium[2], which allows us to have a very clean interface, and on the other hand, its low resistivity reduces self-heating problems. Among the elemental superconductors, Nb has a high superconducting transition temperature ($T_c = 9.2\ K$), it is hard, it is stable and has a great tensile strength. As a result, it presents a great resistance to damage by differential thermal contraction on cooling to 1.5 K, which is an important feature for applications. However, it also has one disadvantage: niobium, like Ti and Al, is very reactive, being an excellent

[1]Hereafter, we will restrict ourself to a single Josephson junction, but everything we say will also be valid for an array.

[2][Jang] S.Jang, S.M.Lee, and H.K.Baik, *Tantalum and niobium as a diffusion barrier between copper and silicon*, J.Mater.Sci.:Mater. in Electr. **7**, 271 (1996).

oxygen getter. We will see in Sec. 3.5.3 that oxygen contamination leads to a degradation of the superconducting properties of the film and it is the main difficulty to overcome in order to produce high quality Nb thin films.

We remember that in our device the Josephson junction is short circuited by a superconducting loop. Furthermore, the gradiometric configuration of the loop makes its fabrication more difficult because, at some point, it is necessary to cross the stripline of the loop, see Fig. 2.2. This feature introduces two challenges: first, it is necessary to deposit an insulating film without pinholes, and secondly, it is necessary to make two via holes through the insulating layer, and therefore one has to be able to stop the etching of the insulator just at the Nb interface.

3.1 Design of the mask

Mask pattern is designed by CAD tool programs. We have used the Expert Layout Editor (3.6.0R), which is a robust software used in the semiconductor industry. It generates the standard format GDSII, a binary file used to transfer layout design between different CAD systems and accepted by all the mask making. The main advantage of this format is that it supports a hierarchical library of structures (called "cells"), in this way the modification of the 'parent-cell' automatically modifies all the 'daughter-cells', otherwise, the change of millions of identical structures would be an impossible task. Cells may contain a number of objects, mainly polygons or rectangles; in this format open lines are forbidden and specific rules to form islands are mandatory. We can resume the rules of design by saying that every surface have to be bounded by a continuous line. On the other hand, there are 64 available layers, numbered 0 to 63, each number layer typically representing one mask.

Figure 3.2 tries to shown the mask used in the present work. The mask is subdivided in nine sub-masks, which has allowed us to considerably lower its price. This has been possible because the mask aligner allows us to move the mask in all directions and so to choose the sub-mask needed in each process. The effective area of all sub-masks corresponds to a circle of one inch in diameter, which is the area of the substrate used to make the samples.

We can see there are two types of sub-masks, one mainly transparent and the other blackish. The reason is that we also use two different photoresists: positive and negative, see bellow. On both sides of each sub-mask we can observe the alignment marks, a pair of them is necessary in order to assure rotational alignment. Beside one of the contact pads we can also observe the different structures we have used to find the optimal parameters for the photoresists. Despite the fact the mask aligner does not have micrometer screws in order to do the alignment between the different masks, we have succeeded in manually aligning the marks of micrometer size without difficulty, see Fig. 3.3.

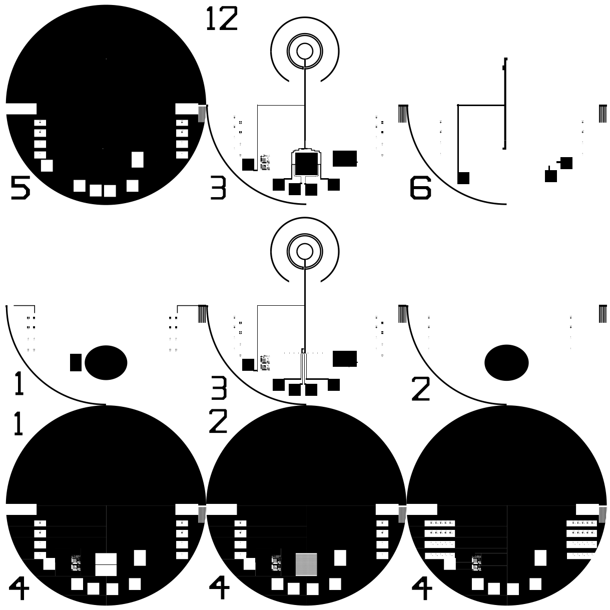

Figure 3.2: Right reading, chrome down mask on 5x5x0.09 inch quartz. The numeration of the corresponding sub-masks is from top to right: 5, 3/12, 6, 1, 3, 2, 4/1, 4/2, and 4.

3.2 Photolithography

Optical lithography is a well established technique used for the transfer of patterns through a mask onto a substrate coated with a photo sensitive resist. It is not the aim of this section to review the theory of this technique. Instead, we will remember briefly some points we consider useful in order to understand the fabrication process we have used.

a) Resists can be either positive or negative. For positive ones the exposed areas are removed by development, while for negative ones the exposed areas remains after development. In the second group we have the Image Reversal resists which are optimized for lift-off, see below.

b) One typical resist processing consists of: 1) the cleaning of the substrate, 2) the spinning of the photoresist on it to get the required thickness, 3) a bake to remove the solvent from the resist, 4) an exposure to UV light through a mask that causes a chemical change in the resist, and finally, 5) the development in an alkaline solution to dissolve it. For Image Reversal resist there are two mandatory additional steps after exposure: a post exposure bake to thermally activate a chemical process (cross-link) and a flood exposure without mask. We can see a sketch of how Image Reversal works in the Fig. 3.4.

In order to transfer a pattern on the substrate we have two ways. Either we can deposit the metal film onto the substrate first, and then pattern the resist for a posterior etching of the undesired metal, or we can use the lift-off technique, which consists of the pattern of the resist first, and the deposition of the metal afterward. The resist is then dissolved in the developer, carrying the unwanted metal with it. Why do we use an Image Reversal resist for lift-off? The reason is that the sidewall slope of a positive resist presents a problem after deposition of the metal: it would form a continuous film and when the resist would be removed the edges of the metal film would lift the pattern off. This problem is overcome in Image Reversal resist because of the cross-link, but most of all, due to an optimization in the sidewall slope that creates an undercut profile, see Fig. 3.5. Finally, we will have to pay attention to the thickness ratio between the resist and the film to avoid, even in this case, the formation of a continuous film.

c) To understand the origin of the sidewall slope it is necessary to talk about two concepts: contrast and diffraction.

The contrast of a photoresist defines the development rate as a function of the absorbed light dose. Figure 3.6 shows two typical curves for both high and low contrast resists. It represents the remaining resist film thickness after development (time fixed), normalized by the thickness before development, as a function of the exposure dose[3]. We observe than even for an exposure dose equal to zero we will have $d' < d_0$ (dark erosion). These curves are only a guide to keep in mind because the result of all the process depends on a great variety of parameters like resist thickness, bake temperature, rehydration, air temperature and humidity, etc.

[3] We remember here the definition for the exposure dose D: $D[\frac{mJ}{cm^2}] = I[\frac{mW}{cm^2}] \times t$, where I is the irradiance of the luminous source.

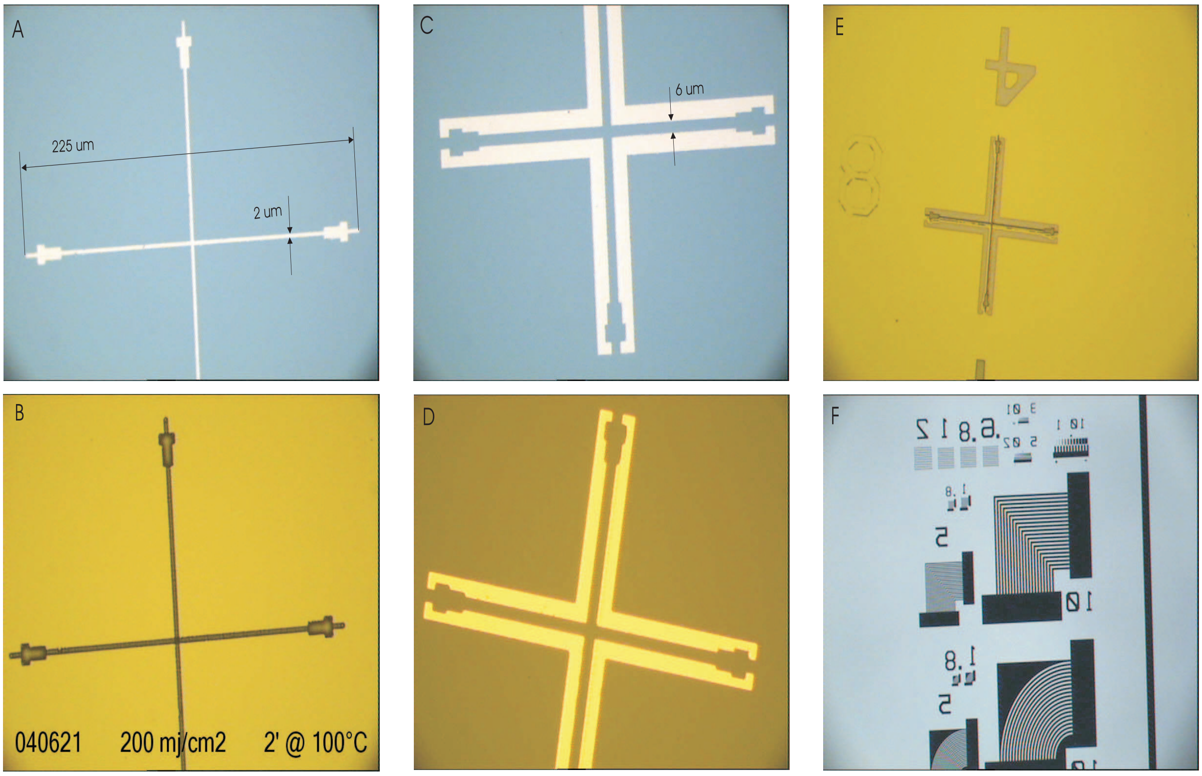

Figure 3.3: A and C: Cr alignment marks on the mask. B and D: alignment marks on the substrate after photolithography. E: alignment made by hand, without using micrometer screws. F: some structures on the mask used to characterize the photoresist.

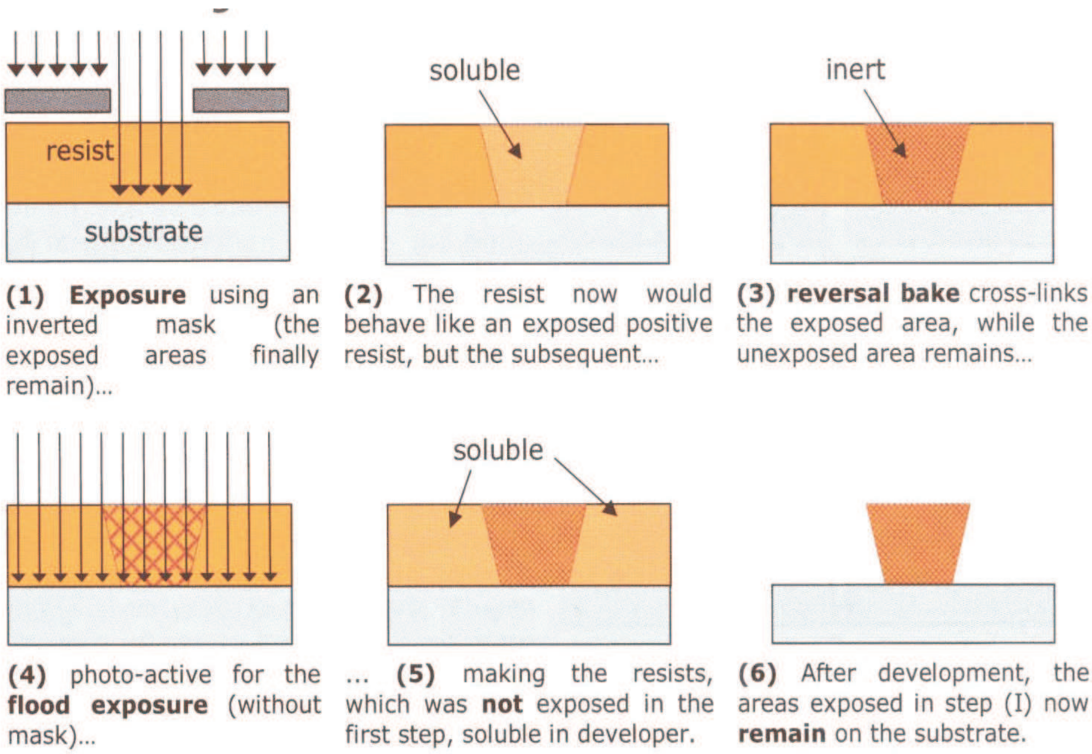

Figure 3.4: How Image Reversal works (taken from the 'Lithography' brochure by MicroChemicals).

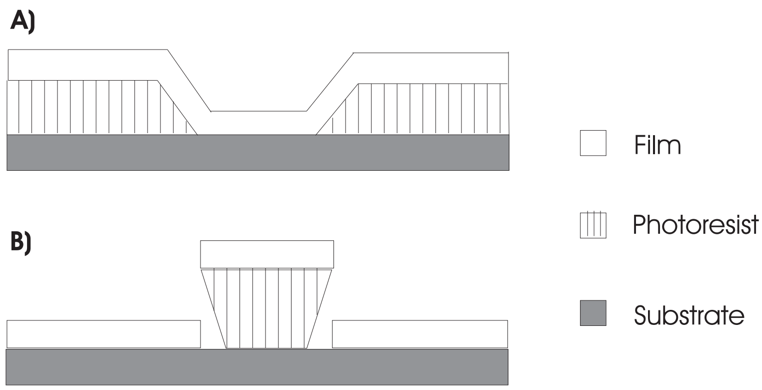

Figure 3.5: Sidewall slope for a positive resist A) and for an Image Reversal resist B).

In contact lithography the mask pattern is transfered directly into the resist (a 1:1 process). Hence, like in all optical processes there will be a fundamental limitation: diffraction. In this case, due to the small separation between the "slit"(mask) and the "screen"(resist on the substrate) we will have to deal with the Fresnel diffraction instead of with the Fraunhofer one. Figure 3.6 shows the diffraction intensity curves for different distances from the mask into the resist.

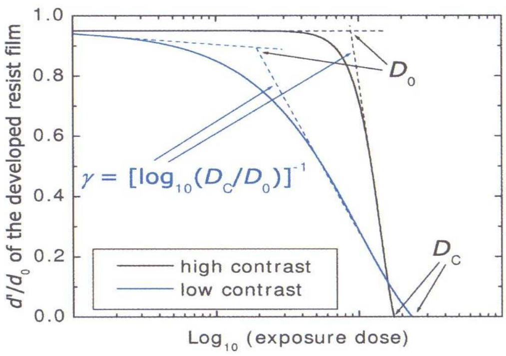

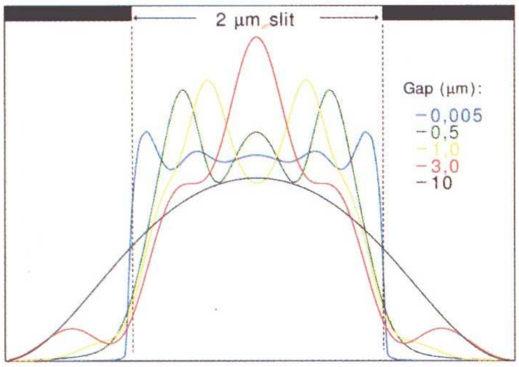

Figure 3.6: Left: Contrast curves. Right: Light intensity distribution on the resist at different deeps (figures taken from the 'Lithography' brochure by MicroChemicals).

We can observe in the diffraction curves that, close to the interface between the exposed an unexposed regions, the resist is gradually less exposed when we move toward the interface. Now, if we use a resist with a low contrast and we do not expose it too much we will also have, in turn, a gradually development rate, and so we will get an optimal sidewall profile for subsequent lift-off. For this reason, Image Reversal resists, thanks to their low contrast, are used for the lift-off process. On the contrary, positive resists will have a high contrast and it will be convenient to expose them sufficiently to have a sharp profile, and so a more exact pattern transfer from the mask.

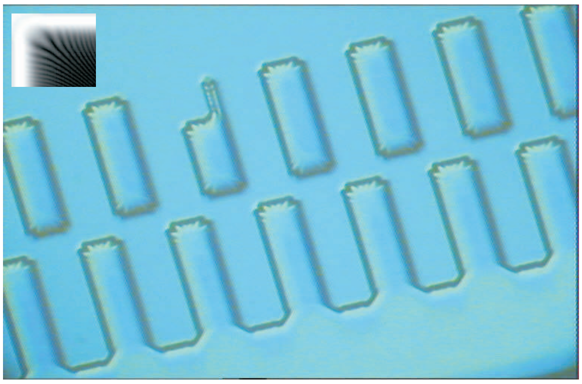

Figure 3.7: Typical diffraction pattern that appears on the corners due to the resist edge bead. In this case, its height was 1 μm. In the inset, a typical simulated Fresnel diffraction.

In order to avoid diffraction problems good contact between the mask and the resist is then desirable. Apart from particulates, the principal factor which prevents perfect contact is the resist edge bead that originates after spinning the resist. Figure 3.7 shows what happens when one does not remove the edge bean. Mask aligners have three modes of contact: soft contact, in which the substrate is brought up until it just makes contact with the mask; hard contact, in which an overpressure of nitrogen pushes the substrate against the mask; and vacuum contact, in which a vacuum seals the substrate to the mask.

d) The optical absorption of an unexposed photoresist matches the emission spectrum of Hg lamps in mask aligners. But once exposed, the photoreaction lowers its UV-absorption and photoresist become almost completely transparent down to approximately 300 nm (bleaching effect). This property allows us to expose thick resist film above 3 μm without any problems. On the other hand, the optical transparency of the photoresist above 460 nm also makes possible to see through it in order to align the substrate and the mask. Figure 3.8 shown typical absorption curves of exposed and unexposed resists and the emission spectrum of different light sources for comparison.

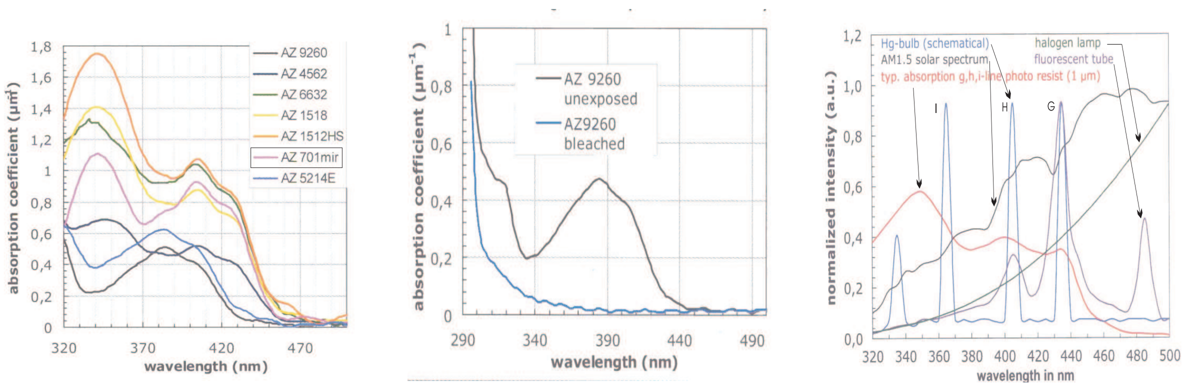

Figure 3.8: *Left*: UV-absorption of unexposed resists. *Center*: Bleaching. *Right*: Emission spectrum of different light sources (figures taken from the 'Lithography' brochure by MicroChemicals).

e) In this work we have used two resists: a positive resist for high resolution down to 0.5 μm, and an Image Reversal resist for lift-off. The first time consuming task was the characterization of both photoresists, that is, the search of all the optimal parameters to reach the two desired goals: first, to be able to resolve sub-micrometer size structures using the positive resist, and secondly, to be able to carry out a lift-off on structures of two micrometers. We have dealt with the following parameters: time and speed of the spinning, bake temperatures, exposure and development times, and water dissolution of the developer. To this end it has been very useful to use the comb structure shown in figure 3.9. Only when the central rectangle is in perfect alignment with the one opposite we can assure an optimal transfer of the pattern on the mask onto the resist. If this is not the case, it also allows us to determine the shifting optically. The minimal shift we can detect in this way is 1 μm, and the maximal is 5 μm.

3.3 Thin film processes

Thin film processes for film deposition and etching are well known since the past 50 years. In these processes the interaction among operating parameters as pressure, temperature, gas composition and flow rate, power level and frequency, electrodes configuration and its separation, chamber geometry, gas chemistry, etc, is rather complicate and in some cases not fully

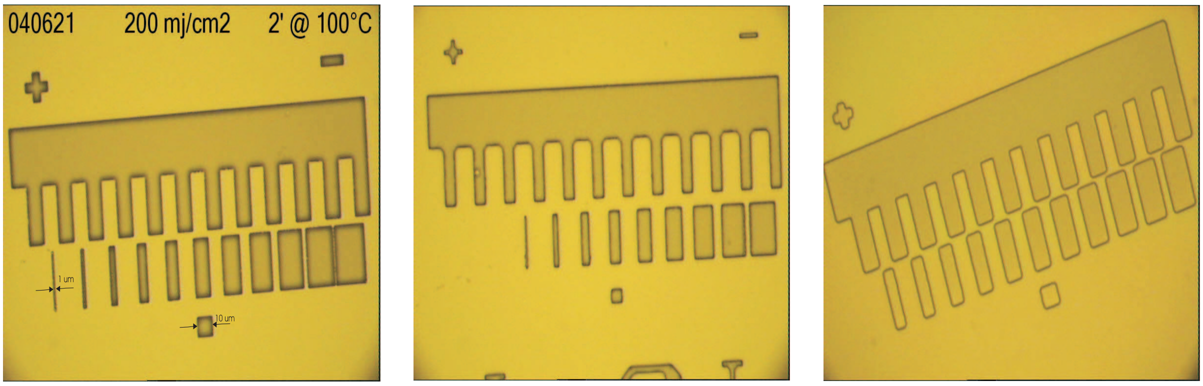

Figure 3.9: This comb structure allows us to determinate if the parameters used in the photolithography are optimal. The nominal width of the individual comb teeth is 10 μm.

understood. For a review, excellent general reference books are available[4]. In this section we describe briefly the principal features of the thin film processes we used to fabricate the samples and we shall remark some practical issues.

On the one hand, the materials used to fabricate the samples were:

a) Copper, as normal metal.

b) Niobium, as superconductor material.

c) Silicon nitride (Si_3N_4), as insulating or passivation layer.

And on the other hand, the three “building blocks” thin film processes we used to fabricate the samples were:

a) Deposition of metallic films (Cu and Nb) by DC sputtering.

b) Deposition of insulating films (Si_3N_4) by RF sputtering and Plasma Enhanced Chemical Vapor Deposition (PECVD).

c) Etching of Nb and Si_3N_4 by Reactive Ion Etching (RIE).

[4]John L. Vossen and Werner Kern, *Thin Film Processes*, Academic Press (1978). B. Chapman, *Glow Discharge Processes*, John Wiley and Sons (1981). D. L. Smith, *Thin Film Deposition*, McGraw Hill (1995)

3.3.1 DC magnetron sputtering

Figure 3.10(left) shows the fundamental elements used in a sputtering system. The material we wish to deposit is made into a sputtering target (cathode) which is held at a high negative DC voltage relative to the substrate and walls of the chamber (grounded anode). It is assumed that the target is a conducting material. The substrate which we wish to coat is placed a few centimeters away. After the chamber is evacuated, argon gas is introduced and an electric field perpendicular to the target is established to produce a glow discharge where electrons are accelerated and collide with argon atoms to generate positively-charged Ar ions, which are in turn accelerated toward the cathode. When these ions strike the cathode they dislodge atoms from the target which fly off in random directions, and some of them condense on the substrate leading to the building up of a thin film on the substrate. In order to confine electrons close to the target surface, thereby increasing ionization in this region, a magnet is placed under the target (magnetron).

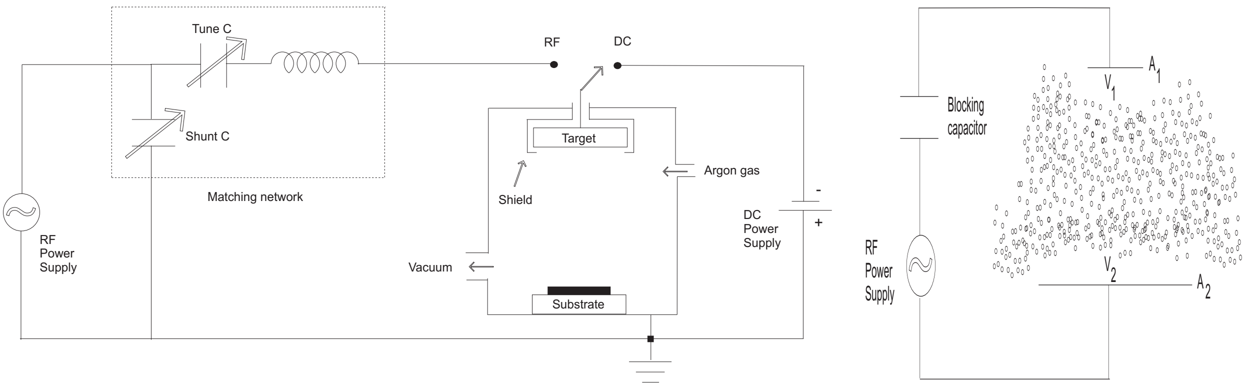

Figure 3.10: Left: schematic of a DC/RF sputtering system. Right: schematic of an asymmetrical RF system.

3.3.1.1 Experimental notes

a) The target is bond to the electrode by a silver-based thick film conductor paste. In order to assure a good thermal and electrical contact it is mandatory to test the flatness of both surfaces.

b) It is also necessary to check there is no water leaks in the circuit used for cooling the target. Their consequences are short circuits, instabilities in the power source, a lack of reproducibility, water vapor contamination, etc.

c) The target is surrounded by a ground shield, and separated from it by a distance of 1 to 1.5 mm. On the one hand, it is this separation that enables the ignition of the plasma because it is in the space between them that the electric field is more intense, and on the other hand, the shield restrict ion bombardment and sputtering to the target only. Otherwise, the target mounting clips and mechanical supports would also be sputtered and cause the film to be contaminated. This small separation between the target and the shield is a source of short circuits due to the occasionally peel off of deposits on the shield. This problem can be avoided by scraping periodically the shield.

d) In our chamber are mounted three magnetrons. We have observed that the relative orientation (North/South) of the magnets is important. They must be placed with the same orientation pointing to the sample, otherwise instabilities in the power source appear.

e) Owing to the relative high pressure used in sputtering systems (1 to 50 mTorr) deposition of material is observed even on the backside of the substrate holder.

3.3.1.2 Operating parameters

The operating parameters for the DC sputtering of both Cu and Nb were the same:

Ar pressure	Ar flow	DC power	Voltage	Current
10 mTorr	14.5 sccm	250 W	276 V	0.93 A

The diameter of the niobium target was 62 mm and the distance to the substrate was 3 cm, under the above conditions the rate of deposition was 2.6 nm/s. The diameter of the copper target was 50 mm and the distance to the substrate was 7 cm. Under the above conditions the rate of deposition was 1.6 nm/s. The substrate was water cooled but neither control nor measurement of its temperature was performed.

The chamber base pressure was 10^{-7} mbar. The standard operating procedure was: purge Ar line for 5 minutes; clean Cu target by DC sputtering for 2 minutes; clean Nb target by DC sputtering for 2 minutes; deposition of Cu by DC sputtering for 1 min (100 nm) and immediately deposition of Nb for 30 seconds (80 nm).

3.3.2 RF magnetron sputtering

If one wants to deposit an insulating material as silicon nitride it is not possible to use a DC power source as described in the above section. The reason is that once the glow discharge is initiated and the negatively biased target begin to be bombarded by positive ions, the insulator starts to charge positively until the discharge is extinguished. This problem is avoided by using an RF discharge[5], see Fig. 3.10(left), so that the positive charge accumulated during one half cycle can be neutralized by electron bombardment during the next half cycle.

In fact, if high enough frequencies are used almost continuous energetic ion bombardment can be achieved due to the self-bias or negative dc offset voltage acquired by the target surface[6]. This negative self-bias voltages is at the origin of the dark region (sheath) observed close to

[5]G. S. Anderson, Wm. N. Mayer and G. K. Wehner, *Sputtering of dielectrics by high frequency fields*, J. Appl. Phys. **33**, 2991 (1962).

[6]H. S. Butler and G. S. Kino, *Plasma sheath formation by radio frequency fields*, The Physics of Fluids **6**, 1346 (1963).

the electrodes, the electrons are repulsed away and the luminosity of the glow discharge in this region diminishes. This negative self-bias voltage, or sheath voltage, also is responsible for the energy acquired by the positive ions which impinges on the electrodes.

In a sputter deposition system we do not want wall materials to be sputtered in order to avoid a source of contamination. Hence, it will be necessary to keep the wall sheath voltage down to about 20 V, which is a typical threshold for sputtering. This is achieved by making the target area much smaller than the wall area, according to[7]

$$\frac{V_1}{V_2} = \left(\frac{A_2}{A_1}\right)^4 \tag{3.1}$$

where A_1 and A_2, V_1 and V_2 are the areas and sheath voltages of the respective electrodes, see Fig. 3.10(right).

In order to match the output impedance of the power source (50 Ω) to the input impedance of the plasma, a matching network consisting of a fixed inductance and two variable capacitors is mandatory, see Fig. 3.10(left). If the tuning is not correct, most of the forward power will be reflected and then the power dissipated in the load (plasma) will not be maximum.

3.3.2.1 Operating parameters

The operating parameters for the RF sputtering of Si_3N_4 were:

Ar pressure	Ar flow	RF power	DC self-bias
10 mTorr	14.5 sccm	200 W	-452 V

The diameter of the silicon nitride target was 50 mm and the distance to the substrate was 7 cm, under the above conditions the rate of deposition was 0.2 nm/s. The substrate was water cooled but neither control nor measurement of its temperature was performed.

The chamber base pressure was 10^{-7} mbar. The standard operating procedure was: clean target by RF sputtering for 5 minutes; deposition of Si_3N_4 by RF sputtering for 5 min (60 nm).

3.3.3 Reactive Ion Etching

Reactive Ion Etching (RIE) systems are essentially converted sputtering systems, see Fig. 3.11(left). In the former, sputtering is confined to the substrate while in the later sputtering is confined to the target. The same area-ratio effect applies in this case. In a RIE system etching relies not only on a physical sputtering but mainly on the chemical combination of the thin film surface atoms to be etched with an active gaseous species produced in the glow

[7]H. R. Kaufman and S. M. Rossnagel, *Analysis of area-ratio effect for radio frequency diode*, J. Vac. Sci. Technol. A **6(4)**, 2572 (1988).

discharge. It is mandatory that the products from theses chemical combinations be volatiles and pumped away by the vacuum system.

3.3.3.1 Operating parameters

The operating parameters for the etching of both Nb and “silicon nitride” were:

Etching gas	Pressure	Flow	RF power	DC self-bias
CF_4	7.5 mTorr	20 sccm	30 W	-415 V

The substrate temperature was not controlled or measured. By using the parameters above it were necessary 9 minutes to etch 80 nm of Nb and 15 minutes to etch 450+60 nm of “silicon nitride”.

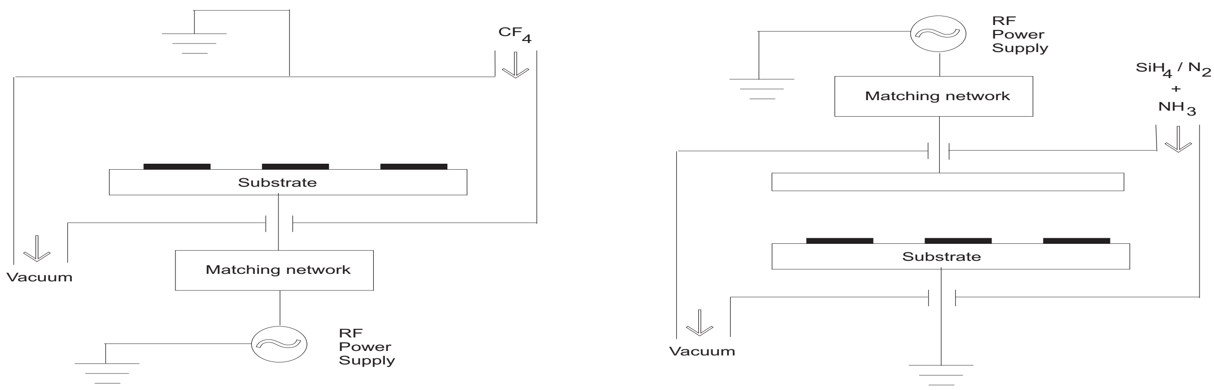

Figure 3.11: Left: schematic of a Reactive Ion Etching system. Right: schematic of a Plasma Enhanced Chemical Vapor Deposition system.

3.3.4 Plasma Enhanced Chemical Vapor Deposition

In a Chemical Vapor Deposition (CVD) system the constituents of the vapor phase react to form a solid film on whatever surface. In such systems typical temperatures ranging from 600^oC to 1300^oC are needed in order to dissociate the vapor phase molecules to produce very reactive radicals, atoms and ions. However, these dissociations can also be achieved by a glow discharge (plasma) as in a RIE system. The main advantage in utilizing such plasma enhanced deposition process is that the substrate temperature can be kept relatively low, typically 300^oC or lower.

Figure 3.11(right) shows a schematic of a Plasma Enhanced Chemical Vapor Deposition (PECVD) system, which presents the typical planar diode configuration with large electrodes of similar area. The fact that one of the electrodes is grounded does not mean it will receive low energy ion bombardment. On the contrary, according to Eq. 3.1, we will expect nearly equal sheath voltages at each electrode. As mentioned before, it is this voltage which determines the energy of ion bombardment. Hence, to avoid sputtering from the electrodes and wall a low power is recommended. This is also the reason for a beneficial preconditioning consisting of a previous deposition, all over the vacuum chamber, with the material we are interested in.

"Silicon nitride" produced by PECVD has not the stoichiometry Si_3N_4 since the ratio Si/N can be controllably varied depending on ratios of entrant reactant gas flows, power level, substrate temperature and chamber pressure[8]. In our case, the deposited thin film has the stoichiometry $Si_xN_yH_z$. Anyway, the only goal we seek is growing an insulating film, and so we are not interested in other physical properties as chemical composition, refractive index, or etch rates.

3.3.4.1 Operating parameters

The operating parameters for PECVD of "silicon nitride" were:

2%SiH_4/N_2 flow	NH_3 flow	Pressure	RF power	Substrate temperature
1000 sccm	30 sccm	1000 mTorr	25 W	300^{o}C

The substrate temperature was kept constant during deposition. By using the parameters above the final deposited thickness was 450 nm for 20 minutes deposition.

3.4 Fabrication process

The fabrication process was the same for all the samples, but we used different masks depending of the nature of the element embedded in the superconducting loop (a single Josephson junction or an array of Josephson junctions).

Before a more detailed description, we will outline the fundamental features of the fabrication process. Contact photolithography was used to define all structures. The fabrication sequence starts with the simultaneous definition of the Cu/Nb gradiometer loop, see Fig. 2.2, and the 3 μm wide Cu/Nb bridge, see Fig. 3.1, by a lift-off process, where the copper and niobium thin films were deposited by dc-magnetron sputtering in Ar onto a resist coated sapphire substrate without breaking the vacuum. After that, the junction itself (or the array) was defined by CF_4 RIE. In order to close the loop an insulating film of hydrogenated silicon nitride ($Si_xN_yH_z$) was first deposited by PECVD. The next step was to open two via holes through the insulating layer by CF_4 RIE. After that, a sputtered niobium short circuit was defined by liftoff, prior to an Ar sputter etching. Finally, a second layer of insulating film ($Si_xN_yH_z$) was deposited by PECVD followed by a niobium shield just on the junction.

[8]C. H. Ling, C. Y. Kwok and K. Prasad, *Silicon nitride films prepared by PECVD of $SiH_4/NH_3/N_2$ mixtures: some physical properties*, Jpn. J. Appl. Phys. **25**, 1490 (1986).

3.4.1 A path through twelve great steps

In this section we will describe with more detail the "birth" of a typical sample. As mentioned, our raw materials were copper, niobium and "silicon nitride", which were "fashioned" using photolithographic and thin films processes through the following twelve steps, see Fig. 3.12:

[Step 1] Pattern definition of the coplanar gradiometer and the 3 μm Josephson junction width bridge:

Photolithography process with an image reversal resist (if light then ↓) (see Annexe B) using sub-mask 3 for a junction, or sub-mask 3/12 for an array (see Fig. 3.2).

[Step 2] Deposition of a bilayer of Cu/Nb by DC sputtering and lift-off (see 3.3.1.2):

After deposition let the substrate vertically for several hours in AZ EBR solvent for lift-off. Clean the substrate but without using ultrasound baths (scrubbing may help). Heat for 2 minutes @ 110^{o}C and allow to cool.

[Step 3] Pattern definition of the 0.8 μm Josephson junction length:

Photolithography process with a positive resist (if light then ↑) (see Annexe B) using sub-mask 4 for a junction, or sub-mask 4/2 for an array (see Fig. 3.2).

[Step 4] Nb etching by CF_4 RIE to define the junction (see 3.3.3.1).

[Step 5] Deposition of an insulating film of "silicon nitride" by PECVD (see 3.3.4.1):

After deposition clean the substrate but without using ultrasound baths. Heat for 2 minutes @ 110^{o}C and allow to cool.

[Step 6] Pattern definition of two via (60 μm × 60 μm square shape):

Photolithography process with a positive resist (if light then ↑) (see Annexe B) using sub-mask 5 (see Fig. 3.2).

[Step 7] "Silicon nitride" etching by CF_4 RIE to define the via (see 3.3.3.1).

[Step 8] Pattern definition of a short circuit to close the coplanar gradiometer through the via:

Photolithography process with an image reversal resist (if light then ↓) (see Annexe B) using sub-mask 6 (see Fig. 3.2).

[Step 9] Deposition of Nb by DC sputtering and lift-off to define the short circuit (see 3.3.1.2):

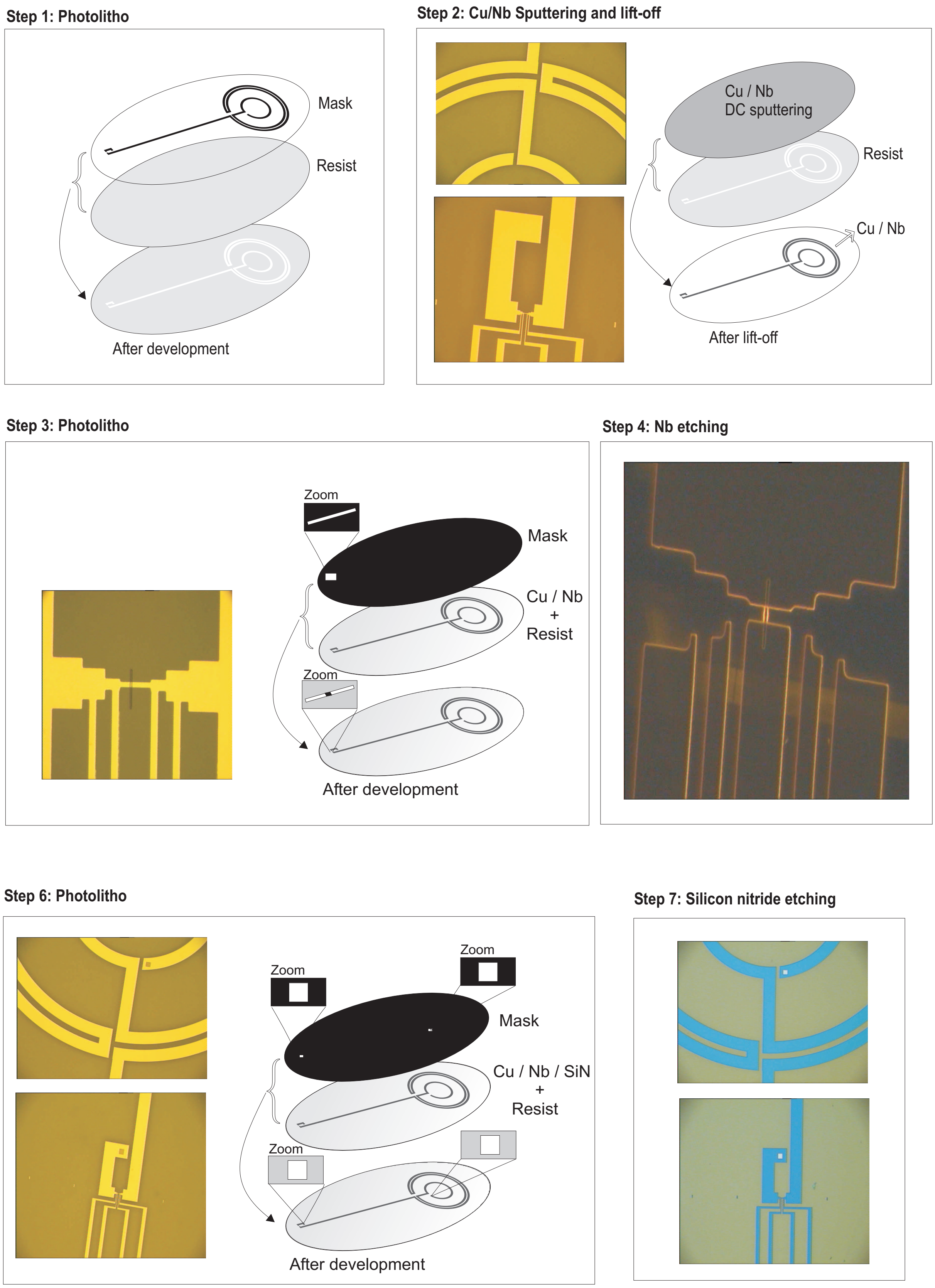
Step 1: Photolitho
Mask
Resist
After development
Step 2: Cu/Nb Sputtering and lift-off
Cu / Nb
DC sputtering
Resist
Cu / Nb
After lift-off
Step 3: Photolitho
Zoom
Mask
Cu / Nb
+
Resist
Zoom
After development
Step 4: Nb etching
Step 6: Photolitho
Zoom
Zoom
Mask
Cu / Nb / SiN
+
Resist
Zoom
After development
Step 7: Silicon nitride etching

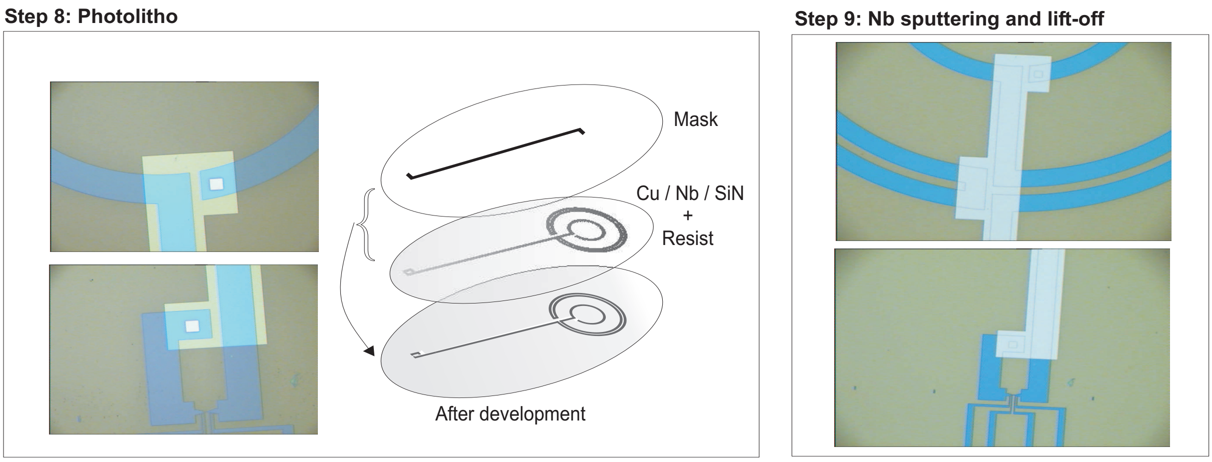

Figure 3.12: Schematic of the fabrication steps 1 to 9 with optical images of the sample after processes.

In this step process, and prior to the DC sputtering of Nb, a RF plasma sputtering is carried out on the substrate (30 W for 2 minutes) in order to etch the native oxide formed on the 60 μm $\times$ 60 μm Nb square surface through the two via. The operating procedure continues according to the following sequence: cleaning of the Nb target and deposition of Nb by DC sputtering for 2 minutes and 30 seconds (400 nm); let the substrate vertically for several hours in AZ EBR solvent for lift-off; clean it but without using ultrasound baths (scrubbing may help); heat it on a hotplate for 2 minutes @ 110^{o}C and allow it to cool at room temperature.

The purpose of the following three steps was to deposit a Nb shield just on the junction:

[**Step 10)**] **Deposition of an insulating film of "silicon nitride" by PECVD** (see 3.3.4.1):

A 450 nm thin film of "silicon nitride" was deposited following the standard procedure.

[**Step 11)**] **Deposition of Nb by DC sputtering to define the shield on the junction** (see 3.3.1.2):

In this case the mask was made simply by an aluminum sheet. A 400 nm thin film of Nb was deposited following the standard procedure.

[**Step 12)**] **Deposition of a passivation layer of Si_3N_4 by RF sputtering** (see 3.3.2.1):

A 60 nm thin film of Si_3N_4 was deposited following the standard procedure.

Figure 3.13 shows the final aspect of a typical sample and a SEM image of the junctiom. It is also shown a X-Ray analysis after the definition of the junction (step 4); the O and Al elements come from the sapphire substrate.

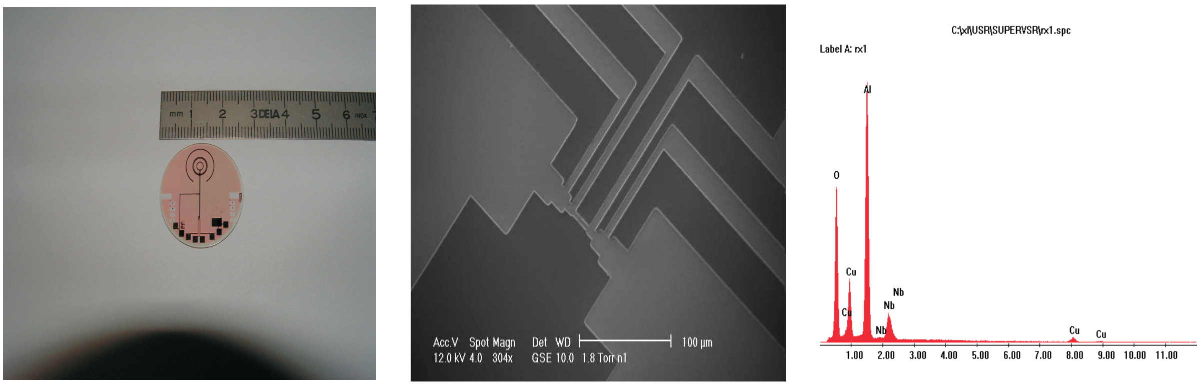

Figure 3.13: Left: sample (without Nb shield). Center: SEM image of the junction. Right: elements analysis after step 4.

3.5 Processes control

We notice that the aim of this part of the thesis has not been the optimization of the different processes but the fabrication of working samples. To this end, along the fabrication process we paid special attention to the following points:

a) We must control the thickness of the different deposited films.

b) We must make sure that the insulating film has no pinholes.

c) We must make sure that the niobium transition temperature is close to the bulk value (9.2 K).

d) We must control the etching process.

In this section we describe how the goals above were achieved.

3.5.1 Film thickness control

Films thickness were well reproduced in all the deposition processes from one run to another. This eliminated the need to check in situ the film growing once the operating parameters, during the different depositions, were fixed.

3.5.2 Control of the electrical insulation in silicon nitride films

We started to use silicon nitride deposited by RF sputtering as insulating layer but these films presented problems due to the presence of pinholes, apparently this is a common specific problem for RF sputtered insulating materials [9] although we do not understand its origin. For

[9] V. Y. Doo, D. R. Nichols and G. A. Silvey, *Method for depositing continuous pinhole free silicon nitride films and products produced thereby*, U.S Patent number 4089992 (1978).

this reason we decided to use a PECVD method to grow the "silicon nitride" insulating films and, in this case, all the produced films were free from pinholes.

The electrical insulation control was performed on a niobium coated proof substrate placed beside the sample during the "silicon nitride" PECVD coating. After that, a second niobium film was deposited over the proof substrate to be finally tested with an ohmmeter for short circuits.

3.5.3 Niobium critical temperature control

The critical temperature of the niobium films is a fundamental parameter to us because the behavior of the fabricated devices are mainly based on the superconducting state of such films.

The first task was then to deposit thin niobium films with a critical temperature close to the bulk value (9.2 K). In order to check the critical temperature we implemented a dip probe that can be immersed directly onto an ordinary storage liquid helium dewar (100 liters), and which allow us to perform very quick measurements from 4.2 K to 20 K in order to observe the transition temperature of the grown films. The dip probe is first introduced in a cylinder jack which is evacuated and filled with 10 mbar of helium gas to allow a weak thermal contact with the liquid helium of the dewar.

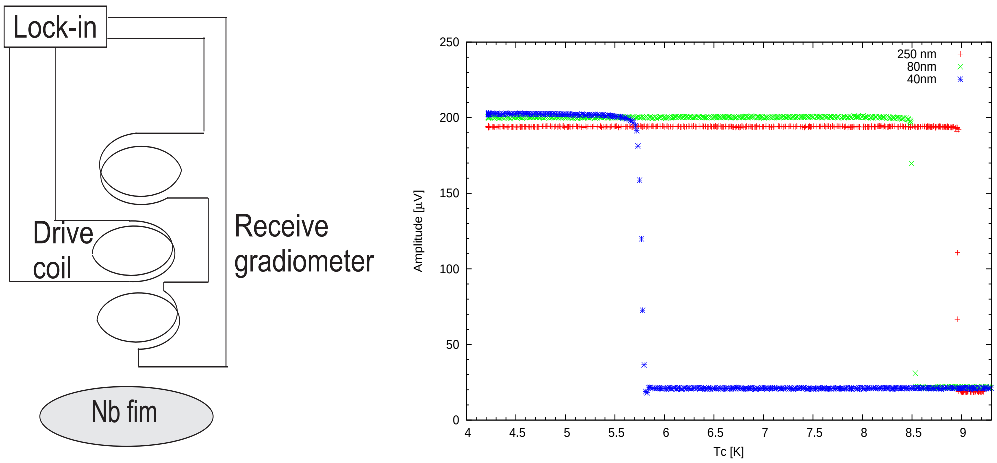

Figure 3.14: Left: schematic of the electrical configuration we used to measure the critical temperature of the Nb films. Right: temperature dependence of the magnitude of the signal measured with the set up shown in the left for three Nb films of different thickness (excitation frequency and amplitude: 250 KHz and 100 μA, respectively).

The electrical measurement setup was the same as described in Chap. 2 but without using the RF SQUID. The lock-in now reads the signal directly at the output of the gradiometric receive coil, see Fig. 3.14(left). Hence, at high temperatures, when the film is normal, the measured signal is low because of the gradiometric configuration of the receive coil. However, at low temperatures, when the film becomes superconductor, the bottom coil of the receive gradiometer will be shielded owing to Meissner effect and therefore the measured signal will be higher. Fig. 3.14(right) shows such measurements for niobium films of different thickness. The decrease of the critical temperature with decreasing thickness has been explained by some authors as due to the proximity effect induced by the formation of a niobium mono-oxide (NbO) layer that presents a critical temperature (1.5 K) much lower than the rest of the film [10]. But for the moment, our aim is not to study such dependence but to grow Nb films with critical temperature close to the bulk value.

The Nb thickness film we used for the fabrication of our Josepshon junctions was always 80 nm (Tc=8.6 K). We checked periodically that we were able to reproduce such superconducting films in order to make sure nothing has changed in the deposition system.

3.5.3.1 Experimental notes

The deposition of niobium films presented some problems. We resume here two tips for success:

a) **Avoid ferromagnetic "dust":** This was the principal problem. We had the chamber and load lock contaminated with tiny particles coming from metallic moving parts like the load-lock handle and screws, which are always manipulated to load the substrates. Unfortunately, these particles were ferromagnetic, the number one enemy of superconductivity!. The solution was to remove the ferromagnetic dust with a magnet and to avoid metallic screws and handles.

b) **Avoid oxigen:** We have also observed that the presence of oxygen is another detrimental factor for sputtering of niobium films. Niobium (as Titanium) is highly reactive with oxygen. Hence, throughout the sputter process the fresh Nb surface act as a getter, cleaning the sputter gas as the best pump of the system. Moreover, the formation of metallic NbO (superconductor at 1.5 K), would degradate the superconducting properties of the Nb film. For this reason, it is recommendable to put an oxygen filter in the argon line and well purging this line before each deposition.

Niobium has a natural oxide coating consisting of a layered structure, comprising amorphous Nb_2O_5, which is mechanically hard, stable and dense, as the outermost layer and reducing over a few nm to NbO_2 and NbO as the innermost layer. Above 100^{o}C this layer represents a source of oxygen which highly diffuses into the film. Furthermore, this oxidation triggers a complex crack corrosion that may reach depths between 0.01-1/1-10 μm, depending on Nb quality and oxidation strength, and degrading its critical temperature[11]. Thus Nb oxidation above 100^{o}C is not appropriate for the superconducting applications.

We faced the above problem when we tried to deposit silicon nitride on niobium by PECVD. As mentioned before, in a PECVD run the substrate is kept at 300^{o}C. Hence, if one place, at

[10] L. N. Cooper, *Superconductivity in the neighborhood of metallic contacts*, Phys. Rev. Lett. **6**, 689 (1961). A. I. Gubin, K. S. Il'in, S. A. Vitusevich, M. Siegel and N. Klein, *Dependence of magnetic penetration depth on the thickness of superconducting Nb thin films*, Phys. Rev. B **72**, 064503 (2005).

[11] J. Halbritter, *On the oxidation and on the superconductivity of niobium*, Appl. Phys. A **43**, 1 (1987).

atmospheric pressure, a substrate with Nb patterns on the hot baseplate the degradation of its critical temperature will be guaranteed. It is then necessary to heat up the baseplate only after a "good vacuum" has been reached. However, since the PECVD equipment we used is not designed to achieve high vacuum pressures (it has only a root pump) we decided to protect the niobium from oxidation with a 60 nm thickness film of Si_3N_4, deposited by sputtering, before running the PECVD process.

Fig. 3.15 shows a series of measurements where the above comments are putted in evidence. It is observed a clear degradation of the niobium critical temperature after oxidation at 300^{o}C. However, this degradation is avoided if the substrate is protected by a thin film (Si_3N_4) prior the oxidation. Notice also the influence of the initial thickness of the Nb film on its critical temperature after thermal oxidation. We have observed also that an oxygen plasma does not degrade the critical temperature of the Nb films, suggesting that the combination of oxygen with thermal processes above 100^o are at the origin of such degradation.

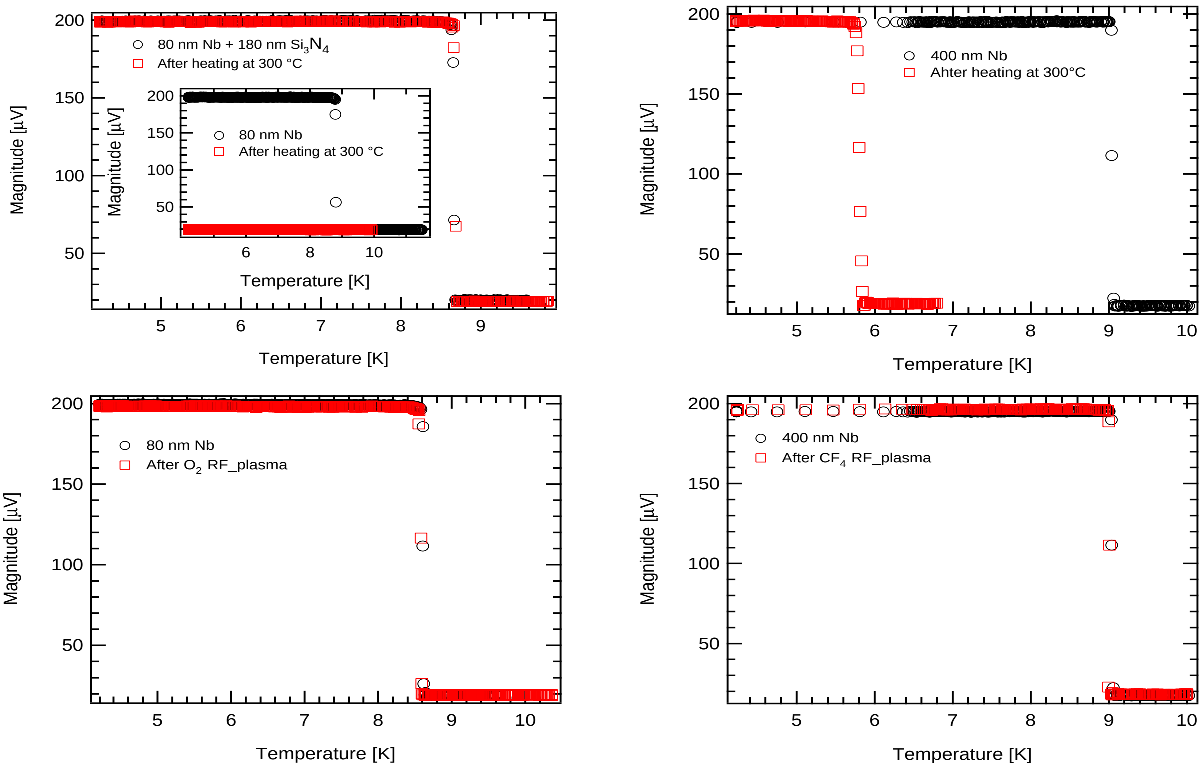

Figure 3.15: Top: Niobium critical temperature after thermal oxidation under different conditions. Bottom: Niobium critical temperature after O_2 and CF_4 plasma exposition.

3.5.4 Optical control of niobium and silicon nitride etching

Along the fabrication process it was needed to etch some material in two occasions: first, to define the Josephson junction in order to remove the niobium deposited on copper, and second, to make two via through the insulating film in order to remove the "silicon nitride" deposited on niobium . In both cases, it is important not to etch the underneath material, that is, the copper in the first case, and the niobium in the second one.

In order to control the etch-stop point an interferometer arrangement consisting of a laser light, a beam splitter and a photodiode detector was used. The spot laser impinged on a proof substrate placed beside the sample to be etched by RIE. In the first case, a step was observed at the output of the detector when the interface Cu/Nb was reached[12]. In the second case, due to the relative transparency of the "silicon nitride" film a series of maximums and minimums were observed during the etching; the absence of these features indicated that the niobium has been reached. Fig: 3.16 shows the measured signals at the output of the photodiode during the etching process in both cases.

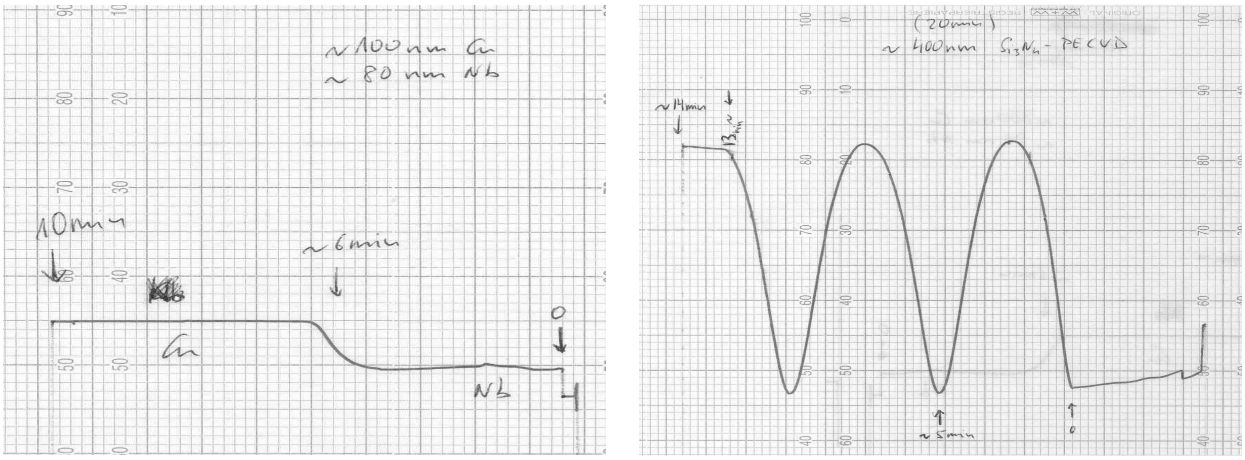

Figure 3.16: Photodiode output signal during etching of niobium (left) and "silicon nitride" (right).

3.6 Conclusions

In this chapter, the processes needed to fabricate the proposed devices are described. The design of the different masks allows for the fabrication of different configurations - a single, a series or an array - of Josephson junctions embedded in a coplanar and garadiometric coil using the same fabrication process.

The fabrication sequence starts with the definition of the gradiometric coil and the width of the Josephson junction (or surface of the array) by depositing two thin films of copper and niobium. After that, the length of the junction(s) is defined by etching the niobium film through an appropriate mask. In order to close the coil an insulating film of hydrogenated silicon nitride is deposited on the sample and two via holes are opened through it followed by connecting them with a niobium stripeline. Finally, two thin films of hydrogenated silicon nitride and niobium are deposited on the junction (or the array) in order to shield it from external magnetic fields.

[12]Notice that, additionally, the copper layer acts as a natural etch-stop layer because copper can not be etched with CF_4.

Chapter 4

Dynamics of a single Josephson Junction: experiments and theory

The fabricated device consists of a Josephson junction embedded in a a superconducting ring, base of an AC SQUID (Alternating Current Superconductor Quantum Interference Device). As already described, the coupling between the device and the measurement system is made inductively. In order to study its dynamics both AC and DC measurements have been carried out. In Section 4.2 a model is presented in order to qualitatively understand the experimental data. An extension of this model which quantitatively predicts the response of the system is presented in Section 4.3.

The study of the dynamics of a superconducting loop interrupted by a Josephson junction started with the work of Silver and Zimmerman[1] where multiple quantum jumps and an hysteretic behavior of the total flux threading the loop versus the applied flux were already observed. Somme numerical calculations on this system were performed by Ben-Jacob *et al.*[2]. On the other hand, Kurkijarvi studied the effect of thermal fluctuations [3]. A simple experiment to observe the entry of quantum of flux was performed by Smith *et al.*[4]. Despite the fact that the system we are dealing with is old, the way our measurement system interacts with the sample is original. It is the first time such a measurements are carried out.

[1]A. H. Silver and J. E. Zimmerman, *Quantum transitions and loss in multiply connected superconductors*, Phys. Rev. Lett. **15**, 888 (1965). A. H. Silver and J. E. Zimmerman, *Quantum states and transitions in weakly connected superconducting rings*, Phys. Rev. **157**, 317 (1966).

[2]E. Ben-Jacob and Y. Imry. *Response times of short Josephson junction and applications to rf SQUID's* , J. Appl. Phys.. **51(8)**, 4317 (1980).

[3]J. Kurkijarvi, *Intrinsic fluctuations in a superconducting ring closed with a Josephson junction*, Phys. Rev B **6**, 832 (1972).

[4]H. J. T. Smith and J. A. Blackburn, *Multiple quantum flux penetration in superconducting loops*, Phys. Rev. B **12**, 940 (1975).

4.1 Introduction

Figure 4.1 shows a typical AC measurement. The sample is excited through the drive coil by an alternating magnetic field at fixed amplitude[5] and frequency. Under these conditions a controlled temperature sweep is performed. As expected with the two coils measurement technique, at sufficiently low temperatures, the inductive component reaches a constant value and the dissipative component vanishes, recovering a conventional superconducting response, *i.e.*, a purely inductive response with a phase difference of ninety degrees between the excitation and detected currents.

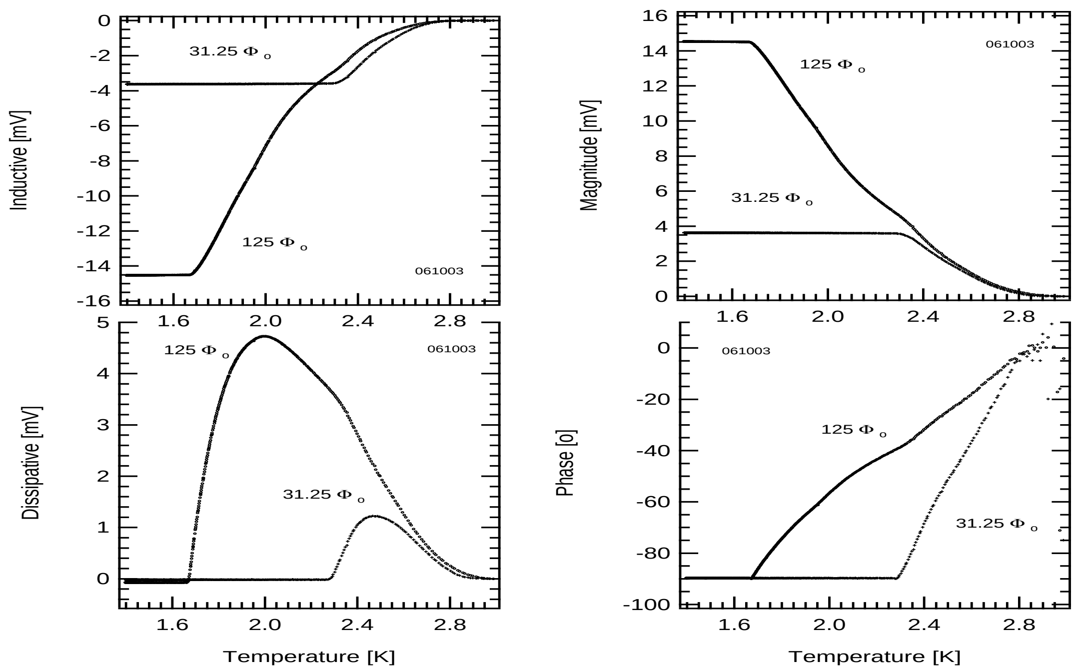

Figure 4.1: AC measurements at 555 Hz: temperature dependence of the inductive and dissipative (left) / magnitude and phase (right) components for two values ($31.25\Phi_o$ and $125\Phi_o$) of the amplitude of the AC applied flux.

By looking at the experimental data shown in Fig. 4.1 two fundamental questions arise:

i) Why does the dissipation start to grow with decreasing the temperature and vanish suddenly?

ii) Why does the dissipation vanish at a lower temperature with increasing the amplitude of the drive magnetic flux?

[5] $\Phi_o = 2.07 \times 10^{-15}$Wb is the superconductor quantum flux. A quantum of flux applied on the loop of the sample (1 mm radius) corresponds to a magnetic field of $\sim 1\ nT$.

4.2 The inductively shunted junction (ISJ) model

In order to answer the questions above we start with the simplest model, which is shown in Fig. 4.2

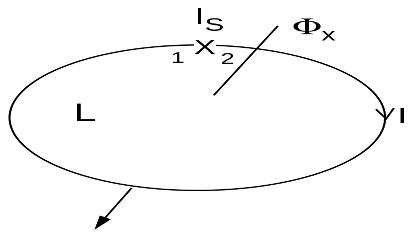

Figure 4.2: A Josephson junction in a superconducting ring of self inductance L in an applied flux Φ_x.

Fundamental equations:

a) Fluxoid quatization

$\Delta\gamma + 2\pi\frac{\Phi}{\Phi_o} = 2\pi n$

b) Josephson current

$I_s = I_c(T)\sin(\Delta\gamma)$

c) Total flux

$\Phi = \Phi_x + LI$

The nonlinearity due to the presence of the weak link and fluxoid quantization are the two fundamental features of this device[6].

The essential feature of superconductivity is the condensation of a macroscopic number of particles (bound-electrons (Cooper) pairs) in the same single quantum state. According to the phenomenological theory of Ginzburg and Landau, such a macroscopic state can be described by a wave function Ψ_s. This complex wave function has an amplitude $\Psi_o(\vec{r}, t, T)$ and a phase $\theta(\vec{r}, t)$

$$\Psi_s = \Psi_o(\vec{r}, t, T)\ \ e^{i\theta(\vec{r},t)} \tag{4.1}$$

In the Ginzburg-Landau theory $\mid \Psi_s \mid^2$ is interpreted as an order parameter which represents the Cooper pairs density at a given temperature T, $\rho_s = \mid \Psi_s \mid^2$, and hence

$$\Psi_s = \sqrt{\rho_s(\vec{r}, t, T)}\ \ e^{i\theta(\vec{r},t)}, \tag{4.2}$$

in which $\rho_s \to 0$ if $T \to T_c$. The absolute phase is not observable, but we will show that phase differences are directly observable quantities. In the Guinzburg-Landau theory, the current

[6]F.London, *Superfluids (Vol. I)*, Dover (1961). K. K. Likharev, *Dynamics of Josephson junctions and circuits*, Gordon and Breach (1986). M. Thinkham, *Introduction to superconductivity*, McGraw-Hill (1996). A. Barone and G. Paterno, *Physics and applications of the Josephson effect*, Wiley (1982). P. G. de Gennes, *Superconductivity in metals and alloys*, W. A. Benjamin (1968). L.-P. Lévy, *Magnetism and superconductivity*, Springer-Verlag (1997). R. de Bruyn Ouboter, *Macroscopic quantum phenomena in superconductors*, Superconductor Applications: SQUIDS and Machines, Edited by B.B. Schwartz and S. Foner, NATO Advanced Study Institutes Series, Vol. 1, Plenum Press (1976).

density I_s is related to the probability current density of quantum mechanics in terms of the wave function Ψ_s

$$I_s = -\frac{i\hbar}{2m^*}\left(\Psi_s^*\vec{\nabla}\Psi_s - \Psi_s\vec{\nabla}\Psi_s^*\right) - \frac{q^*}{m^*} \mid \Psi_s \mid^2 \vec{A} \tag{4.3}$$

where $q^* = 2e$ and $m^* = 2m$. The above equation can be rewritten, using 4.1, as

$$I_s = \mid \Psi_s \mid^2 \frac{\hbar}{2m}\left[\vec{\nabla}\theta - \frac{2e}{\hbar}\vec{A}\right] = \mid \Psi_s \mid^2 \ \vec{v_s} = \rho_s \, \vec{v_s}. \tag{4.4}$$

From the above equation one obtains the fundamental relation for the generalized momentum $\vec{P_s}$

$$\vec{P_s} \equiv 2m\vec{v_s} + 2e\vec{A} = \hbar\vec{\nabla}\theta. \tag{4.5}$$

We should like to remark that Eqs. 4.4 and 4.5 are gauge invariant under the following transformations for the vector potential $\vec{A}$, the scalar potencial φ, the phase θ and the generalized momentum $\vec{P_s}$

$$\vec{A}' = \vec{A} + \vec{\nabla}\chi; \quad \varphi' = \varphi - \frac{\partial\chi}{\partial t}; \quad \theta' = \theta + \frac{2e}{\hbar}\chi; \quad \vec{P_s}' = \vec{P_s} + 2e\vec{\nabla}\chi, \tag{4.6}$$

and we introduce the gauge invariant phase γ defined by

$$\vec{\nabla}\gamma = \vec{\nabla}\theta - \frac{2e}{\hbar}\vec{A}. \tag{4.7}$$

Let us now consider a closed trajectory in a superconducting material. No matter how the phase θ changes as one goes around the trajectory the phase must return to the same value (mod 2π) when one returns to the starting point in order to the wave function Ψ_s stay single valued. Hence

$$\oint d\theta = 2\pi n. \tag{4.8}$$

Let us apply the above relation to the closed loop shown in Fig. 4.2

$$\oint d\theta = \Delta\theta_{J(1->2)} + \Delta\theta_{L(2->1)} = 2\pi n, \tag{4.9}$$

where $\Delta\theta_{J(1->2)} = \theta_2 - \theta_1$ is the phase change across the junction, while $\Delta\theta_{L(2->1)}$ is the phase change measured around the superconducting loop with self inductance L. We can write, in a general form, $d\theta = \vec{\nabla}\theta d\vec{s}$. Hence, Eq. 4.5 can be written as

$$\frac{2m}{\hbar}\int \vec{v_s}d\vec{s} + \frac{2e}{\hbar}\int \vec{A}d\vec{s} = \int \vec{\nabla}\theta \; d\vec{s} = \Delta\theta. \tag{4.10}$$

If we choose the integration trajectory inside the superconducting loop, where there is no supercurrent flowing due to the Meissner effect ($\vec{v_s} = 0$) one has, using Eq. 4.10

$$\Delta\theta_{L(2->1)} = \frac{2e}{\hbar}\int_2^1 \vec{A}d\vec{s} \tag{4.11}$$

On the oder hand, if we use Eq. 4.7 in order to introduce the gauge invariant phase difference across the junction, one has

$$\Delta\theta_{J(1->2)} = \Delta\gamma + \frac{2e}{\hbar}\int_1^2 \vec{A}d\vec{s}. \tag{4.12}$$

Finally, substituting Eqs. 4.12 and 4.11 in 4.9 one obtains

$$\Delta\gamma + 2\pi\frac{\Phi}{\Phi_o} = 2\pi n, \tag{4.13}$$

where $\Phi = \oint \vec{A}d\vec{s}$ is the total flux threading the superconducting ring and $\Phi_o = h/2e$ is the quantum of flux. The left hand side of the above equation is the fluxoide, which is then quantized.

The Josephson relation for the superconducting current I_s through the junction is

$$I_s = I_c(T)\sin(\Delta\gamma), \tag{4.14}$$

where $I_c(T)$ is the critical current, *i.e.*, the maximum steady current that can flow through the junction without dissipation[7]. By using Eq. 4.13 one has

$$I_s = I_c(T)\sin(-2\pi\frac{\Phi}{\Phi_o}), \tag{4.15}$$

On the other hand, the total flux Φ is related to an external magnetic flux Φ_x by

$$\Phi = \Phi_x + LI, \tag{4.16}$$

where L is the self inductance of the coil which closes the circuit where the Josephson junction is incorporated and I is the total current flowing through it.

It is then natural to impose the condition

$$I = I_s \tag{4.17}$$

that is

$$\frac{1}{L}\mathbf{\Phi} - \frac{\Phi_x}{L} = I_c(T)\sin(-2\pi\,\frac{\mathbf{\Phi}}{\Phi_o}), \tag{4.18}$$

[7]Note that for a SNS (Superconductor-Normal-Superconductor) junction $I_c(T)$ increases monotically with decreasing the temperature.

which can be seen like an equation for the variable Φ bringing to light we are dealing with a nonlinear dynamic system.

Figure 4.3 illustrates the general behavior of the system described by Eq. 4.18[8]. The response of the system (total flux Φ or total current I) to an external applied flux Φ_x is the solution of equation 4.18. In other words, it is the intersection of the line $I = I(\Phi) = (1/L)\Phi - (\Phi_x/L)$ with the sinusoidal curve $I = I(\Phi) = I_c(T)sin(-2\pi(\Phi/\Phi_o))$. The external applied flux Φ_x controls the ordinate at the origin of the line, whose slope $1/L$ is fixed by the geometry (self inductance L) of the loop of the sample. On the other hand, the temperature controls the amplitude of the sinusoidal curve via the critical current of the junction.

This graphical representation (Fig. 4.3) of Eq. 4.18 is the key to understand qualitatively the principal features of our measurements.

4.2.1 DC measurements: jumps and hysteresis cycles

DC measurements were performed in order to check this model. In these measurements, at a fixed temperature, the applied magnetic flux on the sample is increased from zero to some maximum and then decreased to zero. The voltage from the SQUID output (ΔV_{sq}) is measured directly, without using the lock-in; and the current flowing in the sample (ΔI_{sa}) is obtained from $\Delta I_{sa}[\mu A] = 0.83\Delta V_{sq}[mV]$, see Sec. 2.4. In Fig. 4.4 the current flowing through the device as a function of the external applied flux is shown for different temperatures. The data exhibit the expected jumps and hysteresis cycles, which are consistent with the model represented in Fig. 4.3.

Point "1" in Fig. 4.4 corresponds to an state where a current flows in the device with no external applied flux. This state corresponds to point 1 in Fig.4.3. Note that for an applied flux the system chooses one of the possibles states. In order to interpret the measurements shown in Fig. 4.4 the origin for the total flux in Fig. 4.3 is shifted to the right.

Following the path from 1 to 2 in Fig. 4.3 one observes that by increasing the external magnetic field the current decreases until it vanishes. If one further increases the external field the system reaches point 2 and starting from that point the current undergoes a series of jumps. But now, if one decreases the external magnetic field the system sweeps from a point 4 to point 5, and then, after a series of jumps, comes back to point 1 completing an hysteresis cycle.

[8]F. Bloch, *Simple interpretation of the Josephson effect*, Phys. Rev. Lett. **21**, 1241 (1968). F. Bloch, *Josephson effect in a superconducting ring*, Phys. Rev. B **2**, 109 (1970).

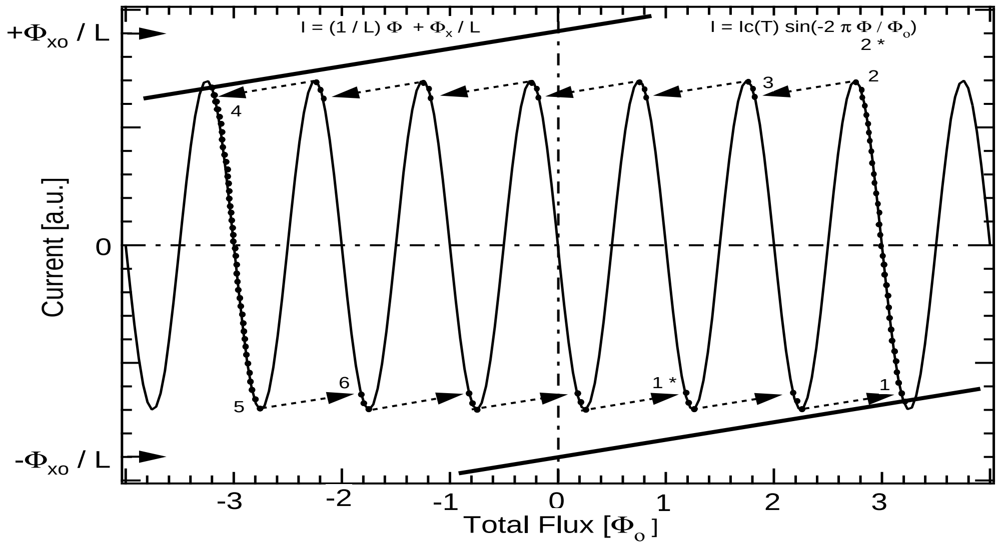

Figure 4.3: Graphical solution of equation 4.18. Particular solutions are represented by large dots. The amplitude of the sinusoidal curve is controlled via the temperature by the the critical current $I_c(T)$. The slope $1/L$ of the line is fixed by the geometry (self inductance L) and its position by the applied flux Φ_x, whose continuous sweep between $+\Phi_{xo}$ and $-\Phi_{xo}$ results in a series of jumps and hysteresis cycles.

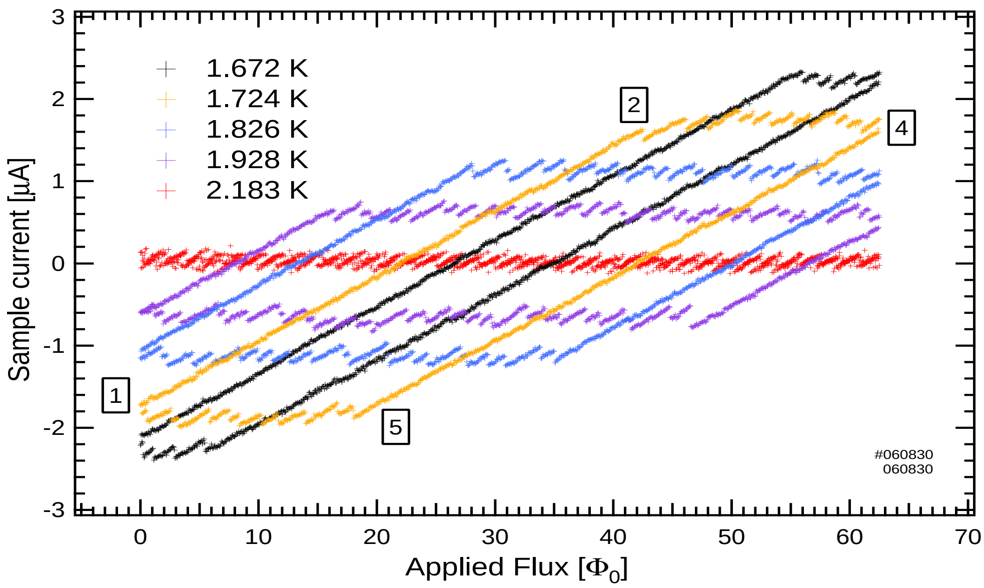

Figure 4.4: DC measurements at different fixed temperatures. Current flowing through the device as a function of the external applied flux in units of the quantum of flux. At each temperature, the applied flux is increased to $\sim 60\Phi_o$ and decreased to zero. The points (1,2,4,5) correspond qualitatively to the respective ones in Fig.4.3.

Depending on the particular initial state, it may be not necessary to change the polarity of the applied field in order to complete an hysteresis loop; but, if the initial state is $\Phi(\Phi_x = 0) = 0$ it is necessary to invert the polarity in order to complete the hysteresis cycle.

As can be deduced from Fig. 4.3, if the critical current increases (temperature decreases), the numbers of jumps will be smaller and the applied flux necessary to reach the critical current where the jumps start will be higher. The same behavior is observed in Fig.4.4. Finally, at a sufficient low temperature there will be neither jumps nor hysteresis cycle, for the given amplitude of the applied flux.

4.2.2 AC measurements: source of the dissipation

Figures 4.5 and 4.6 show AC measurements performed on two different samples. Each measurement was performed at a fixed frequency ν and amplitude Φ_{xo} of the alternating external applied flux ($\Phi_x = \Phi_{xo} sin(2\pi\nu t)$) while the temperature was increased.

In order to interpret qualitatively the measured data a correspondence between DC and AC measurements can be established. When we perform an AC measurement, by changing the temperature, we are actually sweeping through a continuous series of hysteresis cycles. At high temperature, the critical current is small, there are jumps[9], but the area of the hysteresis loop is small. When decreasing the temperature the loop area grows until some maximum and decreases until it finally vanishes at a sufficiently low temperature, which is the temperature at which dissipation also vanishes. Jumps and hysteresis cycles both are source of dissipation [10]. This explains qualitatively the bump observed in the dissipative component of the experimental data.

Once again, by using the model represented in Fig.4.3, the greater the amplitude Φ_{xo} of the sweeping flux, the higher the critical current at which the dissipation disappears, or in other words, a lower temperature is necessary for the jumps to disappear, as is observed in the AC measurements of Fig. 4.1.

[9] The larger slope of the straight line compared to the slope of the tangent to the sinusoidal curve at $\Phi = \Phi_o/2$ ($LI_c(T) > \Phi_o/2\pi$) is at the origin of the jumps.

[10] We will see that changes in the current (or in the total flux) are source of dissipation via the associated voltage $V = -\dot{\Phi}$ and the normal resistance of the junction.

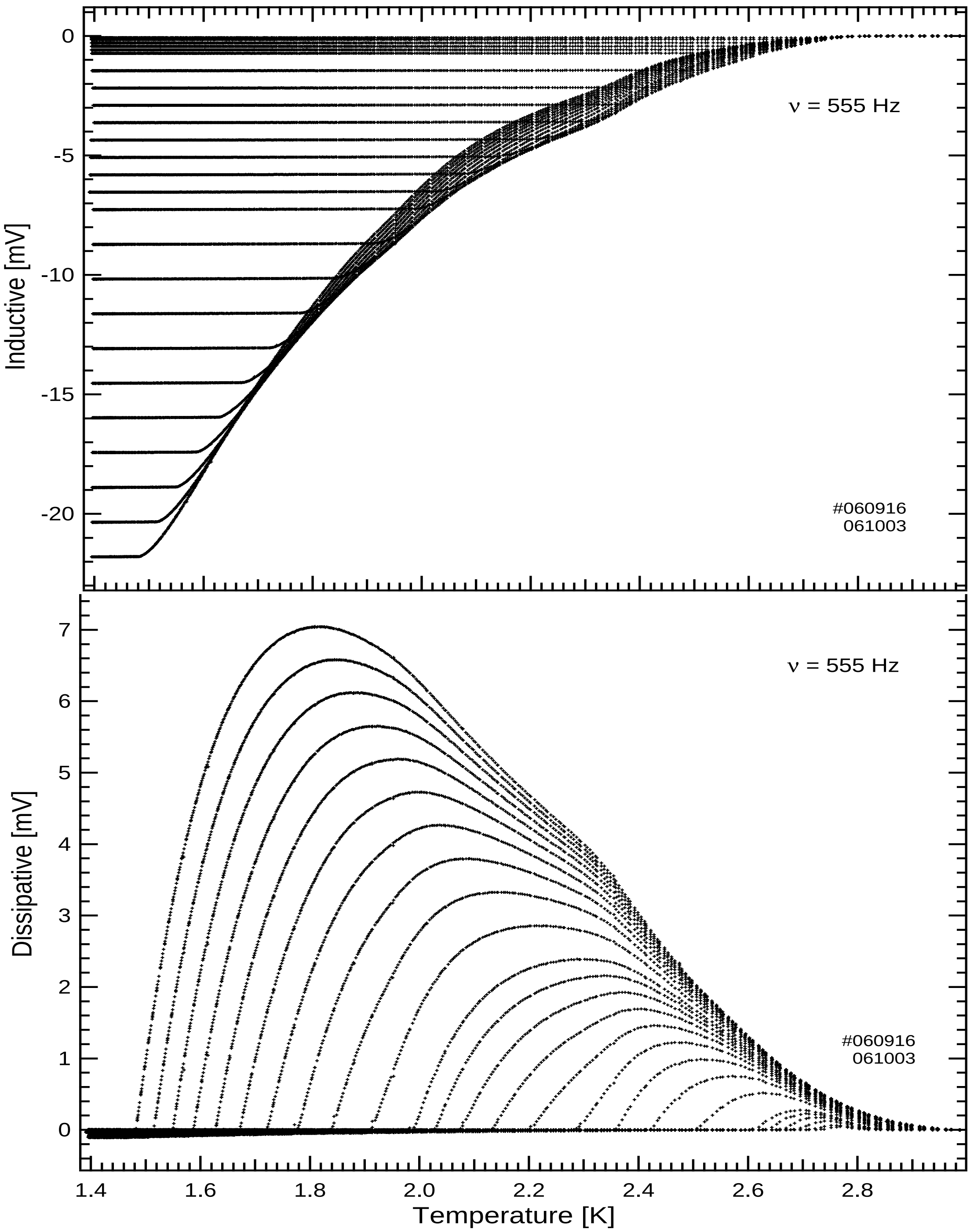

Figure 4.5: AC measurements. Applied flux amplitudes, from the bottom up for the inductive component and from top to bottom for the dissipative component in units of[$\sqrt{2}$ 62.5Φ_o]:(1)3.0 (2)2.8 (3)2.6 (4)2.4 (5)2.2 (6)2.0 (7)1.8 (8)1.6 (9)1.4 (10)1.2 (11)1.0 (12)0.9 (13)0.8 (14)0.7 (15)0.6 (16)0.5 (17)0.4 (18)0.3 (19)0.2 (20)0.1 (21)0.08 (22)0.06 (23)0.04 (24)0.02 (25)0.01. These data correspond to the sample #060916 (100 nm Cu/80 nm Nb).

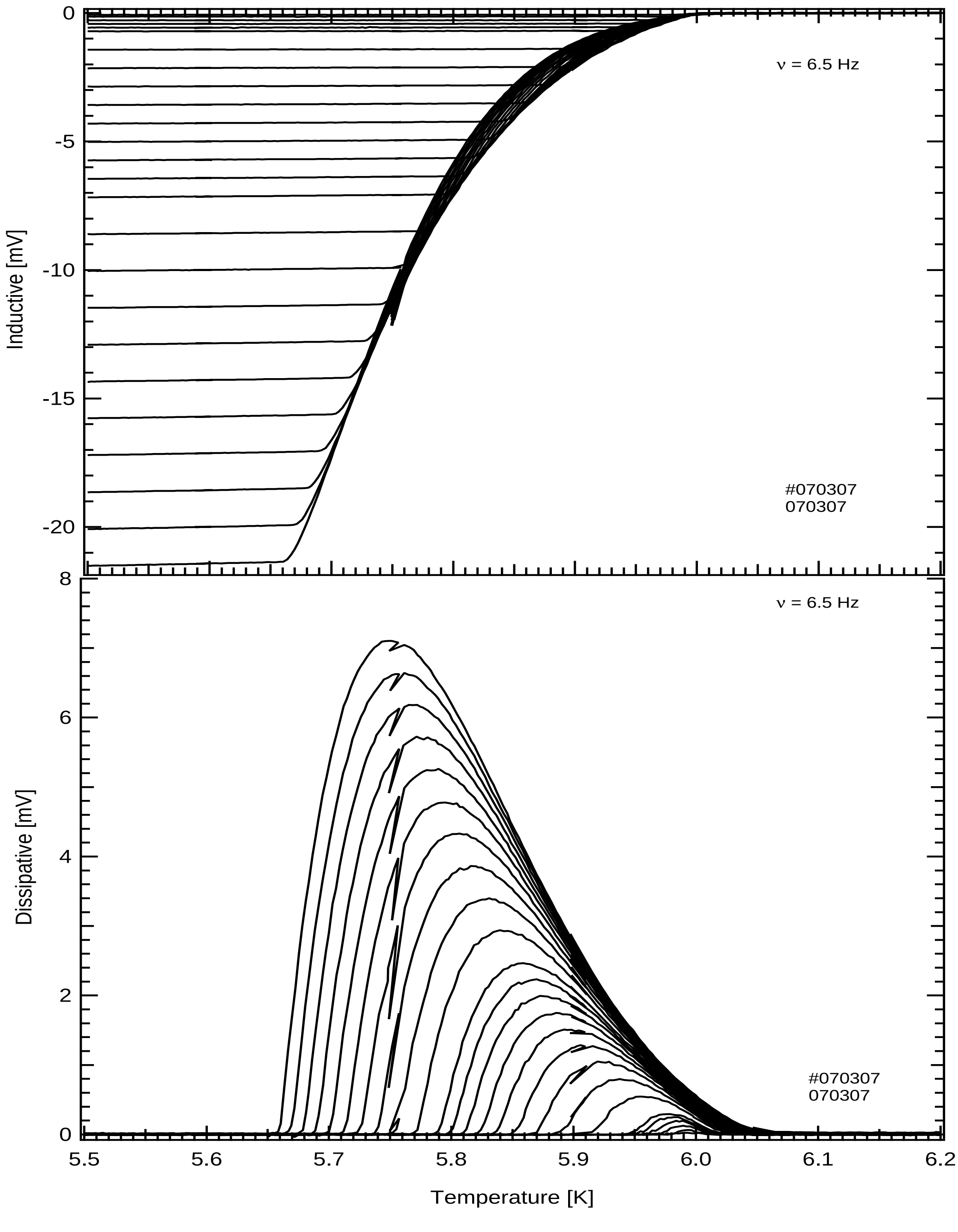

Figure 4.6: AC measurements. Applied flux amplitudes, from the bottom up for the inductive component and from top to bottom for the dissipative component in units of[$\sqrt{2}\ 62.5\Phi_o$]:(1)3.0 (2)2.8 (3)2.6 (4)2.4 (5)2.2 (6)2.0 (7)1.8 (8)1.6 (9)1.4 (10)1.2 (11)1.0 (12)0.9 (13)0.8 (14)0.7 (15)0.6 (16)0.5 (17)0.4 (18)0.3 (19)0.2 (20)0.1 (21)0.08 (22)0.06 (23)0.04 (24)0.02 (25)0.01. These data correspond to the sample #070307 (300 nm Cu/80 nm Nb).

4.2.3 Extracting the critical current from the AC measurements

We can use the model described above to extract the temperature dependence of the critical current from the series of AC measurements shown in Figs. 4.5 and 4.6. As mentioned, there is a temperature at which the dissipation vanishes and the response is purely inductive. At this moment, the amplitude of the signal, which reduces to the inductive component because the dissipative component is zero, corresponds to the amplitude of the critical current. Its value is obtained from the measured data by using the relationship 2.13 between the current flowing through the sample and the voltage reading at the output of the RF-SQUID $\mid \Delta I_{sa}[\mu A] \mid = 0.83 \mid \Delta V_{sq}[mV] \mid$. In this way a couple of values for each curve is obtained which represent the critical current at the corresponding temperature. Figures 4.7(left) and 4.7(right) show a representation of such values.

As expected, an exponential temperature dependence for the critical current is obtained, which is the signature of a SNS (Superconductor-Normal-Superconductor) weak link.

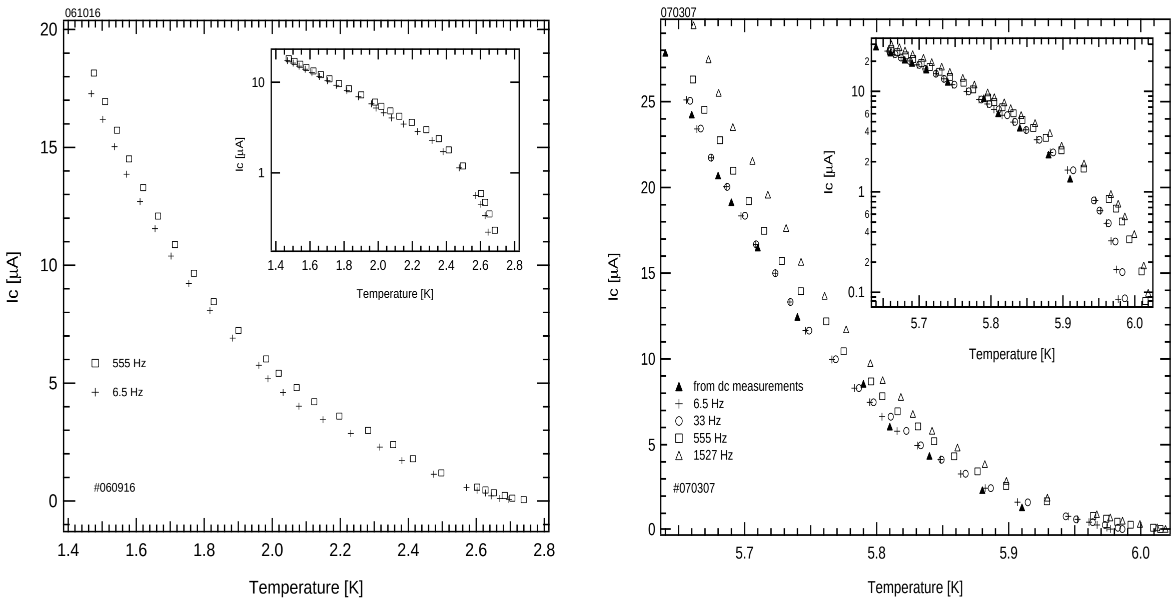

Figure 4.7: *Left*: Critical current corresponding to the sample #060916 (100 nm Cu/80 nm Nb) as a function of the temperature. Each measured point at 555 Hz has been obtained from the different curves of Fig.4.5. For comparison, the result from a similar series at 6.5 Hz is also presented. *Right*: Critical current corresponding to the sample #070307 (300 nm Cu/80 nm Nb) as a function of temperature. Each measured point at 6.5 Hz has been obtained from the different curves of Fig.4.6. For comparison, the results from a similar series at 33, 555, and 1527 Hz are presented, and also the critical current obtained from dc measurements (see Sec. 4.2.4).

4.2.4 Extracting the critical current from the DC measurements

At a sufficient high temperature the supercurrent is zero and so there is no contribution from the sample to the measured signal; the only contribution comes from the asymmetry in the receive gradiometer. This signal is called the pick-up and has to be subtracted from all the data in order to have the response of the sample as if the receive gradiometer was perfectly symmetric. Fig. 4.8 shows the measured data before and after subtracting the pick-up (straight line at high temperature). Figure 4.9 shows DC measurements where the pick-up has been removed. After that, the critical current, at each temperature, can be read out directly from the DC measurements as half the vertical distance between the two plateau of the respective hysteresis cycle. In this way, the critical current of the sample #070307(300 nm Cu/80 nm Nb) was deduced. The result is shown in Fig. ??, where a very good agreement with the critical current extracted from low frequency AC measurements was found.

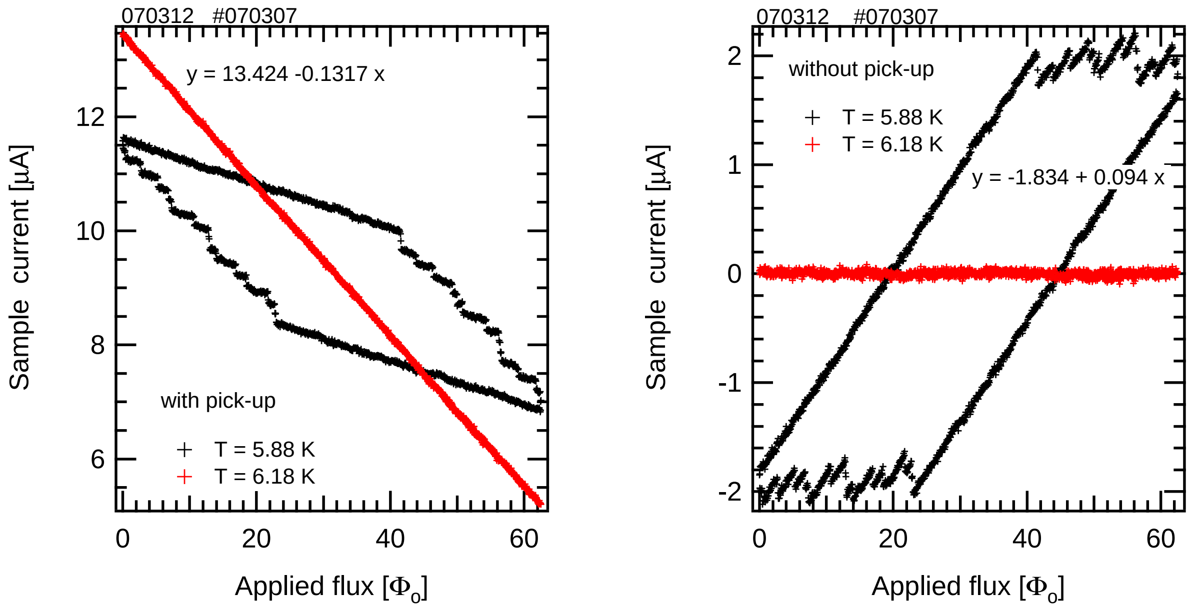

Figure 4.8: Left: DC measurements (with pick-up) performed on sample #070307. Right: The same data after subtracting the pick-up.

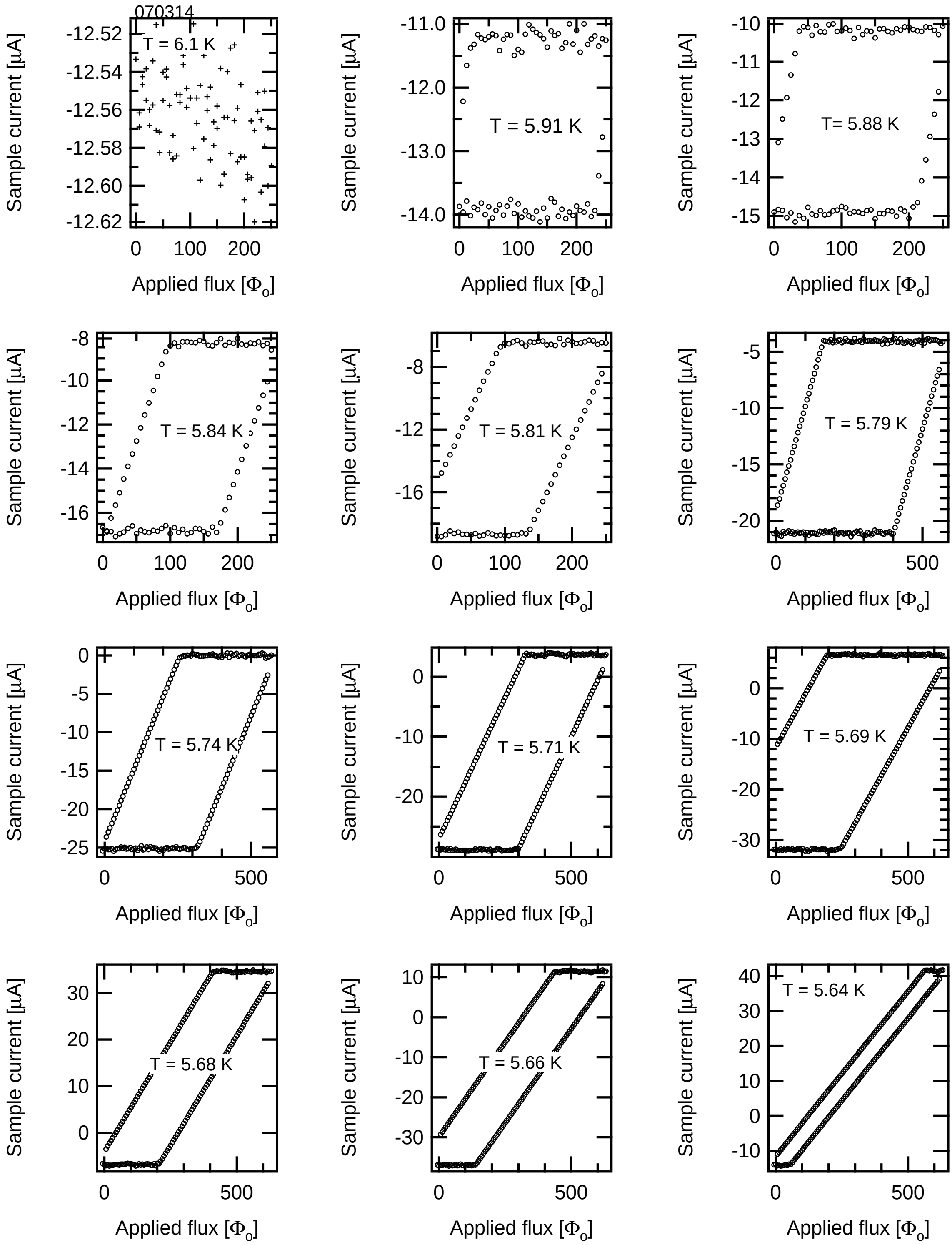

Figure 4.9: DC measurements (without pick-up) at different temperatures performed on sample #070307 (300 nm Cu/80 nm Nb).

4.2.5 Theoretical critical current

Trying to fit the experimental critical current to a theoretical curve is not an easy task, mainly because it is necessary to make sure the restrictions used by the different theoretical approaches are fulfilled. Mesoscopic Josephson junctions can be classified in ballistic (or "clean") / diffusive (or "dirty") and long / short weak links. In a "dirty" system the detailed atomic structure at the normal-superconductor interface is not very important and the large-scale motions of the superconducting electrons can be described by a diffusion equation. In this limit the supercurrent is carried by a continuous density of states, which depends on the junction geometry. On the contrary, in a "clean" system the reflection and transmission properties at the interface play an important role which complicate the equations and the determination of the boundary conditions. In this limit, discrete states are formed which carry the supercurrent.

The milestone in understanding low temperature superconductors starts with the Bardeen, Cooper and Schrieffer (BCS) theory[11] in 1957. Next, in 1959, Gor'kov[12] presented a set of equations that completely described the stationary behavior of type II superconductors. It was necessary a decade (1968) for Eilenberger[13] to show that the highly complicated general equations of Gorkov may be transformed into a simpler set which, when linearized, yielded transport-like equations. In 1970, Usadel[14] reduced the Eilenberger equations to an even simpler equation, which is only valid in the "dirty" limit and can be seen as a generalization of de Gennes' diffusion equation to arbitrary values of the order parameter $\Delta(T)$. In other words, Usadel's equation reduces de Gennes' equation if $\Delta(T) \ll K_B T_c$, that is, $T \sim T_c$. On the other hand, the starting point of P.G. de Gennes[15] (1964) was the phenomenological Ginzburg-Landau theory[16] (1950) that Gorkov (1959) was able to show to be a limiting form of the BCS microscopy theory.

In his treatment, Usadel defined the "dirty" limit condition as

$$l \ll \frac{\hbar v_F}{K T_c} \equiv \xi_o. \tag{4.19}$$

Applied to a weak link, l is the electron mean free path in the normal metal, v_F the Fermi velocity and T_c is the transition temperature of the superconducting electrodes. The characteristic length $\hbar v_F / K T_c \equiv \xi_o$ is the coherence length introduced by Pippard, which represents the smallest size of a wave packet that the superconducting charge carriers can form. It can be estimated considering that, at T_c, only electrons in an interval of $\sim KT_c$ around the Fermi energy can play a role; these electrons have a momentum range $\Delta p \sim KT_c / v_F$.

[11] J. Bardeen, L. N. Cooper and J. R. Schrieffer, *Theory of superconductivity*, Phys. Rev. **108**, 1175 (1957).

[12] L. P. Gor'kov, *Theory of superconducting alloys in a strong magnetic field near the critical temperature*, Sov. Phys. JETP **10**, 998 (1960).

[13] G. Eilenberger, *Transformation of Gorkov's equation for type II superconductors into transport-like equations*, Z. Phys. **214**, 195 (1968).

[14] K. D. Usadel, *Generalized diffusion equation for superconducting alloys*, Phys. Rev. Lett. **25**, 507 (1970).

[15] P. G. de Gennes, *Boundary effects in superconductors*, Rev. Mod. Phys. **36**, 225 (1964).

[16] V. L. Ginzburg, L. D. Landau *On the theory of superconductivity*, Zh. Eksperim. i Teor. Fiz. **20**, 1064 (1950).

Thus, using the uncertainty principle, we have $\Delta x \sim \hbar/\Delta p \sim \hbar v_F/KT_c$. The condition 4.19 is equivalent to

$$l \ll \sqrt{\frac{\hbar l v_F}{6\pi KT}} = \sqrt{\frac{\hbar D}{2\pi KT}} \equiv \xi_n(T) \tag{4.20}$$

where $D = \frac{1}{3} l v_F$ is a diffusion-like constant. Relation 4.20 is mainly used as a condition for the "dirty" limit in proximity superconducting weak links.

The characteristic length ξ_n is also used to define the long and short limits of a junction: if $L \ll \xi_n(T)$, where L is the length of the link (distance between the superconductors) it is said that the junction is short; on the contrary, if $L \gg \xi_n(T)$ it is said that the junction is long.

Hence, before using a theoretical prediction for the critical current of a junction it is mandatory to know two microscopic parameters: the electron mean free path of the normal metal and the length of the link. The later can be measured directly, and the former can be obtained from resistivity measurements using the relation[17]

$$l\rho = K, \tag{4.21}$$

where K is a characteristic constant for each material. Note that relation 4.21 is applicable only to a bulk material. Resistivity measurements by E.V.Barnat et al.[18] during sputter deposition of copper films at room temperature indicate that the electrical resistivity becomes a weak function of thickness above 20 nm. But, at low temperatures the surface effects in a thicker film may be important; in fact, the film thickness imposes an upper limit to the mean free path. In our case, with a film thickness of $100nm$, we can consider the geometry is the limiting factor in the electron mean free path, then $l = 100nm$. Taking into account the Fermi velocity is $1.58 \times 10^6 m/s$ for copper and $T_c = 9.2K$ for Nb, by substituting this values in 4.19 one obtains $\xi_o = 1\mu m$. Hence, if the above estimations are valid, we could conclude that our sample is likely to be in the dirty limit. But to decide if the junction is in the long or short limit is not so clear since $L = 1\mu m \sim \xi_o$.

4.2.5.1 De Gennes' and Likharev prediction for the critical current

De Gennes' prediction for the critical current of a SNS junction is based in the following assumptions:

a) $T \to T_c$.

b) Dirty limit ($l \ll \xi_n(T_c)$).

c) Long junction ($L \gg \xi_n(T_c)$).

[17] N. W. Ashcroft and N. D. Mermin *Solid State Physics*, Harcourt (1976).

[18] E. V. Barnat, D. Nagakura, P. I. Wang and T. M. Lu, *Real time resistivity measurements during sputter deposition of ultrathin copper films*, J. Appl. Phys. **91**, 1667 (2002).

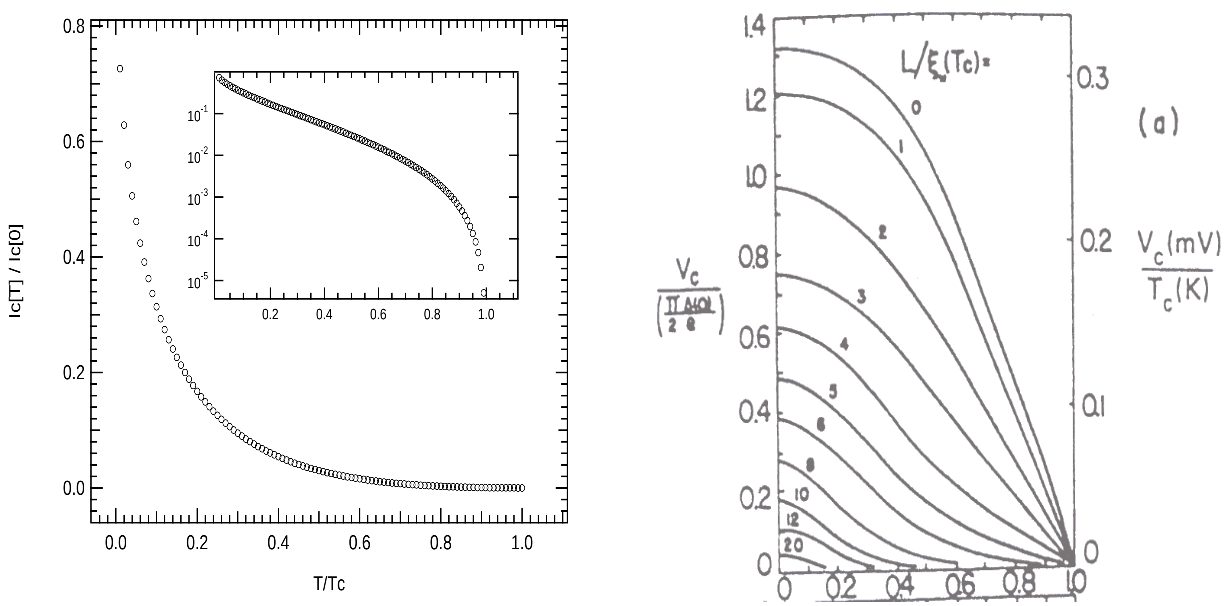

Figure 4.10: Left: de Gennes critical current prediction; a log plot is shown inside. Right: Likharev critical current prediction for different values of the ratio L/ξ_n. Data represented as a function of the reduced temperature T/Tc, where $V_c = I_c R_N$.

The temperature dependence of the critical junction can be expressed as

$$I_c(T) = I_{co}\left(1 - \frac{T}{T_c}\right)^2 e^{-\frac{L}{\xi_n(T)}} = \frac{I_{co}}{T_c^2}(T - T_c)^2 e^{-\alpha\sqrt{T}} \tag{4.22}$$

where we have used $\xi_n(T) = \sqrt{\frac{\hbar D}{2\pi KT}}$. If we put typical values for $l = 100nm$ (for thin films the mean free path is limited by the film thickness), $v_F = 10^6 m/s$, $L = 1\mu m$ and $T_c = 8.6$ K we obtain $\alpha \sim 1$. A representation of 4.22, where we have used these values, is shown in figure 4.10(left). By comparing with the experimental result of figure 4.7 we see that both present the same behavior, that is, an exponential dependence at low temperatures and a sudden drop close to the transition. But, the fundamental difference is that in our sample the critical temperature is not close to the critical temperature of the niobium superconductor banks (8.6 K). This behavior will be explained bellow.

In 1976 Likharev[19] presented an extension of the theory which is valid in the dirty limit for temperatures down to zero, and for any length of the junction, see Fig. 4.10. The results, except for T close to Tc, were obtained numerically.

The ratio $L/\xi_N(T_c)$ has a great influence on the critical current. For high $L/\xi_N(T_c)$ values the critical current is drastically reduced. Since the decrease of the junction length ($L \approx 1\mu m$) is difficult to fulfill, we decide to increase the diffusion length ξ_n via an increase of the electron

[19] K. K. Likharev *The relation $J_s(\phi)$ for SNS bridges of variable thickness*, Sov. Tech. Phys. Lett. **2**, 12 (1976). K. K. Likharev *Superconducting weak links*, Rev. Mod. Phys. **51**, 101 (1979).

mean free path in the normal bridge, which was done by increasing the thickness of the copper film from 100 nm in sample #060916 to 300 nm in sample #070307. Notice that, as shown in Figs. 4.7 and **??**, the temperature dependence of the critical current shifted as expected.

Finally, and from a practical point of view, we could conclude that in order to fabricate a SNS Josephson junction with a high transition temperature a normal metal thickness greater than 300 nm is suitable (for a standard fixed junction length of $\sim 1\mu m$) in order to decrease the ratio $\frac{L}{\xi_n(T_c)}$.

4.2.5.2 Zaikin-Zharkov prediction for the critical current

An analytical expression for the critical current of long ($L \gg \xi_n(T_c)$) dirty ($l \ll \xi_n(T_c)$) SNS junctions was derived by Zaikin and Zharkov[20]. The critical current in this theory is expressed as

$$I_c(T) = \frac{32}{3+2\sqrt{2}} \frac{2\pi K_B T}{e\, R_N} \frac{L}{\xi_n(T)}\, e^{-\frac{L}{\xi_n(T)}}, \tag{4.23}$$

where R_N is the resistance of the normal metal bridge. The above expression is valid in an intermediate range of temperatures $10mK < T < T_c$, where T_c is the critical temperature of the superconducting electrodes. It should be also emphasized that this theory is valid for ideal normal-superconductor interfaces[21], by ideal one means that the resistance of the interface is negligible relative to the resistance of the normal metal in the junction, as in our case (lateral junctions) if the deposition of both materials is made without breaking the vacuum.

One can rewrite the Eq. 4.23 in a more compact form as

$$I_c(T)[\mu A] = 10^6\, \frac{3.025}{R_N[m\Omega]}\, A\, T^{3/2}\, e^{-A\sqrt{T}}, \tag{4.24}$$

where

$$\frac{L}{\xi_n(T)} = A\sqrt{T} \qquad , \qquad A^2 = \frac{2\pi K_B L^2}{\hbar D}. \tag{4.25}$$

We used Eq. 4.24 to fit the exponential dependence of the data corresponding to sample #060916. The best-fit parameters were R_N=55 $m\Omega$, which is of the same order of the measured value (80 $m\Omega$) and A=8.5 K$^{-1/2}$, see Fig. 4.11. We obtain, using 4.25, $\frac{L}{\xi_n(T_c)}$=25 with T_c=8.6 K for the Nb film. We remark that in the framework of Likharev's theory the measured temperature dependence of the critical current is consistent with a high $\frac{L}{\xi_n(T_c)}$ ratio.

[20] A. D. Zaikin and G. F. Zharkov, *Theory of wide dirty SNS junctions*, Sov. J. Low Temp. Phys. **7(3)**, 184 (1980). F. Wilhelm, A. Zaikin and G. Schon, *SNS-model for the transport of a supercurrent in proximity wires*, J. Low Temp. Phys. **106**, 305 (1997). P. Dubos, H. Courtois, B. Pannetier, F. K. Wilhelm, A. D. Zaikin and G. Schon, *Josephson critical current in a long mesoscopic SNS junction*, Phys. Rev. Lett. **63**, 064502 (2001).

[21] Y. Blum, A. Tsukernik, M. Karpovski and A. Palevski, *Critical current in Nb-Cu-Nb junctions with nonideal interfaces*, Phys. Rev. B **70**, 214501 (2004).

	KT	$\Phi_o I_c(T)/2\pi$
B	$3.19\ 10^{-23}$ J	$3.84\ 10^{-21}$ J

Table 4.1: Thermal energy vs. Josephson energy.

Following the same theory of Zaikin-Zharkov, the zero temperature critical current for a long junction is expressed as $I_c(T=0) = 10.82\epsilon_c/eR_N$, which gives $I_c(T=0) = 1.49\ mA$ if $T_c = 8.6\ K$. For comparison, we also show in Fig. 4.11 a fit to the de Gennes critical current (Eq. 4.22), which gives $I_c(T=0) = 29.6\ mA$ and $\frac{L}{\xi_n(T_c)}$=15.8 if we use a T_c=8.6 K. Notice the over estimation for the critical current at T=0 of de Gennes' prediction (29.6 mA versus the 1.4 mA of Zaikin's theory); but as said before, de Gennes' theory is only valid at temperatures close to the superconductor critical temperature.

We should like to remark that the drastic diminution of the measured critical current, which is more evident in the log plot of Fig. 4.11, can not be due to thermal fluctuations. Table 4.1 compares the two energies in competition, the thermal energy KT and the Josephson energy $\Phi_o I_c(T)/2\pi$. So, in point B, one has $\Phi_o I_c(T)/2\pi \sim 100KT$.

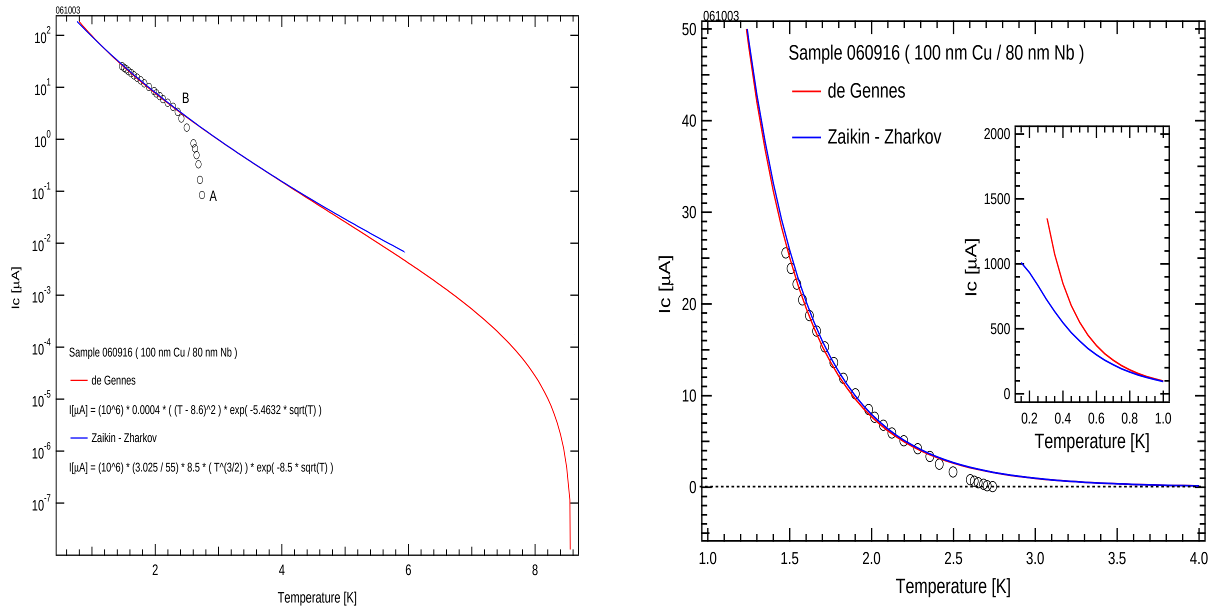

Figure 4.11: Temperature dependence (left:log plot; right: linear plot) of measured critical current for sample #060916 and fit to the theoretical predictions of de Gennes (Eq. 4.22) and Zaikin-Zharkov (Eq. 4.24).

4.3 The inductively and resistively shunted junction (IRSJ) model

In this section we derive the equation which describes quantitatively the dynamics of our device: a single SNS Josephson junction short circuited by a superconducting loop driven by an alternating magnetic field.

From the DC measurements of the previous section (see Fig. 4.4) it is clear that the current I through the sample loop undergoes jumps. Therefore, the total flux Φ through the sample loop also undergoes jumps since $\Phi = \Phi_x + LI$, we remember Φ_x is the external applied magnetic flux and L is the self inductance of the superconducting sample loop.

The Josephson junction we have fabricated is inherently shunted by a finite normal resistance R. Hence, the natural extension of the previous model is to incorporate such resistance in parallel with the junction[22] as shown in Fig. 4.12.

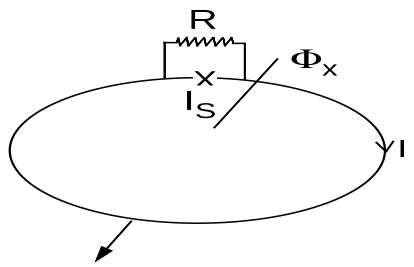

Figure 4.12: A resistively shunted Josephson junction embedded in a superconducting ring of self inductance L in an applied flux Φ_x.

We can expect that an e.m.f. will be induced in the sample loop due to the changes in the total flux Φ. The e.m.f is given by the Faraday law as

$$\oint \mathbf{E}\, d\mathbf{l} = -\dot{\Phi}$$

We may place the integration path so deep in the interior of the superconducting loop that the electric field $\mathbf{E}$ vanishes[a]. In this case

$$-\dot{\Phi} = \oint \mathbf{E}\, d\mathbf{l} = \int_R \mathbf{E}\, d\mathbf{l} = V$$

[a] F. London, *Superfluids (Vol. I)*, Dover (1961).

where V is the voltage across the junction, which is given by Ohm's Law as

$$V = R\, I_R \tag{4.26}$$

where I_R is the current flowing through the normal shunt, and R its resistance. Thus, we obtain

$$I_R = \frac{V}{R} = -\frac{\dot{\Phi}}{R} \tag{4.27}$$

[22] W. C. Stewart, *Current-Voltage characteristics of Josephson junctions*, Appl. Phys. Lett. **12**, 277 (1968). D. E. McCumber, *Effect of ac impedance on dc Voltage-Current characteristics of superconductor weak link junctions*, J. Appl. Phys. **39**, 3113 (1968).

This term takes into account, via the resistance R, the dissipation due to whatever total flux variation $\dot{\Phi}$ through the sample loop. The total circulating current I is the sum of the supercurrent I_S flowing through the junction and the current I_R flowing through the normal shunt, that is

$$I = I_S + I_R \tag{4.28}$$

Hence, the only difference with the model of the previous section is that now one has an additional term on the right side of Eq. 4.17. Since Eqs. 4.13 to 4.16 are still valid, we can finally write

$$\frac{1}{L}\Phi - \frac{\Phi_x}{L} = I_c(T)\sin(-2\pi\,\frac{\Phi}{\Phi_o}) - \frac{\dot{\Phi}}{R} \tag{4.29}$$

This is a nonlinear first order differential equation that can be solved numerically to obtain $\Phi(t)$, and hence to determine the total current through the loop as

$$I(t) = \frac{1}{L}(\Phi(t) - \Phi_x(t)) \tag{4.30}$$

where the sinusoidal external applied flux can be written as

$$\Phi_x(t) = \Phi_{xo}\ \sin(2\pi\nu t). \tag{4.31}$$

In order to determine the relevant parameters of the problem it is beneficial to rewrite Eq. 4.29 in a dimensionless form

$$\dot{f} + \lambda\sin(2\pi f) = f_{xo}\sin(2\pi\nu_N\tau) - f \tag{4.32}$$

where the normalized parameters are

$$f = \frac{\Phi}{\Phi_o} \quad , \quad f_{xo} = \frac{\Phi_{xo}}{\Phi_o} \quad , \quad \lambda = \frac{LI_c(T)}{\Phi_o} \quad , \quad \tau = \frac{R}{L}t \quad \text{and} \quad \nu_N = \frac{L}{R}\nu, \tag{4.33}$$

notice that $\dot{f} = \frac{df}{d\tau}$. The Eq. 4.32 has been implemented in Mathematica and solved numerically in a discretized interval of temperature to obtain corresponding solutions for $f(\tau)$. As initial condition we used $f(\tau = 0) = 0$, but solutions are not sensitive to this particular choice. In this way, solutions for the current through the superconducting loop are obtained via Eq. 4.30

$$\frac{I(t)}{\Phi_o} = \frac{1}{L}\left(\frac{\Phi(t)}{\Phi_o} - \frac{\Phi_x(t)}{\Phi_o}\right) \tag{4.34}$$

and with $t = \tau\frac{L}{R}$ one has

$$\frac{I(\tau\frac{L}{R})}{\Phi_o} = \frac{1}{L}\left(\frac{\Phi(\tau\frac{L}{R})}{\Phi_o} - \frac{\Phi_x(\tau\frac{L}{R})}{\Phi_o}\right) \tag{4.35}$$

or

$$i(\tau) = \frac{\Phi_o}{L}(f(\tau) - f_x(\tau)) \tag{4.36}$$

where we have defined $f_x(\tau)$ from Eq. 4.31 as

$$\frac{\Phi_x(t)}{\Phi_o} = \frac{\Phi_x(\tau\frac{L}{R})}{\Phi_o} = \frac{\Phi_{xo}}{\Phi_o}\sin(2\pi\nu\frac{L}{R}\tau) =: f_x(\tau). \tag{4.37}$$

and in the same way

$$\frac{\Phi(t)}{\Phi_o} = \frac{\Phi(\tau\frac{L}{R})}{\Phi_o} =: f(\tau) \quad , \quad I(t) = I(\tau\frac{L}{R}) =: i(\tau). \tag{4.38}$$

Eq. 4.36 allows us to determine the loop current from the solution $f(\tau)$ of the differential equation 4.32 . Finally, by rewriting the Fourier transforms (Eqs. 2.15) in the new parametrization we obtain the real and imaginary components of the signal as

$$X_n = \frac{2}{1/\nu_N}\int_0^{1/\nu_N} K\, i(\tau)\cos(2\pi n\nu_N\tau)d\tau, \qquad n = 0, 1, 2... \tag{4.39}$$

$$Y_n = \frac{2}{1/\nu_N}\int_0^{1/\nu_N} K\, i(\tau)\sin(2\pi n\nu_N\tau)d\tau, \qquad n = 1, 2... \tag{4.40}$$

These values can be compared with the experimental data supplied by the lock-in.

The fixed parameters used in the differential equation 4.32 are

a) the *measured* critical current $I_c(T)$.

b) the amplitude Φ_{xo} and the frequency ν of the drive flux.

c) the self inductance L of the sample loop, which in a first attempt was calculated (4 nH), but later measured (21 nH).

d) the shunt resistance R of the junction.

4.3.1 First attempts to simulate the experimental results

The aim of this section is to study the general behavior of the differential equation 4.32 in order to compare its solutions with the main features of the experimental data. At first, the following inputs were used to run the simulation:

a) the *theoretical* critical current: $I_c(T) = I_o(1 - T/T_c)^2 e^{-4\sqrt{T}}$, with $I_o = 0.1\ A$ and $T_c = 8.5\ K$.

b) the amplitude and frequency of the applied flux were $\Phi_{xo} = 25\ \Phi_o$ and $\nu = 5\ Hz$.

c) the *calculated* self inductance of the superconducting loop: $L = 4\ nH$.

d) the shunt resistance of the junction: $R = 10\ \mu\Omega$; this low value was used in order to reduce computation time.

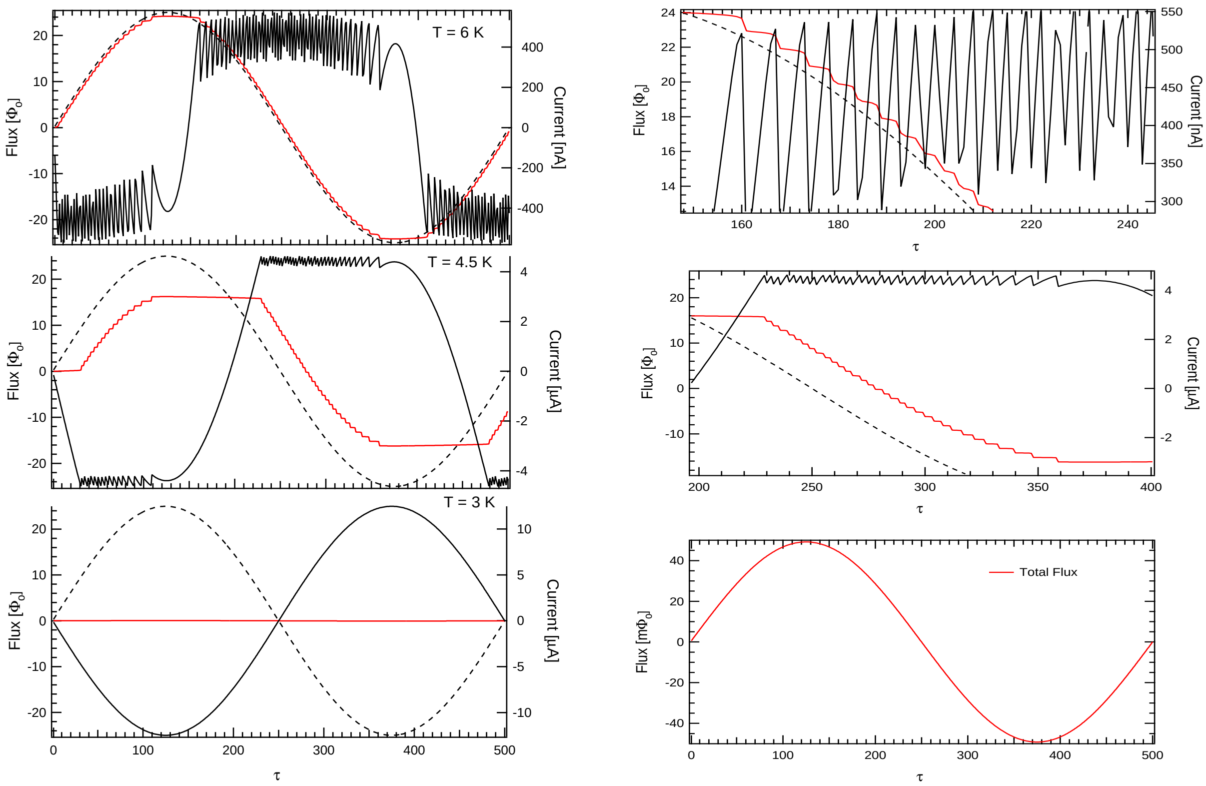

Figure 4.13: Left: applied flux Φ_x(dashed), total flux Φ(red) and total current I(black) at three different temperatures as a function of the rescaled time $\tau = \frac{R}{L}t$. Right: respective zooms.

Figure 4.13 shows the solution of Eq. 4.32, that is, the temporal dependence of the total flux $\Phi(\tau) = f(\tau)\Phi_o$ on the sample loop for three values of the temperature. In this figure, the applied flux $\Phi_x(t) = \Phi_{xo}\ \sin(2\pi\nu t)$ and the total current flowing through the sample loop, which is obtained via Eq. 4.36, are also showed.

The following comments can be made:

- The response (total current through the sample) to a sinusoidal excitation is not sinusoidal except at low temperatures or low excitations ($\Phi_x < LI_c$).
- By decreasing the temperature a phase difference between the applied flux and the total flux on the sample is observed.
- The sample maintains the fluxoid constant until the critical current is reached; at this moment a series of jumps starts up.

The simulated phase sensitive measurements of our device is shown in Fig. 4.14. The inductive (Y) and dissipative (X) components are obtained from the total current via the Fourier transforms represented by Eq. 4.39, with $n = 1$ (first harmonic). In the same figure the temperature dependence of the magnitude and phase, calculated via Eq. 2.17, are also shown.

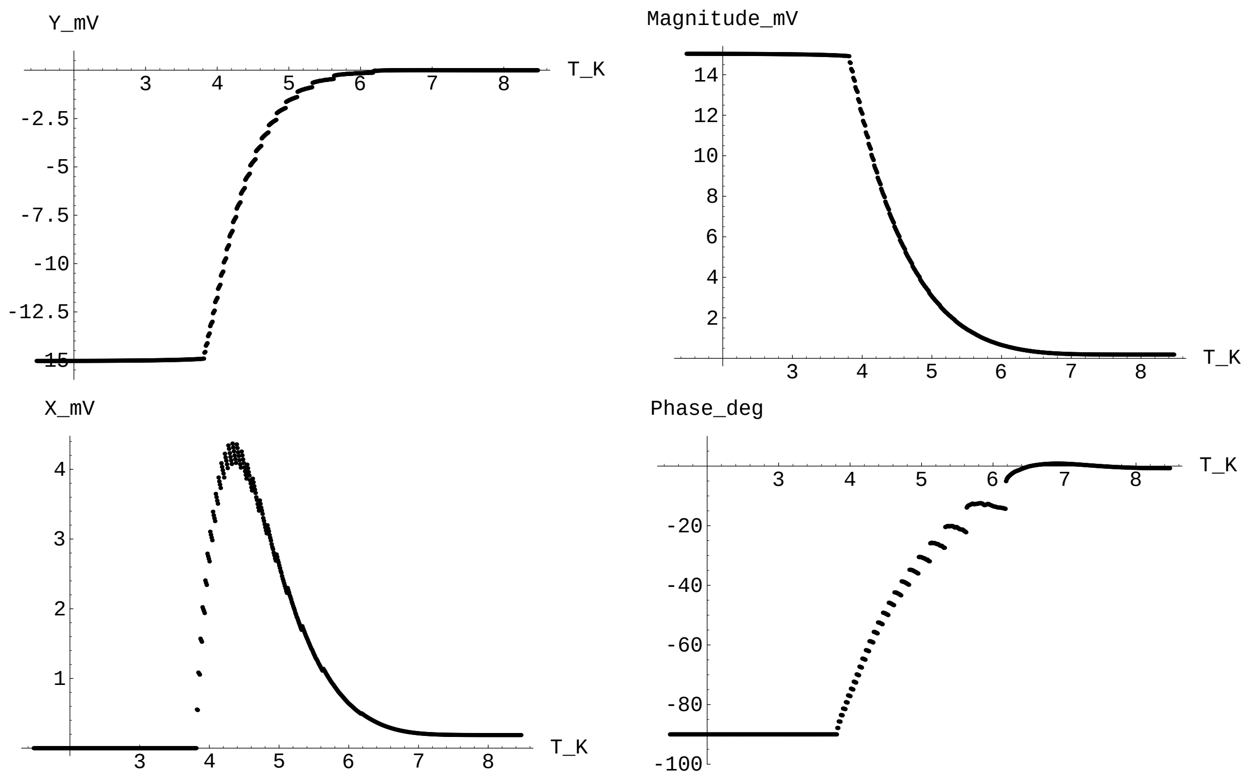

Figure 4.14: Left: simulated temperature dependence of the inductive (Y) and dissipative (X) components. Right: simulated temperature dependence of the magnitude and phase. The amplitude of the alternating applied flux is 25 Φ_o and its frequency is $\nu = 5\ Hz$

When comparing the numerical simulations of Fig. 4.14 with the experimental data shown in Fig. 4.1 we observe they are in a good qualitative agreement. However, one can notice that: first, the simulated phase presents steps which are not observed in the experimental data[23]. Second, the low temperature response is five times smaller. The fact that this quantitative disagreement is at low temperatures indicates that the problem is not the particular value of the resistance of the junction, since at low temperature we measure no dissipation. Moreover, notice that this factor has to be independent of the critical current amplitude at low temperatures and also of the frequency of excitation, see Fig. 4.3.

One possible source of error could be the estimation of the applied flux on the sample loop. However, the inductance calculations, which was corroborated by experimental measurements in non-superconducting coils discard this possibility, see Fig. 2.4. Furthermore, by observing Fig. 4.15 where DC measurements on two different samples are shown we see that the minimal jump in flux is a quantum of flux, but we also observe two, three, four jumps, etc., as is expected for an overdamped (capacitance$\rightarrow 0$) junction[24]. This corresponds very well with the scale on the abscise axes.

Therefore, such a disagreement comes from the calculated value of the self inductance L of the sample loop. It was calculated using the results of Appendix A and Eq. 2.3, taking into account the geometrical parameters of the loop. The calculated value was 4 nH. But, as can be seen at the end of Appendix A.3.2 a greater self inductance than the theoretical prediction is expected in this case. So, this is the aim of the following section: to determine experimentally the self inductance of the sample loop.

4.3.2 Determination of the self inductance of the sample loop

It is possible to determine the sample loop self inductance from both DC and AC measurements. By observing Fig. 4.13 we see that at low temperatures, when there is no jumps, $\Phi \ll \Phi_x$ and so, from Eq. 4.30, we can write

$$I(t) = -\frac{\Phi_x(t)}{L}, \tag{4.41}$$

that is, at low temperatures the total current through the sample loop is able to screen the external applied field (strong screening limit). This allows to determine the self inductance of the loop from the slope of the linear dependence that appears in the DC measurements. Figure 4.15 shows such measurements on two different samples, but in both cases with the same loop geometry. As expected, in both samples the slope of the straight lines is approximately the same. According to Eq. 4.41 the slope of this line is just 1/L. The measured self inductance

[23]Notice that the numbers of steps matches the number of quantum of flux we use to excite the sample (in this case 25).

[24]H. J. T. Smith and J. A. Blackburn, *Multiple quantum flux penetration in superconducting loops*, Phys. Rev. B **12**, 940 (1975).

(L∼20 nH) is five times greater than the calculate one (4 nH), and this is just the factor we need to get a good agreement between experimental and theoretical curves[25].

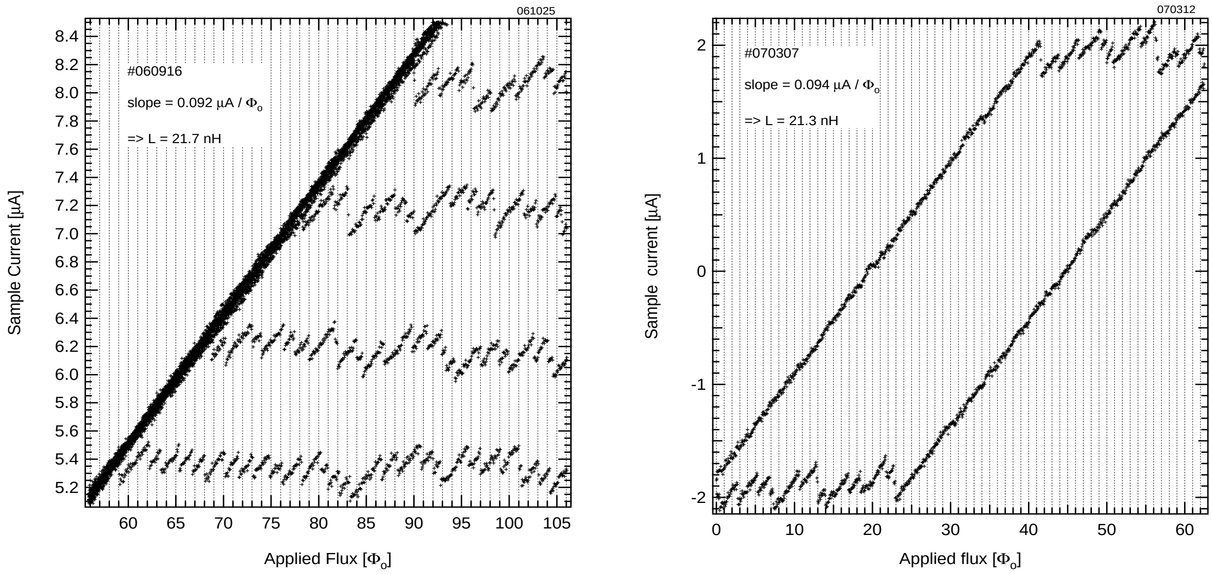

Figure 4.15: Left: self inductance of sample #060916(left) and sample #070307(right) deduced from DC measurements.

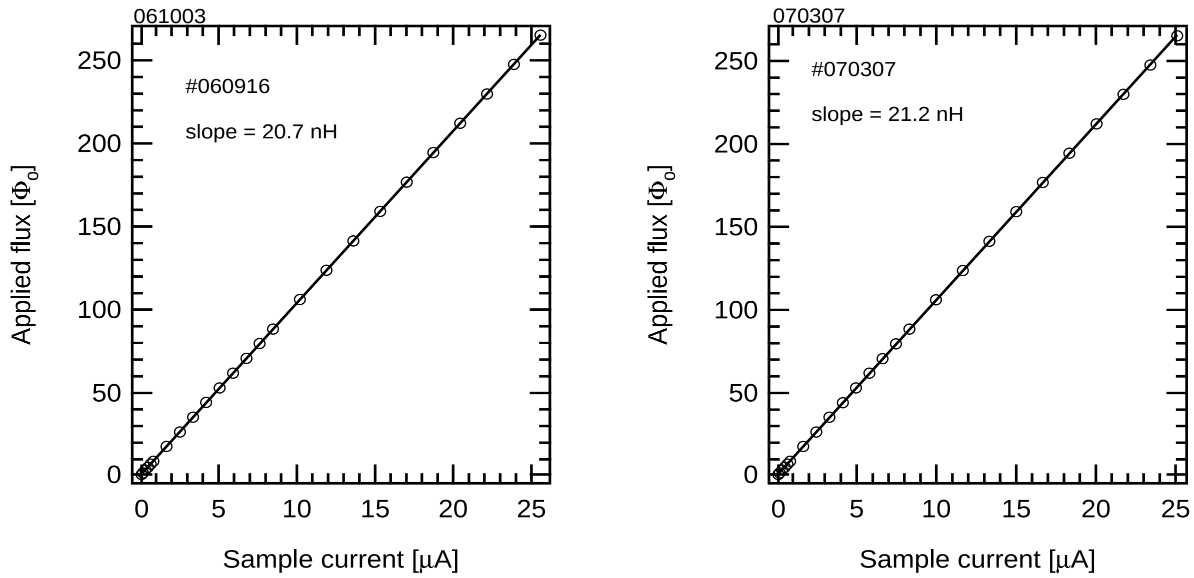

Figure 4.16: Left: self inductance of sample #060916 deduced from the AC measurements data of Fig. 4.5. Right: self inductance of sample #070307 deduced from the AC measurements data of Fig. 4.6.

[25]Although the receive gradiometer is also superconducting we expect its theoretical value be a good approximation because of its smaller wire diameter and the averaging effect of the mutual inductance between the different coil loops.

The self inductance of the sample can also be deduced from the AC measurements data. At a sufficient low temperature, that is, when the dissipation disappears, we are in the strong screening limit and so we can determine, for each curve which corresponds to a fixed applied flux, the screening current from the inductive component data. Fig. 4.16 shows the expected linear dependence between the measured applied flux and the sample current in such a limit for two different samples. The results from the AC measurements are in very good agreement with the DC measurements.

4.3.3 Experiments vs. theory

In order to compare the experimental data with the predicted values (Eqs. 4.39), calculated from the numerical solution of Eq. 4.29, the critical current is first extracted from the AC measurements, as described in Sec. 4.2.3. The frequency and amplitude of the applied flux are imposed externally for each run, so there are known. We also know the value of the self inductance of the sample loop $L = 21\ nH$, which was extracted from the DC or AC measurements, as shown in the previous section. So, the only "free" parameter is the resistance of the junction, and we used a estimated value of $R = 4\ m\Omega$ for all simulations but, as we will show in the following section, the value of the resistance does not change the numerical results as long as $R \geq 2\pi\nu\ L$. **Therefore, our simulations were carried out without adjusting parameters**.

In Figs. 4.17 and 4.18 a comparison between numerical simulations and measured data corresponding to the sample #060916 (100 nm Cu/80 nm Nb) are presented. Figure 4.19 shows a comparison between experimental and simulated data corresponding to sample #070307 (300 nm Cu/80 nm Nb). Magnitude and phase components are obtained from the inductive and dissipative components, therefore they give no additional information.

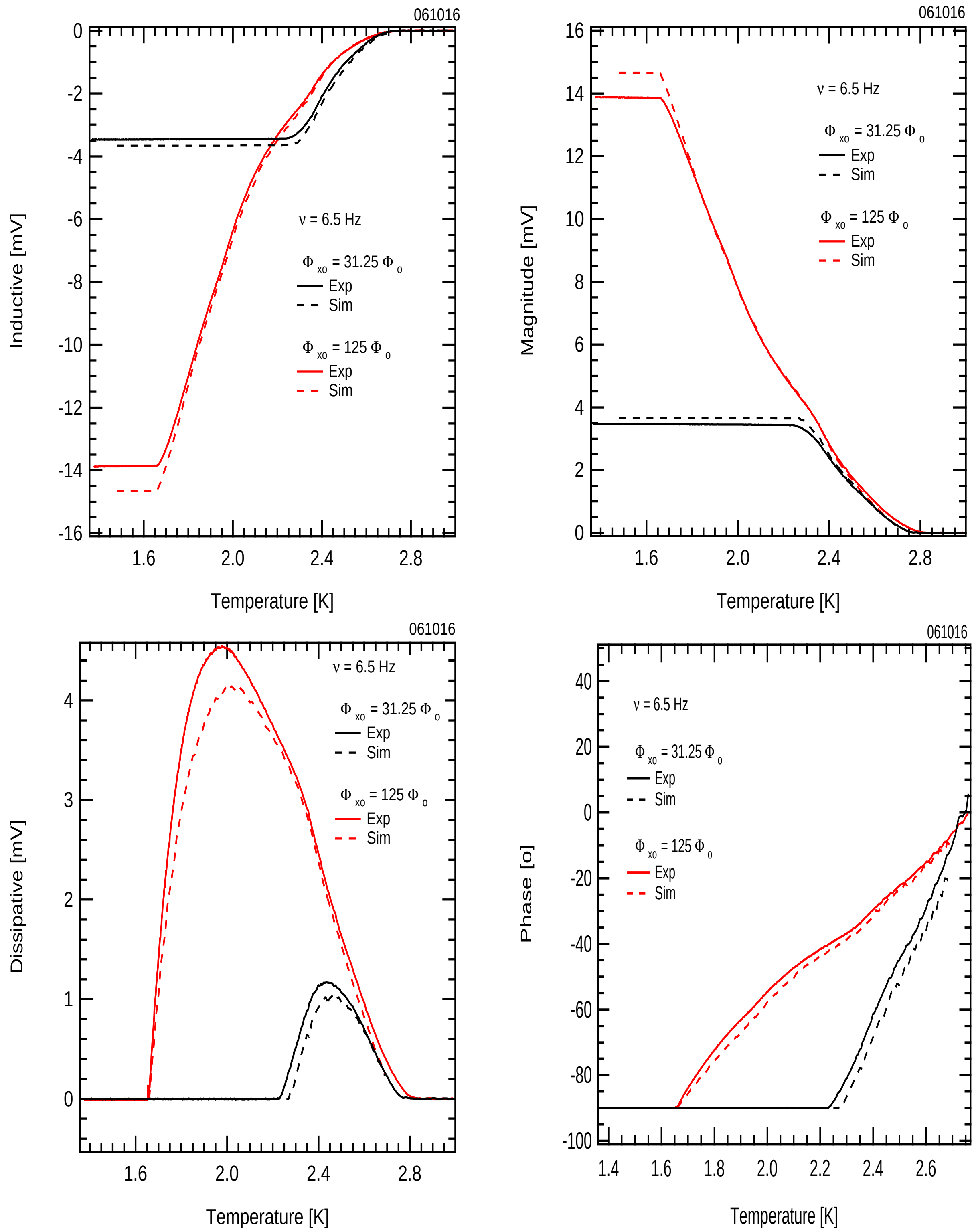

Figure 4.17: Comparison between the experimental and simulated data for two values of the amplitude of the applied flux ($31.25\Phi_o$ and $125\Phi_o$) at a frequency of $\nu = 6.5\ Hz$. The experimental data correspond to sample #060916 (100 nm Cu/80 nm Nb).

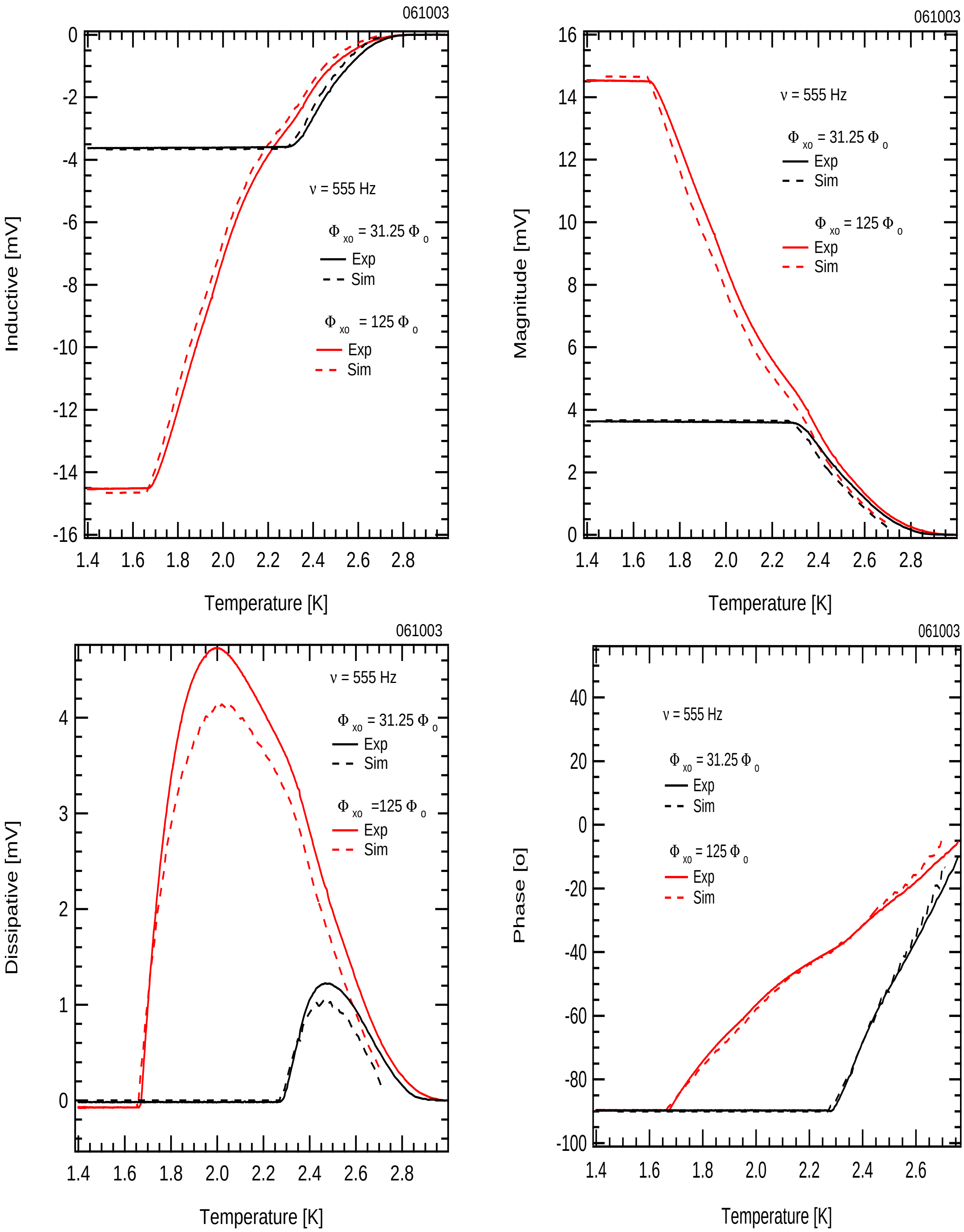

Figure 4.18: Comparison between the experimental and simulated data for two values of the amplitude of the applied flux ($31.25\Phi_o$ and $125\Phi_o$) at a frequency of $\nu = 555\ Hz$. The experimental data correspond to sample #060916 (100 nm Cu/80 nm Nb).

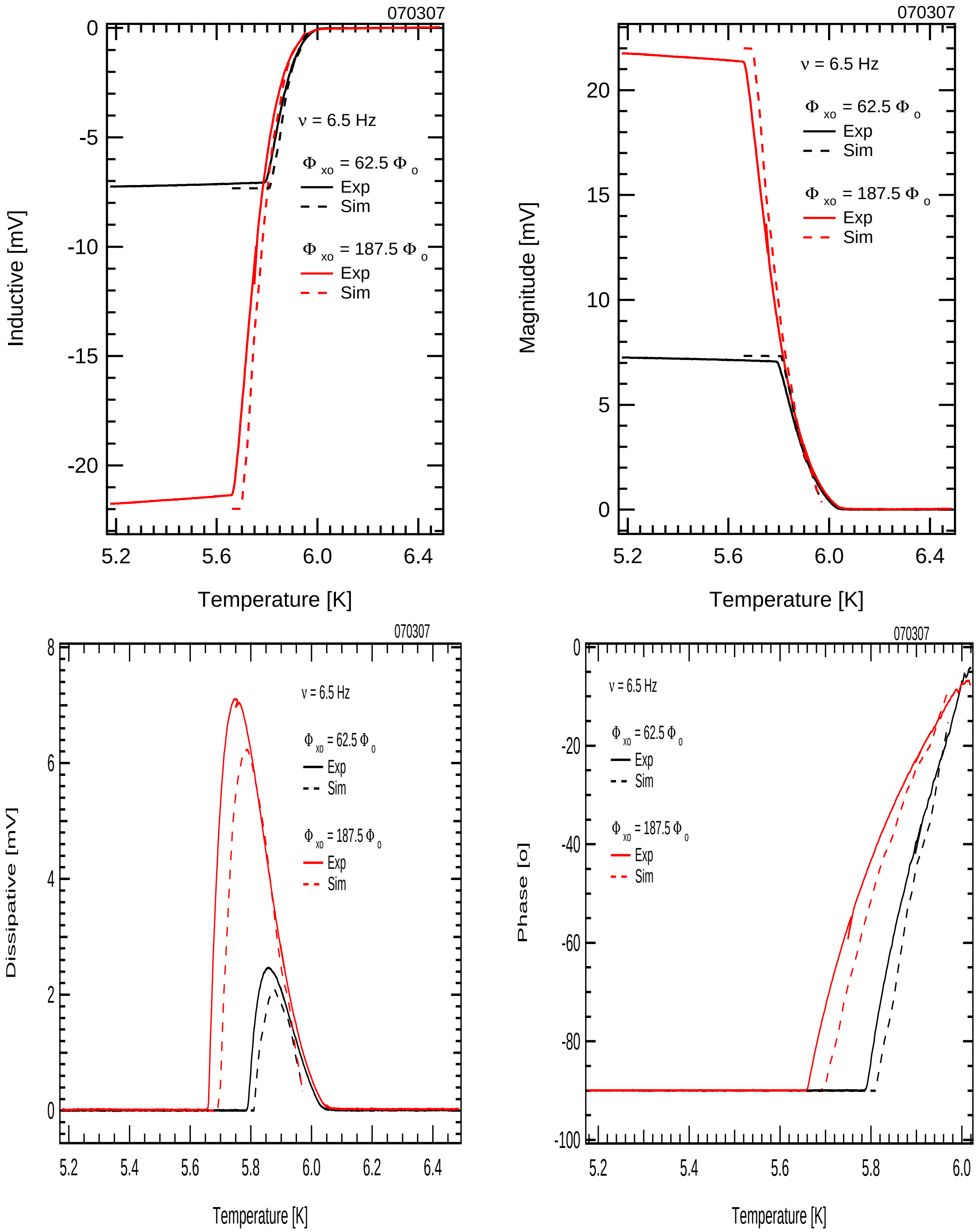

Figure 4.19: Comparison between the experimental and simulated data for two values of the amplitude of the applied flux ($62.5\Phi_o$ and $187.5\Phi_o$) at a frequency of $\nu = 6.5\ Hz$. The experimental data correspond to sample #070307 (300 nm Cu/80 nm Nb).

4.3.4 Frequency and resistance dependence

Figure 4.21 shows experimental data corresponding to sample #070307 (300 nm Cu/80 nm Nb). We observe a weak frequency dependence, but with a different behavior depending on the amplitude of the applied flux: for low values there is a shift in the dissipation curves, while for high values the shift is only observed in the high temperature region.

Figure 4.20 shows the simulations for a high amplitude of the applied flux. One observes that the effect of increasing ν is equivalent to decrease R, which is consistent with the fact that the resistance and the frequency appear in Eq. 4.32 as the ratio $\frac{\nu}{R}$. On the other hand, we observe that when $R \leq L2\pi\nu$ a shift in the high temperature region appears, which is in agreement with the measured data shown in Fig. 4.21(left).

Figure 4.22 shows the simulations for a low amplitude of the applied flux. When increasing the frequency (or by decreasing the resistance) a shift is observed. However, in order to explain the experimental shift we would need a very low resistance (0.04 mΩ), whose origin is not clear.

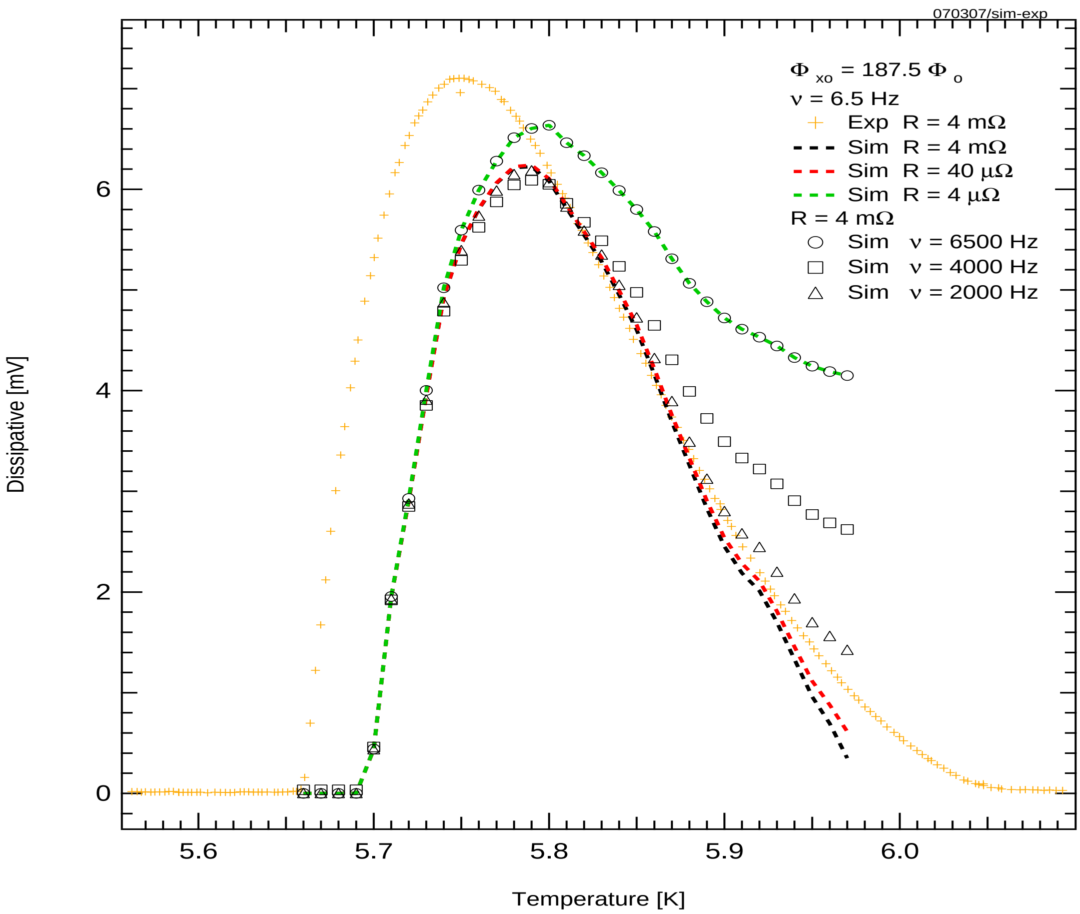

Figure 4.20: Influence of frequency and resistance of the junction on the simulated dissipative component. The experimental data (crosses) correspond to the sample #070307 (300 nm Cu/80 nm Nb).

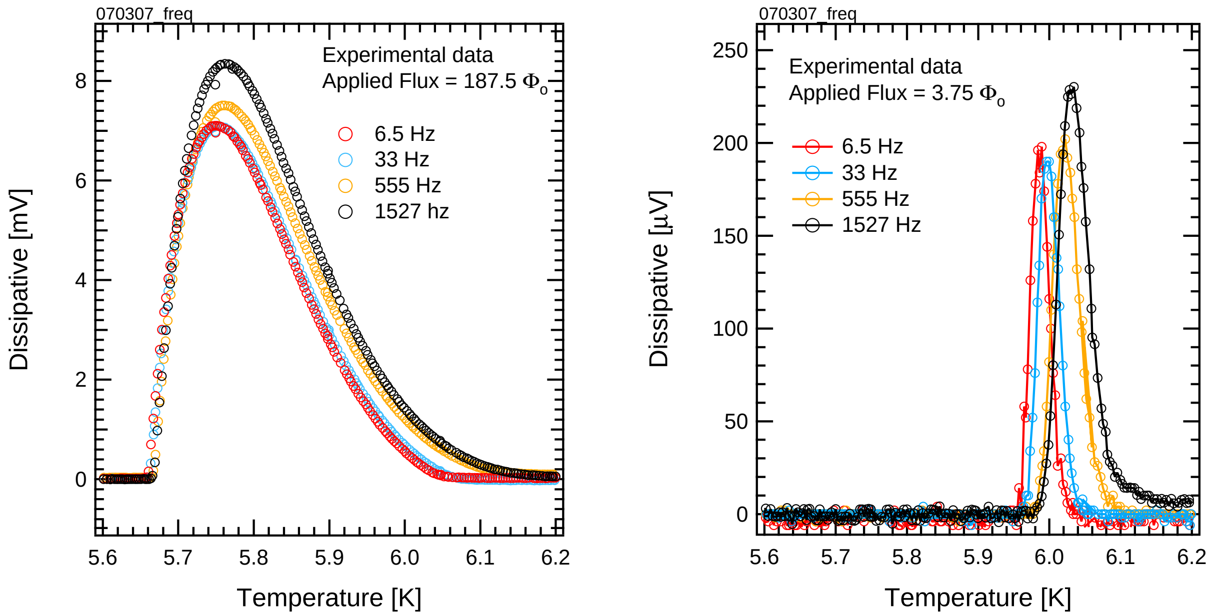

Figure 4.21: Influence of frequency on the measured dissipative component for two different amplitudes of the applied flux. The experimental data correspond to the sample #070307 (300 nm Cu/80 nm Nb).

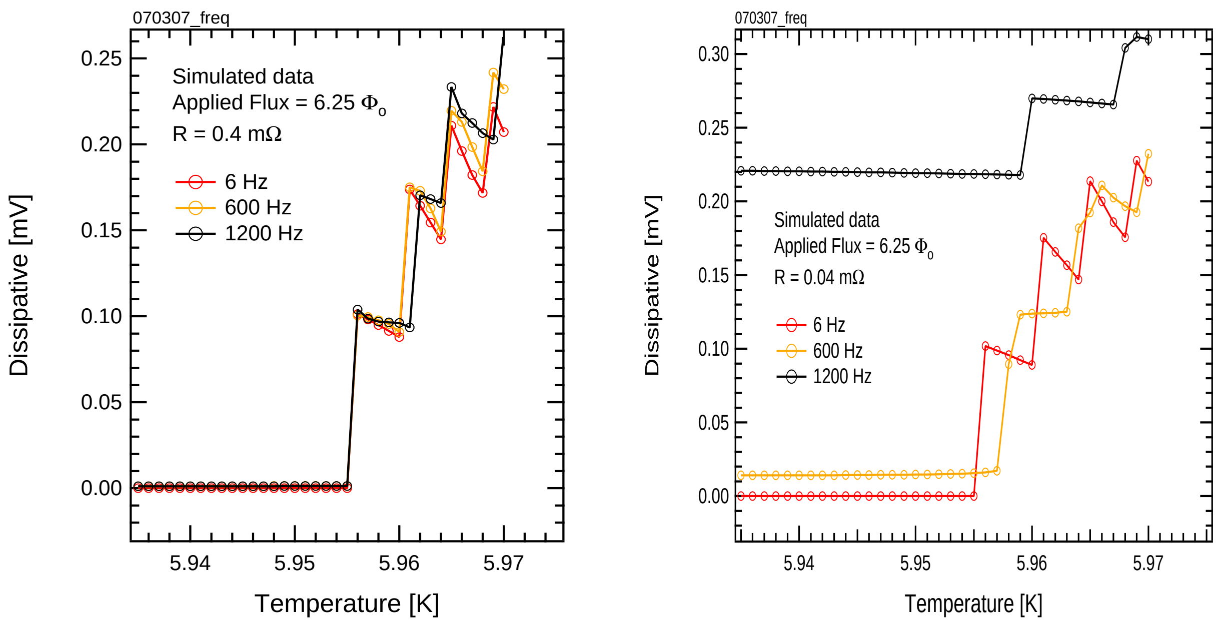

Figure 4.22: Influence of frequency on the simulated dissipative component for a small amplitude of the applied flux.

4.4 Conclusions

In order to understand the response of our device we started with a lumped circuit model consisting of a Josephson junction in series with a superconducting ring of self inductance L. This model leads to a useful graphical representation which explains qualitatively the principal features of the DC and AC measurements. In particular, it has been demonstrated that the source of the observed dissipation in the AC measurements is a series of jumps in the total flux and a series of hysteresis cycles that the sample undergoes when subjected to an alternating magnetic field.

A lumped circuit model, that takes into account the normal resistance of the junction and the dissipation, was utilized. The numerical solution, without adjusting parameters, of the corresponding differential equation is in very good quantitative agreement with the AC measurements.

It was also possible to extract the critical current of a Josephson junction. Two principal features were observed using the device consisting of a single Josephson junction embedded in a superconducting ring. Firstly, a sudden fall in the critical current near the temperature at which dissipation appears, and secondly, a dependence of this transition temperature on the thickness of the junctions normal metal. This behavior was found to be in good qualitative agreement with the Likharev's prediction for the critical current of a SNS Josephson junction.

Chapter 5

Inductive measurements on a magnetically shielded array of Josephson junctions

5.1 Introduction

The BKT transition in two-dimensional Josephson junction arrays is driven by the unbinding mechanism of thermally created vortex-antivortex pairs. The BKT theory, and its dynamical extensions, supposes a zero applied magnetic field on the array. With such a goal in mind, we have performed dc and ac measurements on a *niobium shielded* array of Josephson junctions embedded in a superconducting loop. The geometry of the fabricated array is shown in Fig.5.3.

We will see briefly[1] that the thermal generation of bound pairs of vortices is energetically favored, that there are no free vortices present at sufficiently low temperatures, and that free vortices will appear as thermal fluctuations above the BKT transition.

Consider two neighboring superconducting islands, with their superconducting wave functions $\Psi_j = \Psi_{oj}\exp(i\theta_j)$, and a Josephson junction connecting them. A phase difference $\theta_j - \theta_i$ corresponds to a supercurrent $I_s = I_c(T)\sin(\theta_j - \theta_i)$, where $I_c(T)$ is the junction critical current. The energy stored in a junction is given by $E_j(1 - \cos(\theta_j - \theta_i))$, where $E_j = \hbar I_c(T)/(2e) = \Phi_o I_c(T)/2\pi$ is called the Josephson (coupling) energy, the work necessary to bring the junction's phase from 0 to $\pi/2$ [2]. If the coupling energies are the same everywhere in the array and assuming zero applied magnetic field, the array Hamiltonian is simply given by the sum of the coupling energies of all the pairs $H = E_j \sum_{pairs}(1 - \cos(\theta_j - \theta_i))$.

Figure 5.1 represents a vortex in the array. The total phase difference around any closed path containing the center plaquette in the array is 2π.

---

[1] R. S. Newrock, C. J. Lobb, U. Geigenmller and M. Octavio, *The two-dimensional physics of Josephson junction arrays*, Sol. State Phys. **54**, 253 (2000). P. Martinoli and Ch. Leemann, *Two dimensional Josephson junction arrays*, J. Low Temp. Phys. **118**, 699 (2000).

[2] M. Tinkham*Introduction to superconductivity*, McGraw-Hill (1996).

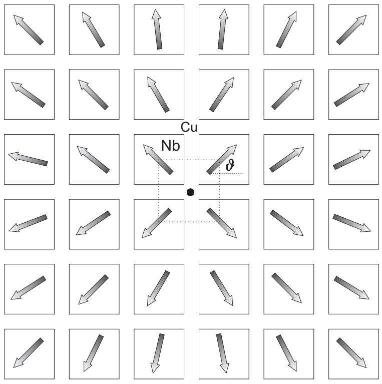

Figure 5.1: Phase configuration of a vortex.

$$\sum_{junctions} (\theta_j - \theta_i) = 2\pi \tag{5.1}$$

It is possible to calculate[3] the energy of such an isolated vortex in a large square array of size L to find $E_{vortex} = \pi E_j \ln(L/a)$, where a is the lattice spacing. So, the energy of a simple vortex increases logarithmically with sample size, its presence affecting all the spins. One can also calculate the energy of a vortex-antivortex pair, bound together a distance r apart; this has been shown to be $E_{pair} = 2\pi E_j \ln(r/a)$. In general, pairs with $r << L$ occur since $E_{pair} << E_{vortex}$. Hence, at any nonzero temperature it is much more probable that bound pairs of vortices will be thermally generated that single ones. Therefore, as one approaches the transition temperature from bellow, bound pairs are created, when increasing the temperature we will have more and more pairs of greater size, and at high temperatures, there will be sufficient thermal energy to unbind many of this pairs to create free vortices. The change in the free energy caused by the introduction of a single vortex in an array is $\Delta F = E_v - T\Delta S_v$, where $\Delta S_v = 2K_B \ln(L/a)$, since there are $(L/a)^2$ possible places for a vortex in the array. This leads to $\Delta F = (\pi E_j - 2K_B T)\ln(L/a)$. The probability of finding a single free vortex in the array will be

$$P_{free\ vortex} \sim e^{-\frac{(\pi E_j - 2K_B T)\ln(L/a)}{K_B T}} = \left(\frac{L}{a}\right)^{2-\frac{\pi E_j}{K_B T}}. \tag{5.2}$$

When the exponent in the second part of 5.2 reaches zero a free vortice appears, which defines the BKT transition

$$T_{BKT} = \frac{\pi E_j}{2K_B} \tag{5.3}$$

Since E_j is temperature dependent, Eq. 5.3 is an implicit expression for T_{BKT}

[3] C. J. Lobb, D. Abraham and M. Tinkham, *Theoretical interpretation of resistive transition data from arrays of superconducting weak links*, Phys. Rev B **27**, 150 (1983).

$$K_B T = \frac{\Phi_o I_c(T)}{4}, \tag{5.4}$$

where we have used $E_j = \Phi_o I_c(T)/2\pi$.

5.2 Results and discussion

A typical DC measurement is shown in Fig. 5.2. Like in the single junction case we also observe the characteristics jumps in the current as a function of the applied flux. We already know the origin of such jumps is the penetration into the ring of flux quantum once the induced supercurrent is not able to perform a perfect shielding. As expected, the lower the temperature, the greater the value of the critical current at which the jumps start. The behavior of the sample current vs. applied flux also is hysteretic, like in the single junction case. Therefore, both hysteresis and jumps are, in this particular geometry, additional sources of dissipation.

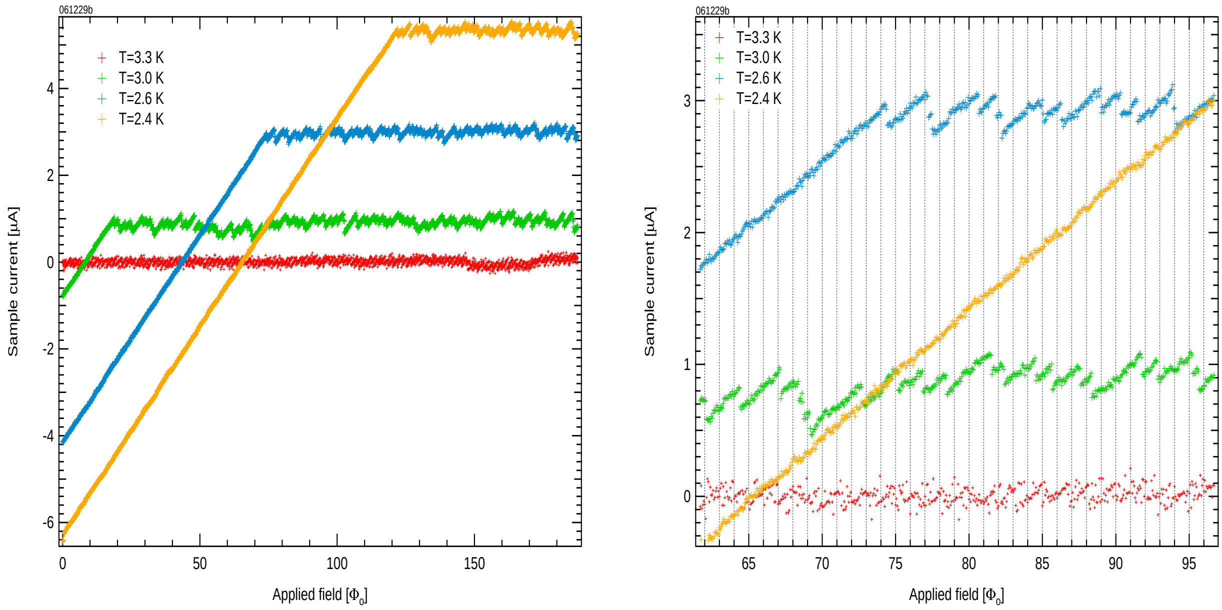

Figure 5.2: DC measurements: (left) current through the sample loop vs. applied field at different temperatures. The element embedded in the superconducting loop is an array of Josephson junctions. (Right) a zoom in the left figure.

According to the BKT transition mechanism, we will also have the dissipation due to the thermally generated vortices. Such hysteresis loops have also been predicted by D. Domínguez *et al.*[4] in the magnetization as a function of the applied flux for an array consisting of 30×30 junctions: "for small fields the magnetization decreases linearly corresponding to a Meissner state with an average vortex density equal to zero. After a critical field, vortices start penetring

[4]D. Dominguez and J. V. Jose, *Magnetic and transport dc properties of inductive Josephson junction arrays*, Phys. Rev. B **53**, 11692 (1996).

the array. For larger fields the magnetization has a sawtooth-like behavior of period Φ_o"(*sic*), see Fig. 14 in the cited paper. In their simulations the external field is applied directly on the array and the effect of self-induced magnetic fields were taken into account.

In Figs. 5.3 and 5.4 AC measurements at two frequencies (6.5 Hz and 555 Hz) and at different amplitudes as a function of temperature are shown. The behavior of these curves is similar to the one single junction case. As explained in Sec. 4.2.3, we have extracted the critical current of the array from AC measurements corresponding to 6.5, 33, 170 and 555 Hz. The results are shown in Fig. 5.5.

A graphical solution of Eq. 5.4 is presented in Fig. 5.5, the factor 275 comes from the fact that our array is made of 275×275 junctions, so the measured current through the loop is distributed over 275 channels. The predicted transition temperature is approximately 2.1 K, as shown in Fig.5.5.

Nothing particular is observed before or after T_{BKT}. The temperature dependence of the critical current is qualitatively the same as for a single junction. The response of the sample as a function of the frequency is shown in Fig. 5.6 in order to compare with the single junction case: for a high amplitude of the external applied flux there is a weak dependence in frequency at high temperatures and a collapse to a single curve at low temperatures, while for a low amplitude of the external applied flux the dissipative 'bump' moves toward greater values of temperature when increasing the frequency of the applied flux. This is in complete analogy to the behavior observed for a single junction, see Fig. 4.21.

We conclude that there is no clear evidence of a BKT transition in this system. One could think that the transition is hidden by the dissipation coming from the jumps observed on the DC measurements, but, by observing the measurements corresponding to a low amplitude of the applied flux, see Fig. 5.6, no signature of dissipation is observed above the predicted BKT transition temperature (2.1 K), except at a sufficient high temperature when the jumps start to appear. On the other hand, despite we have shielded the array from external magnetic fields in order to have no induced vortices, a drawback, intrinsic to the geometry of the system, arises: the measured entry of flux quantum into the superconducting loop is through the array itself. Therefore, these vortices will interact with the thermally induced vortex-antivortex of the BKT theory, and this interaction is not taken into account in such a theory. Once again, the measurement of the BKT transition has demonstrated to be an intrinsically difficult task.

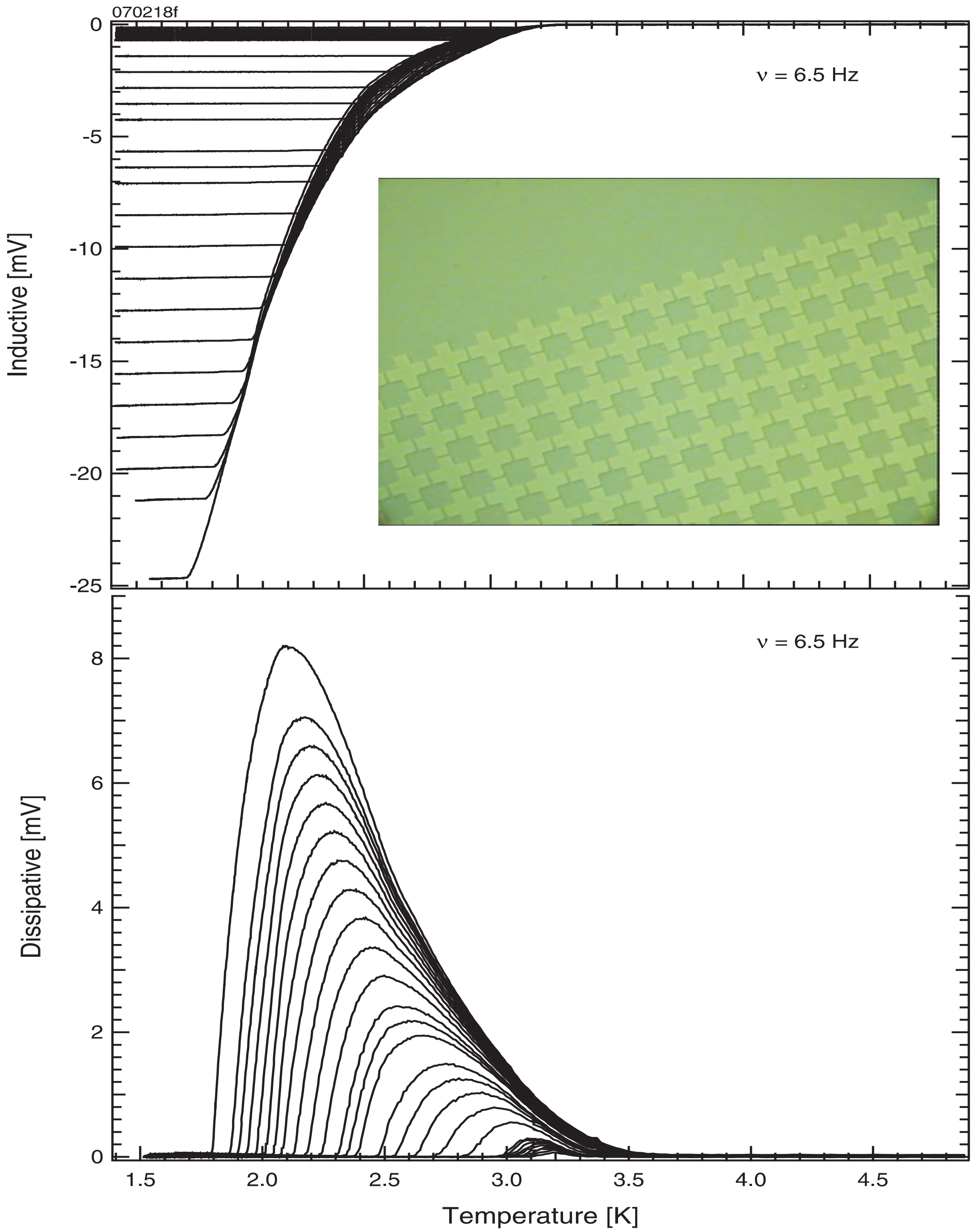

Figure 5.3: AC measurements at 6.5 Hz. Applied flux amplitudes, from the bottom up for the inductive component and from top to bottom for the dissipative component [$\times\sqrt{2}$ $62.5\Phi_o$]: (1)3.5 (2)3.0 (3)2.8 (4)2.6 (5)2.4 (6)2.2 (7)2.0 (8)1.8 (9)1.6 (10)1.4 (11)1.2 (12)1.0 (13)0.9 (14)0.8 (15)0.7 (16)0.6 (17)0.5 (18)0.4 (19)0.3 (20)0.2 (21)0.1 (22)0.09 (23)0.08 (24)0.07 (25)0.06 (26)0.05 (27)0.04 (28)0.03 (29)0.02.. Inside: optical image of the array (275 x 275 junctions; made of 200 nm Cu / 80 nm Nb). The length of each junction is 0.8 μm, its width is 3 μm and the lattice spacing is 9.8 μm.

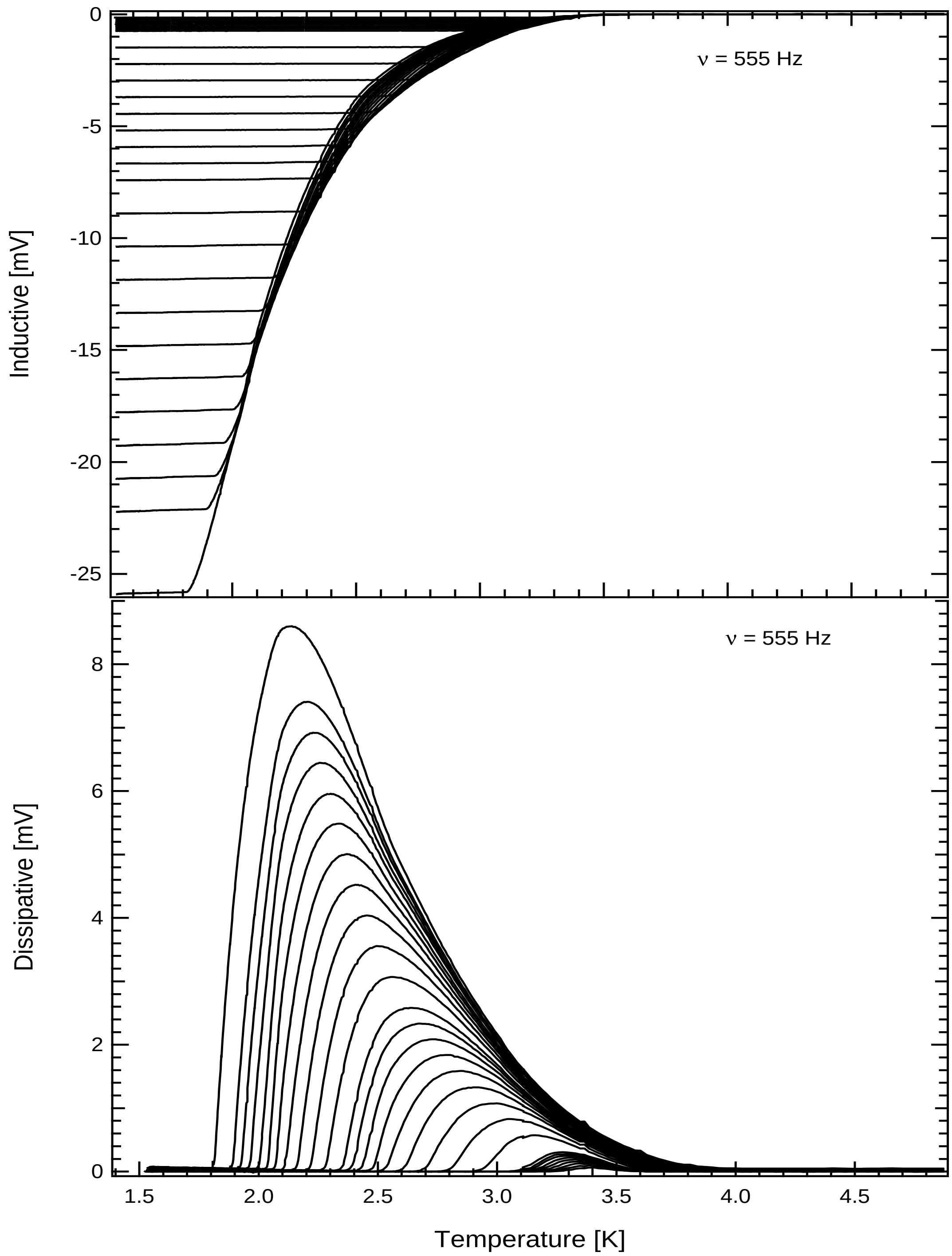

Figure 5.4: AC measurements at 555 Hz. Applied flux amplitudes, from the bottom up for the inductive component and from top to bottom for the dissipative component [$\times\sqrt{2}$ $62.5\Phi_o$]: (1)3.5 (2)3.0 (3)2.8 (4)2.6 (5)2.4 (6)2.2 (7)2.0 (8)1.8 (9)1.6 (10)1.4 (11)1.2 (12)1.0 (13)0.9 (14)0.8 (15)0.7 (16)0.6 (17)0.5 (18)0.4 (19)0.3 (20)0.2 (21)0.1 (22)0.09 (23)0.08 (24)0.07 (25)0.06 (26)0.05 (27)0.04 (28)0.03 (29)0.02.

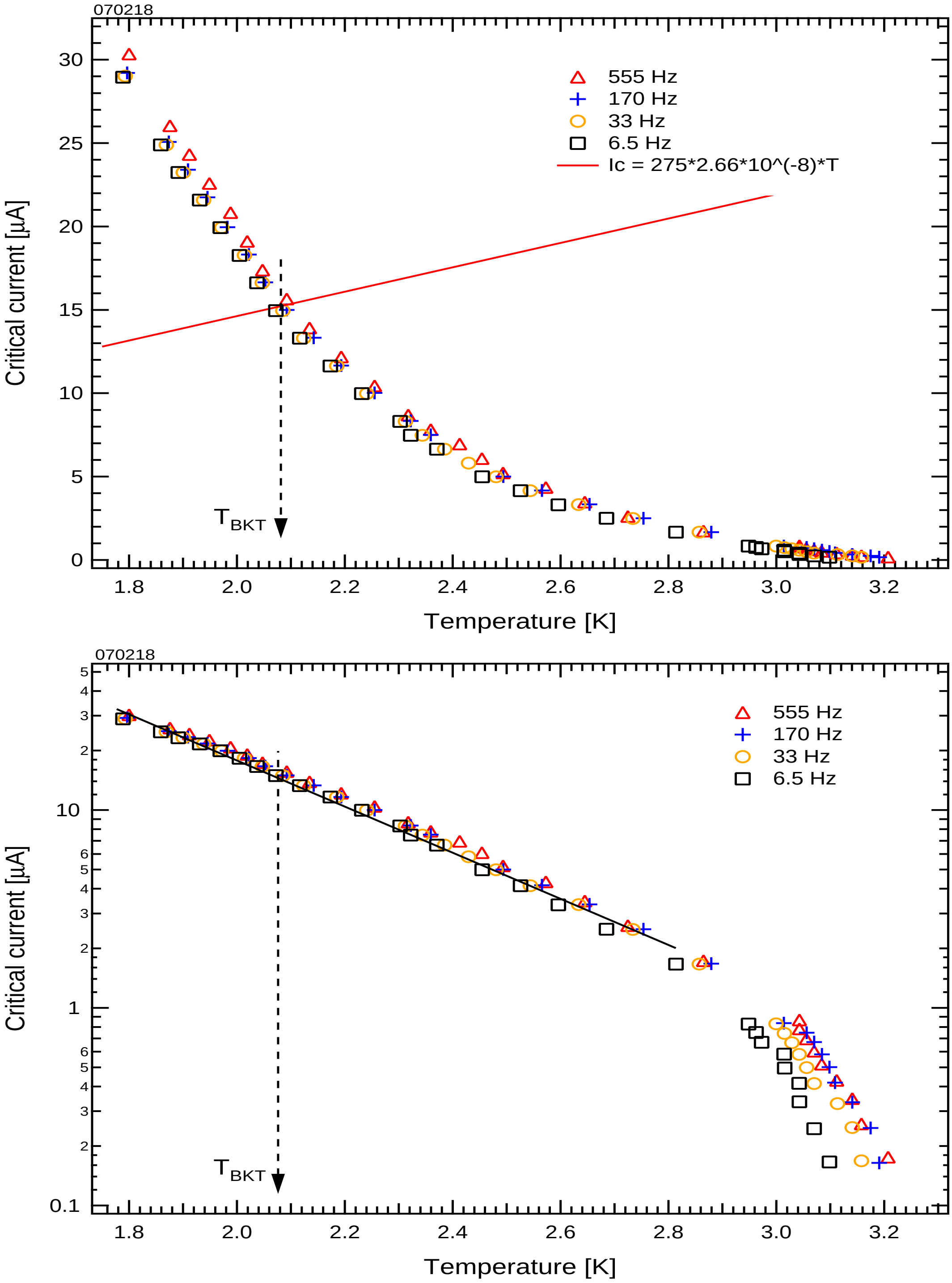

Figure 5.5: Array critical current (linear and exponential representations) extracted from the AC measurements, and BKT temperature prediction.

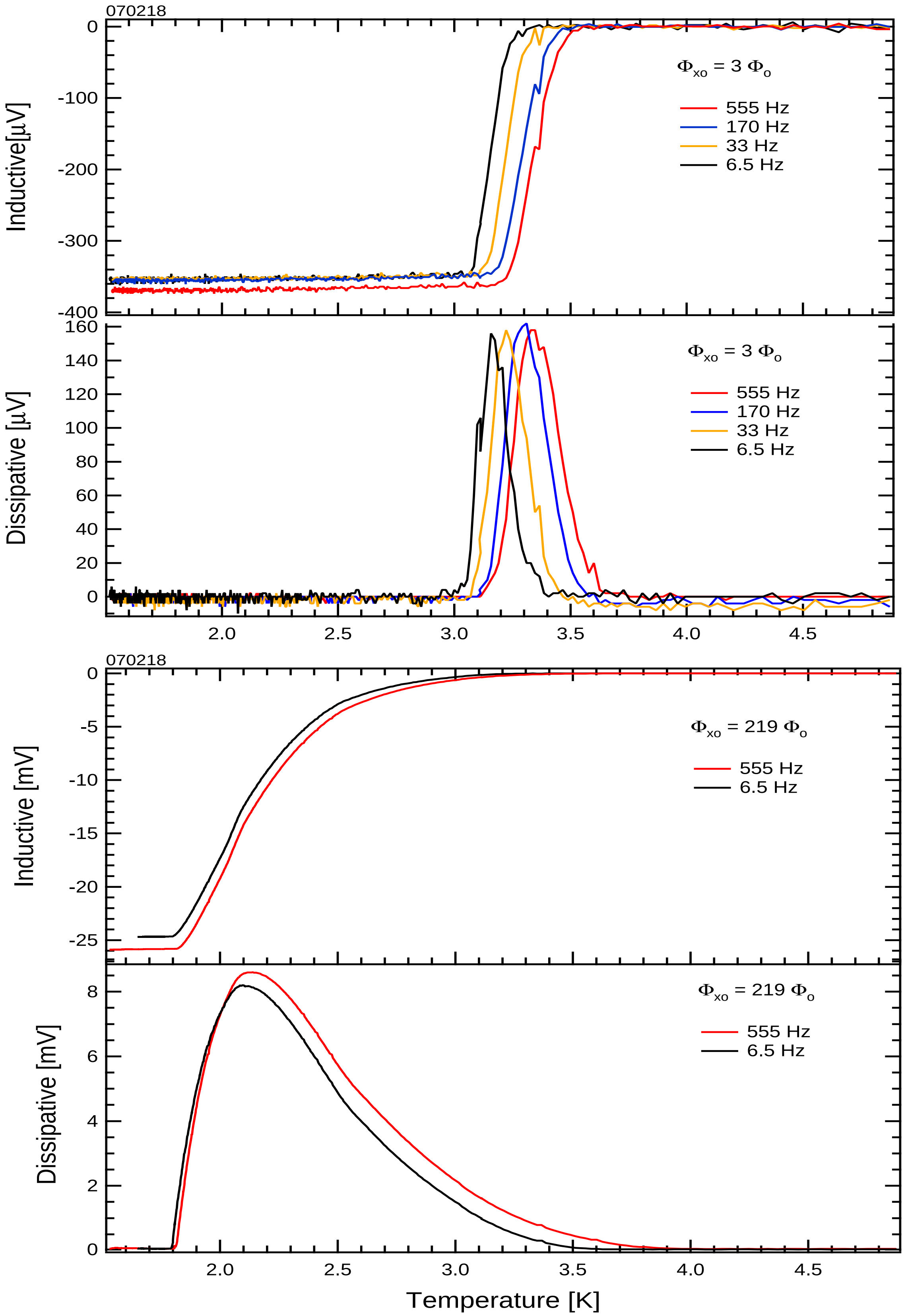

Figure 5.6: AC measurements on the array: temperature dependence of the dissipative component for different amplitudes and frequencies of the applied flux.

5.3 Conclusions

In this chapter, we performed DC and AC measurements on an array of Josephson junctions embedded in the same superconducting coil that was used for the device consisting of a single Josephson junction. We also observed that the sample undergoes a series of jumps in the total flux and a series of hysteresis cycles, which are sources of dissipation. A similar dynamic behavior to the single junction set up was found. The observed dissipation must therefore be attributed to the entry of quantum of flux into the superconducting coil through the Josephson array. As a result, the possible contribution to dissipation due to the unbinding of vortex-antivortex pairs, as predicted by the BKT theory, may be hidden by the aforementioned dissipation mechanism. In conclusion, no clear signature of the BKT transition was found.

Chapter 6

Conclusions

The conclusions of the present work are the following:

From an experimental point of view:

i) We was able to fabricate a Superconducting-Normal-Superconducting single Josephson junction, a series of Josephson junction or an array of Josephson junctions, embedded in a coplanar and gradiometric superconducting loop.

ii) We developed an original and very sensitive measurement technique which allows to perform on the same sample DC and AC measurements.

iii) We developed, for the first time, a contactless method to extract the critical current of a Josephson junction.

From a theoretical point of view:

iv) The thickness of the normal thin film has a great influence on the critical current, as predicted by Likharev's theory. In this way, one can tune the transition temperature of the SNS junction simply by changing such a thickness.

v) The origin of the dissipation observed in the AC measurements comes from a series of jumps in the flux and hysteresis cycles the sample undergoes when driven by an applied flux. This was qualitatively understood with a simple model on the basis of a graphical representation.

vi) A lumped circuit model which take into account a) the Josephson current, b) the fluxoid quantization, c) the dissipation via a resistance in parallel with the junction, and d) the self inductance of the loop where the junction is embedded is able to describe quantitatively the experimental data.

vii) No clear evidence of the BKT transition was found in the measurements performed on the sample consisting of an array of Josephson junctions. A similar behavior to the single junction case was observed.

6.1 Revelance of this work and future perspectives

The contactless technique developed in this work opens a new path to study the dynamics of Josephson junctions in a superconducting ring. Moreover, the possibility of extracting the critical current allows to test theoretical predictions based on microscopic models.

The results of this work may also give some insight into the interpretation of inductive measurements performed with the classical 'Two-Coils' technique on arrays of Josephson junctions. In particular, it was predicted theoretically that an array of Josephson junctions presents magnetization curves similar to the DC measurements shown in this thesis, with the two characteristic features: jumps and hysteresis loops, see Fig. 14 in the paper of Domínguez and José[1]. Therefore, this behavior could also be the responsible for the typical 'bump' observed in the dissipative component.

Similarly, this work may also give some insight into the interpretation of inductive measurements performed on high temperature superconductors where it is known both inter and intragranular josephson junctions are present[2].

Some possible directions for future experimental research are:

a) A systematic study of the dependence of the critical current in SNS junctions as a function of the normal metal film thickness.

b) The substitution of the normal metal by a ferromagnetic material (SFS junction) in order to study the transition from a 0-junction to a Π-junction as a function of the ferromagnetic film thickness[3].

c) Modify the fabrication process in order to fabricate a Superconducting-Insulator-Superconducting (SIS) or tunnel junction in order to perform very low temperature measurements to study quantum effects[4] on the dynamics of Josephson junctions in a superconducting ring.

d) To perform DC measurements with the classical 'Two-Coils' technique, on an array of Josephson junctions, in order to confirm or not the presence of jumps and hysteresis loops.

---

[1] D. Domínguez and J. V. José, *Magnetic and transport dc properties of inductive Josephson junction arrays*, Phys. Rev. B **53**, 11692 (1996).

[2] T. Ishida and H. Mazaki, *Superconducting transition of multiconnected Josephson network*, J. Appl. Phys. **52**, 6798 (1981). D. Domínguez, E. A. jagla and C. A. Balseiro, *Phenomenological theory of the paramagnetic Meissner efect*, Phys. Rev. Lett. **72**, 2773 (1994).

[3] A. Bauer, J. Bentner, M. Aprili, M. L. Della Rocca, M. Reinwald, W. Wegscheider and C. Strunk, *Spontaneous supercurrent induced by ferromagnetic π junctions*, Phys. Rev. Lett. **92**, 217001-1 (2004).

[4] J. R. Friedman, V. Patel, W. Chen, S. K. Tolpygo and J. E. Lukens, *Quantum superposition of distinct macroscopic states*, Nature **406**, 43 (6 July 2000).

Acknowledgments

First of all I would like to thank Prof. Piero Martinoli who gave me the opportunity to carry out this work in his research group and take advantage of the infrastructure and knowledge accumulated over the last twenty years. I appreciated his confidence in me and also the freedom he let me. Without his enthusiastic support this work would not be possible. I have no words to express him my gratitude for the great opportunity he opened me. Thanks a lot! Piero.

I am very grateful to Dr. Ricardo Théron, for his valuable suggestions and guidance. I appreciated his continuous support, his availability, his criticism and his always clear ideas. The discussions we had were very inspiring to me. Finally, I wish to thank him for his well humor and laugh, which made more easy to overcome all difficulties we found along the way.

I am also very grateful to Profs. Christophe Ballif and Jean-Marc Triscone for having accepted to be examiners of this thesis, and to Prof. Philipp Aebi for his help and support.

I am grateful to Prof. N. de Rooij and Dr. Luca Berdondini at the Sensors, Actuators and Microsystems Laboratory at the Institute of Microtechnology (Neuchâtel) for their hospitality and advices concerning the design of the mask.

I would like to thanks to Tobias Gresch and Fabrizio Giorgetta for the good maintenance of the PECVD equipment, and for their availability, despite the PhD work, to growth the silicon nitride films I needed.

I am very grateful to Flavio Ghezzi for his help with the English and his encouragement. I am also grateful to Verónica Marconi and Juan José Mazo for their useful advices concerning the numerical simulations.

Special thanks to the mechanical and electronics' workshops staff: Thierry Delhove, Daniel Varidel, Urs Bart, René Caillet, Christian Heche, Isidro Fernández, André Cornu and Jean Pierre Bourquin for their contagious passion and very useful collaboration.

I am also grateful to Anne-Marie Milo, Muriel Vallery-Mugely and Nicole Derendinger for their kindness and patience.

I would like to thank Alain, Mauro, Corsin, Claude, Hervé, Gunnar... and Laurent, with who I shared the office these last months, making more pleasant the end of this thesis.

I would like to remember here the people who influenced my orientation to study physics: my mathematics teacher at the Basic School (Plácido Martínez), my physics teacher (Javier Cantera) and my mathematics teacher (María Luisa Sánchez) at the High School of my natal village Borja (Zaragoza (Spain)). Thank you very much for your 'silent' task.

Finally, I would like to offer a very special thanks to my parents (Rafael and María Asunción), my brothers (Aito and Ana) and Lizzet, for their support and love.

This work has been supported by the Swiss Federal Office for Education and Science and the Swiss National Science Foundation, to whom I am very grateful.

Thanks God, I love you over everything.

Bibliography

Ambegaokar, V., B. I. Halperin, D. R. Nelson and E. D. Siggia, *Dynamics of superfluid films*, Phys. Rev. B **21**, 1806 (1980).

Anderson, G. S., Wm. N. Mayer and G. K. Wehner, *Sputtering of dielectrics by high frequency fields*, J. Appl. Phys. **33**, 2991 (1962).

Anderson, P. W., and J. M. Rowell, *Probable observation of the Josephson superconducting tunneling effect*, Phys. Rev. Lett. **10**, 230 (1963).

Ashcroft, N. W., and N. D. Mermin, *Solid State Physics*, Harcourt (1976).

Bardeen, J., L. N. Cooper and J. R. Schrieffer, *Theory of superconductivity*, Phys. Rev. **108**, 1175 (1957).

Barnat, E. V., D. Nagakura, P. I. Wang and T. M. Lu, *Real time resistivity measurements during sputter deposition of ultrathin copper films*, J. Appl. Phys. **91**, 1667 (2002).

Barone, A., and G. Paterno, *Physics and applications of the Josephson effect*, Wiley (1982).

Bauer, A., J. Bentner, M. Aprili, M. L. Della Rocca, M. Reinwald, W. Wegscheider and C. Strunk, *Spontaneous supercurrent induced by ferromagnetic π junctions*, Phys. Rev. Lett. **92**, 217001-1 (2004).

Ben-Jacob, E., and Y. Imry. *Response times of short Josephson junction and applications to rf SQUID's* , J. Appl. Phys.. **51(8)**, 4317 (1980).

Benz, S. P., and C. A. Hamilton, *Application of the Josephson effect to voltage metrology*, IEEE Proc. **92**, 1617 (2004).

Bloch, F., *Simple interpretation of the Josephson effect*, Phys. Rev. Lett. **21**, 1241 (1968).

Bloch, F., *Josephson effect in a superconducting ring*, Phys. Rev. B **2**, 109 (1970).

Blum, Y., A. Tsukernik, M. Karpovski and A. Palevski, *Critical current in Nb-Cu-Nb junctions with nonideal interfaces*, Phys. Rev. B **70**, 214501 (2004).

Butler, H. S., and G. S. Kino, *Plasma sheath formation by radio frequency fields*, The Physics of Fluids **6**, 1346 (1963).

Chapman, B., *Glow Discharge Processes*, John Wiley and Sons (1981)

Claassen, J. H., *Coupling considerations for SQUID devices*, J. Appl. Phys. **46**, 2268 (1975).

Coffin, J. G., *Extension of Maxwell's series formula for the mutual inductance of coaxial circles*, Phys. Rev. **2**, 65 (1913).

Cooper, L. N., *Superconductivity in the neighborhood of metallic contacts*, Phys. Rev. Lett. **6**, 689 (1961).

de Bruyn R. , *Macroscopic quantum phenomena in superconductors*, Superconductor Applications: SQUIDS and Machines, Edited by B.B. Schwartz and S. Foner, NATO Advanced Study Institutes Series, Vol. 1, Plenum Press (1976).

de Gennes, P. G., *Superconductivity in metals and alloys*, W. A. Benjamin (1968).

de Gennes, P. G., *Boundary effects in superconductors*, Rev. Mod. Phys. **36**, 225 (1964).

Delong, L. E., O. G. Symko and J. C. Wheatley, *Continuously operating ^{4}He evaporation refrigarator*, Rev. Sci. Instr. **42**, 147 (1971).

Domínguez D., and J. V. José, *Magnetic and transport dc properties of inductive Josephson junction arrays*, Phys. Rev. B **53**, 11692 (1996).

Domínguez, D., E. A. jagla and C. A. Balseiro, *Phenomenological theory of the paramagnetic Meissner efect*, Phys. Rev. Lett. **72**, 2773 (1994).

Doo, V. Y., D. R. Nichols and G. A. Silvey, *Method for depositing continuous pinhole free silicon nitride films and products produced thereby*, U.S Patent number 4089992 (1978).

Dubos, P., H. Courtois, B. Pannetier, F. K. Wilhelm, A. D. Zaikin and G. Schon, *Josephson critical current in a long mesoscopic SNS junction*, Phys. Rev. Lett. **63**, 064502 (2001).

Eilenberger, G., *Transformation of Gorkov's equation for type II superconductors into transport-like equations*, Z. Phys. **214**, 195 (1968).

Fazio R., and H. van der Zant, *Quantum phase transitions and vortex dynamics in superconducting networks*, Phys. Rep. **355**, 235 (2001).

Fiory, A. T., and A. F. Hebard, AIP Conf. Proc., **58**, 293 (1980).

Friedman, J. R., V. Patel, W. Chen, S. K. Tolpygo and J. E. Lukens, *Quantum superposition of distinct macroscopic states*, Nature **406**, 43 (6 July 2000).

Ginzburg, V. L., L. D. Landau *On the theory of superconductivity*, Zh. Eksperim. i Teor. Fiz. **20**, 1064 (1950).

Gor'kov, L. P., *Theory of superconducting alloys in a strong magnetic field near the critical temperature*, Sov. Phys. JETP **10**, 998 (1960).

Gradshteyn, I. S., and I. M. Ryzhik, *Table of Integrals Series and Products*, 4th ed., Academic Press (1965).

Grover, F-W., *Inductances Calculations*, Dover (1962).

Gubin, A. I., K. S. Il'in, S. A. Vitusevich, M. Siegel and N. Klein, *Dependence of magnetic penetration depth on the thickness of superconducting Nb thin films*, Phys. Rev. B **72**, 064503 (2005).

Halbritter, J., *On the oxidation and on the superconductivity of niobium*, Appl. Phys. A **43**, 1 (1987).

Hebard, A. F., and A. T. Fiory, *Evidence for the Kosterlitz-Thouless transition in thin superconducting aluminum films*, Phys. Rev. lett. **44**, 291, (1980).

Ishida, T., and H. Mazaki, *Superconducting transition of multiconnected Josephson network*, J. Appl. Phys. **52**, 6798 (1981).

Jackson, J. D., *Classical Electrodynamics*, 2nd ed., John Wiley & Son (1975).

Jang, S., S. M. Lee, and H. K. Baik, *Tantalum and niobium as a diffusion barrier between copper and silicon*, J. Mater. Sci. :Mater. Electr. **7**, 271 (1996).

Jeanneret, B., J. L. Gavilano, G. A. Racine, Ch. Leemann, and P.Martinoli, *Inductive conductance measurements in two-dimensional superconducting systems*, Appl. Phys. Lett. **55(22)**, 2336 (1989).

Josephson, B. D., *Possible new effects in superconductive tunnelling*, Phys. Lett. **1**, 251 (1962).

Kaufman, H. R., and S. M. Rossnagel, *Analysis of area-ratio effect for radio frequency diode*, J. Vac. Sci. Technol. A **6(4)**, 2572 (1988).

Kosterlitz, J. M., and D. J. Thouless, *Ordering, metastability and phase transitions in two-dimensional systems*, J. Phys. C **6**, 1181 (1973).

Kurkijarvi, J., *Intrinsic fluctuations in a superconducting ring closed with a Josephson junction*, Phys. Rev B **6**, 832 (1972).

Landau, L. D., E. M. Lifshitz, L. P. Pitaevskii, *Electrodynamics of Continuous Media*, 2nd ed., Pergamon Press (1984).

Lévy, L.-P., *Magnetism and superconductivity*, Springer-Verlag (1997).

Likharev, K. K., *Dynamics of Josephson junctions and circuits*, Gordon and Breach (1986).

Likharev, K. K., *The relation $J_s(\phi)$ for SNS bridges of variable thickness*, Sov. Tech. Phys. Lett. **2**, 12 (1976).

Likharev, K. K., *Superconducting weak links*, Rev. Mod. Phys. **51**, 101 (1979).

Ling, C. H., C. Y. Kwok and K. Prasad, *Silicon nitride films prepared by PECVD of $SiH_4/NH_3/N_2$ mixtures: some physical properties*, Jpn. J. Appl. Phys. **25**, 1490 (1986).

Lobb, C. J., D. Abraham and M. Tinkham, *Theoretical interpretation of resistive transition data from arrays of superconducting weak links*, Phys. Rev B **27**, 150 (1983).

London, F., *Superfluids (Vol. I)*, Dover (1961).

Makhlin, Y., G. Schon and A. Shnirman, *Quantum-state engineering with Josephson junction devices*, Rev. Mod. Phys. **73**, 357 (2001).

Martinoli, P. and Ch. Leemann, *Two dimensional Josephson junction arrays*, J. Low Temp. Phys. **118**, 699 (2000).

McCumber, D. E., *Effect of ac impedance on dc Voltage-Current characteristics of superconductor weak link junctions*, J. Appl. Phys. **39**, 3113 (1968).

Meissner, H., *Superconductivity of contacts with interposed barriers*, Phys. Rev. **117**, 672 (1962).

Minnhagen, P., *The two-dimensional Coulomb gas, vortex unbinding, and superfluid-superconducting films*, Rev. Mod. Phys. **59**, 1001 (1987).

Newrock, R. S., C. J. Lobb, U. Geigenmller and M. Octavio, *The two-dimensional physics of Josephson junction arrays*, Sol. State Phys. **54**, 253 (2000).

Panofski, W. K. H., M. Phillips, *Classical Electricity and Magnetism*, 2nd ed., Addison-Wesley (1962).

Silver, A. H., and J. E. Zimmerman, *Quantum transitions and loss in multiply connected superconductors*, Phys. Rev. Lett. **15**, 888 (1965).

Silver, A. H., and J. E. Zimmerman, *Quantum states and transitions in weakly connected superconducting rings*, Phys. Rev. **157**, 317 (1966).

Smith, D. L., *Thin Film Deposition*, McGraw Hill (1995)

Smith, H. J. T., and J. A. Blackburn, *Multiple quantum flux penetration in superconducting loops*, Phys. Rev. B **12**, 940 (1975).

Stewart, W. C., *Current-Voltage characteristics of Josephson junctions*, Appl. Phys. Lett. **12**, 277 (1968).

Théron, R., J. B. Simond, Ch. Leemann, H. Beck, P. Martinoli and P. Minnhagen, *Evidence for nonconventional vortex dynamics in an ideal two-dimensional superconductor*, Phys. Rev. Lett. **71**, 1246 (1993).

Thinkham, M. *Introduction to superconductivity*, McGraw-Hill (1996).

Usadel, K. D., *Generalized diffusion equation for superconducting alloys*, Phys. Rev. Lett. **25**, 507 (1970).

Zant, van der H., F. C. Fritschy, W. J. Elion, L. J. Geerligs and J. E. Mooij, *Field-induced superconductor-to-insulator transitions in Josephson-junction arrays*, Phys. Rev. Lett. **69**, 2971 (1992).

Vossen, J. L., and Werner Kern, *Thin Film Processes*, Academic Press (1978)

Wangsness, R. K., *Electromagnetic Fields*, 2nd ed., Wiley (1986).

Wilhelm, F., A. Zaikin and G. Schon, *SNS-model for the transport of a supercurrent in proximity wires*, J. Low Temp. Phys. **106**, 305 (1997).

Zaikin, A. D., and G. F. Zharkov, *Theory of wide dirty SNS junctions*, Sov. J. Low Temp. Phys. **7(3)**, 184 (1980).

Appendix A

Inductances Calculations

A.1 Introduction

In this annexe self and mutual inductances calculations of wire loops and coils are performed. We have decided to carry out them since they allow us to have an insight into the inductive measurement system we have used, and moreover, to make a quantitative analysis of the experimental data. On the other hand, these inductances calculations are necessary to find the geometrical dimensions that maximize the sensibility of the measurement system. They also are necessary if we search for some criteria to optimize the design parameters of the coplanar gradiometer in which the Josephson junction is embedded. We need to know, for instance, the numbers of turns and the geometry of this coplanar coil. In particular, some design questions arise: What is more suitable for this planar coil, using a narrow or a width pattern? How does one determine, exactly, the total self inductance of a coil?, and how can its value be decreased? To answer these questions is the aim of this annexe.

The analytical results of this chapter are well known[1], but not the details to arrive them. This is the reason we have made an effort to deduce them from scratch. Henceforth, we shall adopt the MKSA system of units[2].

A.2 Magnetic field of a circular wire loop

In this section we are going to obtain an analytical expression for the magnetic field produced by a circular filament. Since we are interested in calculating its self-inductance it will only be

[1]W. K. H. Panofski, M. Phillips, *Classical Electricity and Magnetism*, 2nd ed., Addison-Wesley (1962). R. K. Wangsness, *Electromagnetic Fields*, 2nd ed., Wiley (1986). J. D. Jackson, *Classical Electrodynamics*, 2nd ed., John Wiley & Son (1975). L. D. Landau, E. M. Lifshitz, L. P. Pitaevskii, *Electrodynamics of Continuous Media*, 2nd ed., Pergamon Press (1984).

[2]We remember that in the MKSA system $\mu = \mu_o(1+\chi)$, where $\mu_o = 4\pi \times 10^{-7}$ henry/m is the vacuum permeability; while $\mu = 1 + 4\pi\chi$, with a vacuum permeability of $\mu_o = 1$ in the CGS system. χ is the magnetic susceptibility.

necessary to consider the value of the magnetic field on the plane of the circular filament. We will start with the Biot-Savart law and a cylindrical coordinate system, see Fig.A.1(A).

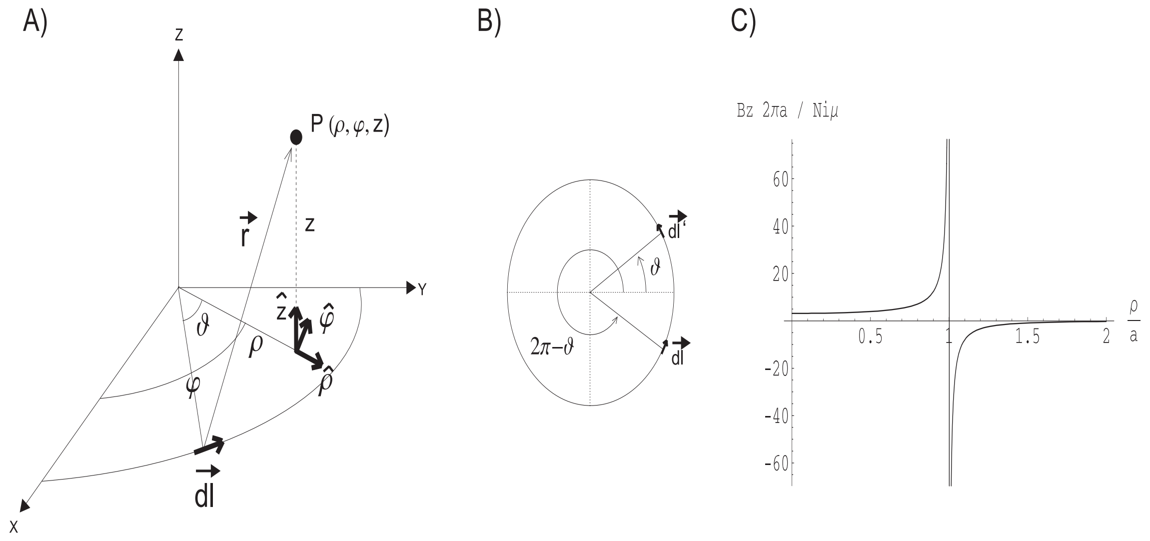

Figure A.1:

The magnetic field at $P \equiv (\rho, \varphi, z)$ produced by a current element $d\mathbf{l}$ is given by

$$d\mathbf{B}(\mathbf{r}) = \frac{\mu}{4\pi}\frac{i\, d\mathbf{l}\times\mathbf{r}}{r^3} \tag{A.1}$$

where $d\mathbf{l} = ad\theta\sin\theta\ \hat{\boldsymbol{\rho}} + ad\theta\cos\theta\ \hat{\boldsymbol{\varphi}}$ and $\mathbf{r} = \rho - a\cos\theta\ \hat{\boldsymbol{\rho}} + a\sin\theta\ \hat{\boldsymbol{\varphi}}$ with $|\mathbf{r}|^2 = z^2 + a^2 + \rho^2 - 2a\rho\cos\theta$, then we can write the components of the magnetic field like

$$dB_\rho = \frac{\mu_o}{4\pi}\, i\, \frac{za\cos\theta d\theta}{[z^2+a^2+\rho^2-2a\rho\cos\theta]^{3/2}} \tag{A.2}$$

$$dB_\varphi = -\frac{\mu_o}{4\pi}\, i\, \frac{za\sin\theta d\theta}{[z^2+a^2+\rho^2-2a\rho\cos\theta]^{3/2}} \tag{A.3}$$

$$dB_z = \frac{\mu_o}{4\pi}\, i\, \frac{(a^2-\rho a\cos\theta)\,d\theta}{[z^2+a^2+\rho^2-2a\rho\cos\theta]^{3/2}} \tag{A.4}$$

As expected for a cylindrical symmetry we have that, whatever the value of z, $dB_\varphi(d\mathbf{l}) = -dB_\varphi(d\mathbf{l}')$ for every couple of elements such shown in Fig.A.1(B) and hence $B_\varphi = 0$.

Since we are only interested in the magnetic field on the XY plane, ie, at $z = 0$, we can also write

$$B_\rho = 0 \qquad and \qquad B_z(\rho, z=0) = \frac{\mu_o}{4\pi}\, i\int_0^{2\pi}\frac{1-p\cos\theta}{[1+p^2-2p\cos\theta]^{3/2}}d\theta \qquad \text{, with } p = \frac{\rho}{a} \tag{A.5}$$

A.2.1 Analytical result

The above integral will be calculate in two parts:

$$\int_0^{2\pi} \frac{1 - p\cos\theta}{[1 + p^2 - 2p\cos\theta]^{3/2}} d\theta = \underbrace{\int_0^{2\pi} \frac{1}{[1 + p^2 - 2p\cos\theta]^{3/2}} d\theta}_{I} - \underbrace{\int_0^{2\pi} \frac{p\cos\theta}{[1 + p^2 - 2p\cos\theta]^{3/2}} d\theta}_{II}$$

with the following change of variable

$$\alpha = \frac{1}{2}(\theta - \pi) \qquad \Rightarrow \qquad \cos\theta = 2\sin^2\alpha - 1 \qquad d\alpha = \frac{1}{2}d\theta$$

we can rewrite the integral I as

$$I = \frac{1}{(1+p)^3} \int_{-\frac{\pi}{2}}^{\frac{\pi}{2}} \frac{2\, d\alpha}{\left[1 - \frac{4p}{(1+p)^2}\sin^2\alpha\right]^{\frac{3}{2}}} = \frac{4}{(1+p)^3} \int_0^{\frac{\pi}{2}} \frac{d\alpha}{\Delta^3}$$

where we have defined

$$\Delta = \sqrt{1 - k^2 \sin^2\alpha} \qquad \text{and} \qquad k^2 = \frac{4p}{(1+p)^2}$$

This last integral can be expressed as[3]

$$I = \frac{4}{(1+p)^3} \, \frac{1}{1-k^2} \, E\left(\frac{\pi}{2}, k\right) = \frac{4}{(1+p)(1-p)^2} \, E(k^2) \tag{A.6}$$

where $E(k^2)$ is the complete elliptic integral of second kind which is defined by

$$E(k^2) = E(\frac{\pi}{2}, k) = \int_0^{\frac{\pi}{2}} \sqrt{1 - k^2 \sin^2\alpha} \; d\alpha \tag{A.7}$$

Using the same change of variable than before we can calculate the integral II

$$II = \underbrace{\int_{-\frac{\pi}{2}}^{\frac{\pi}{2}} \frac{2p\sin^2\alpha \; 2d\alpha}{\left[(1+p)^2 - 4p\sin^2\alpha\right]^{\frac{3}{2}}}}_{III} - p \underbrace{\int_{-\frac{\pi}{2}}^{\frac{\pi}{2}} \frac{2d\alpha}{\left[(1+p)^2 - 4p\sin^2\alpha\right]^{\frac{3}{2}}}}_{I}$$

the last integral is identical to the integral I, hence it will only be necessary to calculate the integral III,

[3] I. S. Gradshteyn, I. M. Ryzhik, *Table of Integrals Series and Products*, 4th ed., Academic Press (1965).

$$III = \frac{4p}{(1+p)^3} \int_{-\frac{\pi}{2}}^{\frac{\pi}{2}} \frac{\sin^2\alpha \, d\alpha}{\left[1 - \frac{4p}{(1+p)^2}\sin^2\alpha\right]^{\frac{3}{2}}} = \frac{8p}{(1+p)^3} \int_0^{\frac{\pi}{2}} \frac{\sin^2\alpha}{\Delta^3} d\alpha$$

that can be expressed as[4]

$$\begin{aligned} III &= \frac{8p}{(1+p)^3} \left[\frac{1}{(1-k^2)k^2}\, E\left(\frac{\pi}{2}, k\right) - \frac{1}{k^2}\, F\left(\frac{\pi}{2}, k\right)\right] \\ &= 8p\left[\frac{1+p}{(1-p^2)4p} E(k^2) - \frac{1}{(1+p)4p} K(k^2)\right] \end{aligned} \tag{A.8}$$

where $F(k^2)$ is the complete elliptic integral of first kind which is defined by

$$K(k^2) = F(\frac{\pi}{2}, k) = \int_0^{\frac{\pi}{2}} \frac{d\alpha}{\sqrt{1 - k^2\sin^2\alpha}} \tag{A.9}$$

Finally, the integral we are looking for can be written as

$$\int_0^{2\pi} \frac{1 - p\cos\theta}{[1 + p^2 - 2p\cos\theta]^{3/2}} d\theta = I - II = I - (III - p\, I) = (1+p)I - III$$

and using Eq. A.6 and A.8 one has

$$\int_0^{2\pi} \frac{1 - p\cos\theta}{[1 + p^2 - 2p\cos\theta]^{3/2}} d\theta = \frac{2}{1-p}\, E(k^2) + \frac{2}{1+p}\, K(k^2) \tag{A.10}$$

In brief, inserting A.10 back into A.5, the magnetic field produced by a circular loop on his surface ($z = 0$) can be expressed as

$$B_z(p) = i\, \frac{\mu_o}{2\pi a} \left[\frac{1}{1-p}\, E(k^2) + \frac{1}{1+p}\, K(k^2)\right] \tag{A.11}$$

where

i is the current flowing through the filament.

μ_o is the vacuum permeability.

a is the radius of the loop. $p = \frac{\rho}{a}$ is the normalized distance from the center to the point where the magnetic field is calculated.

$E(k^2)$ and $K(k^2)$ are the complete elliptic integrals of second and first kind, respectively, that are expressed by equations A.7 and A.9.

Eq. A.11 is represented in Fig.A.1(C), which shows the dependence of the magnetic field in the plane $z = 0$ as a function of the distance from the center. We observe the divergence close to the wire and the asymptotic vanishing of the magnetic field outside the loop.

A.3 Self inductance of a circular wire loop

A current flowing through a circular filament produces a magnetic field throughout its surface, which can be written as

$$\phi = L\, i \qquad \Rightarrow \qquad L = \phi(i=1) \tag{A.12}$$

where L is the self inductance of the loop.

Hence, it is only necessary to know the magnetic flux through the circular filament (at the surface $z=0$) and evaluate it using Eq. A.11 by $\phi = \int_0^1 B_z(p)\, dS$. But, this integral diverge due to the divergence of the magnetic field near $p=1$ ($\rho = a$). However, if we consider that our filament will be a superconductor and therefor there will not be magnetic field inside, we can truncate the upper limit of the integral at $p = \frac{a-\delta}{a}$ ($\rho = a-\delta$), where 2δ is the diameter of the filament. In this way the divergence disappears. Hence, we only consider the contribution to the magnetic flux due to the magnetic field that exists outside the wire.

A.3.1 Numerical and analytical results

Using A.12 the self inductance can be written as

$$L = \phi(i=1) = \int_0^{\frac{a-\delta}{a}} \underbrace{B_z(p)}_{i=1}\; 2\pi a^2 p dp$$

and substituting $B_z(p)$ by A.11 one has

$$L = \mu_o a \underbrace{\int_0^{1-\frac{\delta}{a}} \left[\frac{1}{1-p}\, E(k^2) + \frac{1}{1+p}\, K(k^2)\right] p dp}_{C(\frac{\delta}{a})} = \mu_o a\; C(\frac{\delta}{a}) \tag{A.13}$$

The above integral can be evaluated numerically. Apart the factor $C(\frac{\delta}{a})$ which take into account the diameter of the wire, we have obtained the typical value $\sim \mu_o a$ used to estimate the self inductance of a loop of radius a.

We can compare Eq. A.13 with a known analytical expression (Eq. A.14) for the self inductance of a circular filament, see Panofsky-Phillips, Landau or Grover, *op.cit.*. In this case, the self inductance has been deduced taking into account the energy of the system, without using the Biot-Savart law, and it is written as

$$L = a\left[\mu_{ext}\left(ln\left(\frac{8a}{\delta}\right) - 2\right) + \frac{1}{4}\mu_{int}\right] \tag{A.14}$$

where μ_{ext} is the permeability of the external medium, μ_{int} is the permeability of the material, a is the radius of the loop and δ is the radius of the filament. In this way, the self inductance has two terms: an external contribution that only depends on the medium and the geometry, and an internal contribution that is independent of the geometry, depending only on the material. If the wire is superconducting we will have $\mu_{int} = 0$ (perfect diamagnetism) and in the vacuum we will write $\mu_{ext} = \mu_o = 4\pi\ 10^{-7}\ \frac{H}{m}$, hence

$$L = \mu_o\, a \left[ln\frac{8a}{\delta} - 2 \right] \tag{A.15}$$

In Fig. A.2 a representation of both A.13 and A.15 is shown. We observe that both equations give similar results. On the other hand, we note that the self inductance of a circular filament can be a factor ten greater than the typical approximation $L \sim \mu_o a$; smaller the ratio δ/a greater the difference. Finally, in Table A.3.1 some numerical values are shown for comparison.

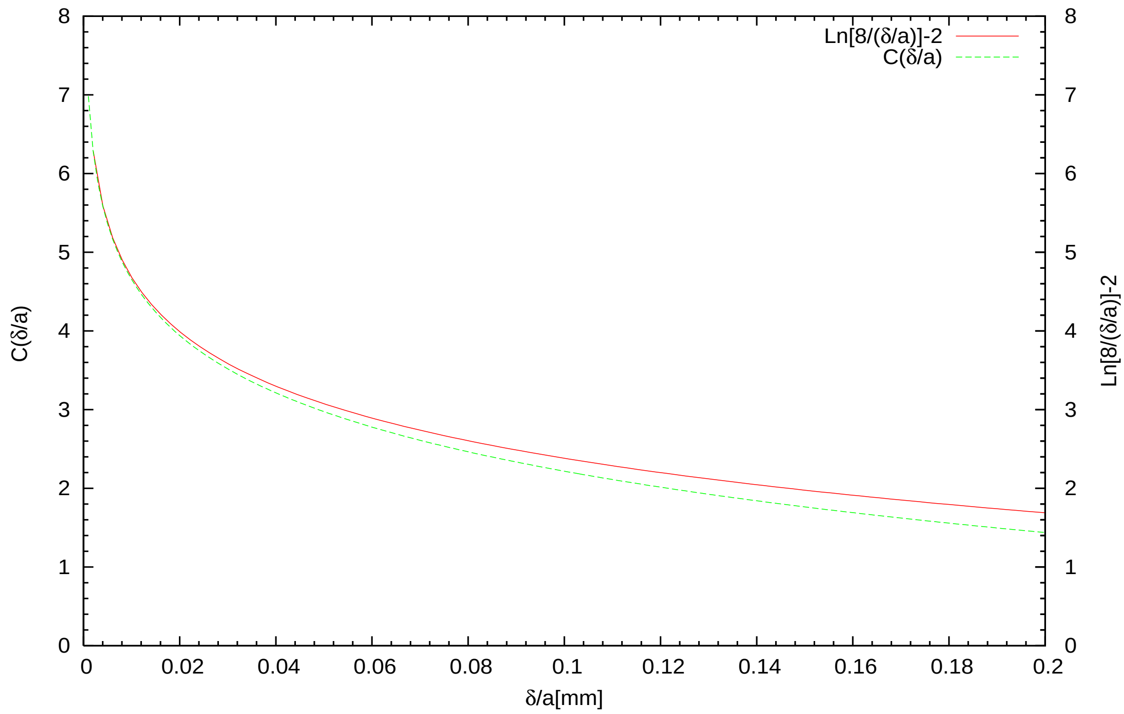

Figure A.2: Comparison between the factors in Eqs. A.13 and A.15 and their dependence in function of the ratio of filament radius δ to loop radius a.

2δ $[\mu m]$	1	20	160
$L = \mu_o a$ $[nH]$	1.256	1.256	1.256
$L = \mu_o a\, C(\frac{\delta}{a})$ $[nH]$	9.648	5.851	3.096
$L = \mu_o\, a \left[ln\frac{8a}{\delta} - 2\right]$ $[nH]$	9.651	5.887	3.274
$ln\frac{8a}{\delta} - 2$	7.68	4.68	2.60

Table A.1: Numerical comparison between the values of L for a loop of 1 mm radius and three different wire diameters (1,20 and 160 μm). On the first row, the known approximation for the self inductance L which do not consider the size of the wire is presented. On the second one, the value obtained from the Biot-Savart law and, on the third one, the value obtained from an energetic calculation, see Sec. A.3. On the fourth row the factor which take into account the diameter of the wire is presented.

A.3.2 Some notes about self inductances

The above results can be summarized as follows:

a) Smaller the ratio of the radius of the wire δ to the radius of the loop a, more important is the factor $C(\frac{\delta}{a})$ in determining the self inductance of the loop.

b) In order to decrease the self inductance of a loop, with fixed radius, it is necessary to increase the diameter of the wire.

Finally, we wish to add a critical remark on the applicability of Eq. A.15 to a superconducting loop. Before, we have pointed out that inside a superconductor $\mu_{int} = 0$ and then the self inductance reduces to Eq. A.15. But, we have also seen that this equation is equivalent to $\mu_o a\ C(\frac{\delta}{a})$ which takes into account the contribution due to the magnetic field created by the loop until the surface of the wire. Although it is true that inside the superconducting wire $\mu_{int} = 0$, it is not correct to suppose the magnetic field lines are not modified. On the contrary, due to the exclusion of the magnetic field, a greater density of field lines is expected inside the loop, and therefore a greater value of the self inductance than the predicted by Eq. A.13 or A.15.

A.4 Mutual inductance between two coaxial circular wire loops

In order to calculate the mutual inductance between two coaxial loops, see Fig. A.3, we use the Neumann's formula[4],

[4] J. D. Jackson, *Classical Electrodynamics*, 2nd ed., John Wiley & Son (1975).

$$L_{12} = \frac{\mu_o}{4\pi} \oint_{C_1} \oint_{C_2} \frac{d\mathbf{l} \cdot d\mathbf{l}'}{r}, \tag{A.16}$$

without lack of generality let us suppose both currents are in the same sense. One has

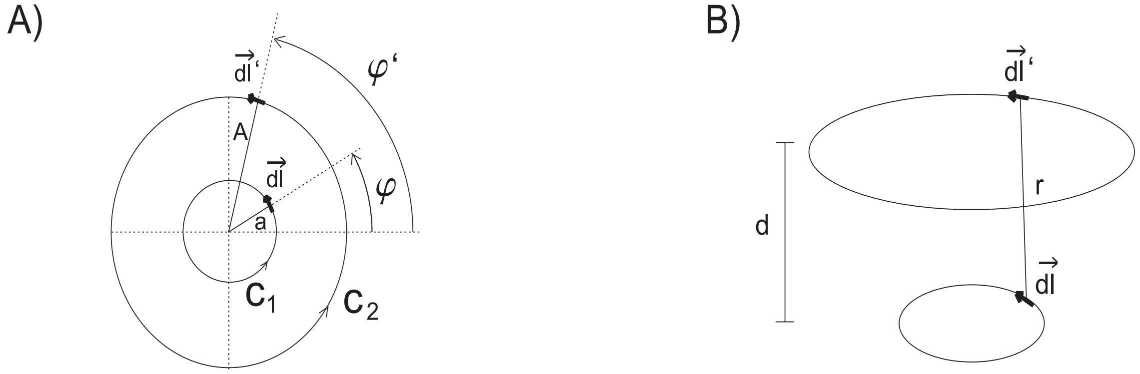

Figure A.3: Geometry used for the calculation of the mutual inductance between two coaxial loops. Fig. A) is the projection of B).

$$\begin{aligned} d\mathbf{l} \cdot d\mathbf{l}' &= dldl' \cos(\phi' - \phi) = aA \cos(\phi' - \phi) d\phi d\phi' \\ r^2 &= a^2 + A^2 - 2aA \cos(\phi' - \phi) + d^2 \end{aligned} \tag{A.17}$$

where a and A are the radii of the circular filaments and d is the distance betwen them.

(1) If one interchanges a by A in expressions A.17 nothing changes, *i.e.*, $L_{12} = L_{21}$.

(2) If both currents were in opposed senses, we should write

$$d\mathbf{l} \cdot d\mathbf{l}' = dldl' \cos[\pi - (\phi' - \phi)] = -dldl' \cos(\phi' - \phi), \;\; ie, \;\; L_{12}^{\uparrow\downarrow} = -L_{12}^{\uparrow\uparrow}$$

Inserting A.17 in A.16 one has

$$L_{12}^{\uparrow\uparrow} = \frac{\mu_o}{4\pi} \int_{\phi=0}^{2\pi} \int_{\phi'=0}^{2\pi} \frac{aA \cos(\phi' - \phi) \; d\phi d\phi'}{\sqrt{a^2 + A^2 - 2aA \cos(\phi' - \phi) + d^2}}$$

It is convenient now to make the following change of variables

$$\theta = \frac{1}{2}[(\phi' - \phi) - \pi] \quad \Rightarrow \quad \cos(\phi' - \phi) = 2 \sin^2 \theta - 1, \text{ and } d\theta = \frac{1}{2} d\phi' \; (\phi \; fixed)$$

and then $L_{12}^{\uparrow\uparrow}$ can be rewritten as

$$L_{12}^{\uparrow\uparrow} = \frac{\mu_o}{4\pi} aA \int_0^{2\pi} \underbrace{\left[\int_{-\frac{\phi}{2}-\frac{\pi}{2}}^{-\frac{\phi}{2}+\frac{\pi}{2}} \frac{2\sin^2\theta - 1}{\sqrt{a^2 + A^2 - 2aA(2\sin^2\theta - 1) + d^2}} 2d\theta \right]}_{I} d\phi \tag{A.18}$$

The integral I is calculated in the following Section.

A.4.1 Analytical result

We calculate I in two parts:

$$\begin{aligned} I &= \underbrace{\left[\int_{-\frac{\phi}{2}-\frac{\pi}{2}}^{-\frac{\phi}{2}+\frac{\pi}{2}} \frac{4\sin^2\theta}{\sqrt{(a+A)^2 - 4aA\sin^2\theta + d^2}} d\theta \right]}_{II} \\ &\quad - \underbrace{\left[\int_{-\frac{\phi}{2}-\frac{\pi}{2}}^{-\frac{\phi}{2}+\frac{\pi}{2}} \frac{2}{\sqrt{(a+A)^2 - 4aA\sin^2\theta + d^2}} d\theta \right]}_{III} \end{aligned}$$

a) Calculate of integral II.

$$II = \frac{4}{\sqrt{(a+A)^2 + d^2}} \int_{-\frac{\phi}{2}-\frac{\pi}{2}}^{-\frac{\phi}{2}+\frac{\pi}{2}} \frac{\sin^2\theta}{\sqrt{1 - k^2\ \sin^2\theta}} d\theta$$

with $k^2 = \frac{4aA}{(a+A)^2+d^2}$.

If we do the change of variables $\theta' = \theta + \frac{\pi}{2}$ one has

$$II = \frac{4}{\sqrt{(a+A)^2 + d^2}} \int_{-\frac{\phi}{2}}^{-\frac{\phi}{2}+\pi} \frac{\sin^2\theta'}{\sqrt{1 - k^2\ \sin^2\theta'}} d\theta'$$

this last integral can be written as (see Gradshteyn tables)

$$\begin{aligned} &= \frac{4}{\sqrt{(a+A)^2 + d^2}} \left[\frac{1}{k^2} F(\theta', k) - \frac{1}{k^2} E(\theta', k) \right]_{-\frac{\phi}{2}}^{-\frac{\phi}{2}+\pi} \\ &= \frac{8}{\sqrt{(a+A)^2 + d^2 k^2}} \Big(K(k^2) - E(k^2) \Big) \end{aligned} \tag{A.19}$$

as expected, this expression is independent of ϕ. In order to obtain it we have used the following relations (see Gradshteyn tables)

$$\begin{aligned} F\left(\frac{-\phi}{2}+\pi,k\right) &= 2K(k^2)-F\left(\frac{\phi}{2},k\right) \\ E\left(\frac{-\phi}{2}+\pi,k\right) &= 2E(k^2)-E\left(\frac{\phi}{2},k\right) \\ F\left(\frac{-\phi}{2},k\right) &= F\left(\frac{\phi}{2},k\right) \\ E\left(\frac{-\phi}{2},k\right) &= E\left(\frac{\phi}{2},k\right) \end{aligned} \tag{A.20}$$

where $E(k^2)$ and $K(k^2)$ are the complete elliptic integrals of second and first kind, respectively, which are expressed by A.7 and A.9.

b) Calculate of integral III.

$$III=\frac{2}{\sqrt{(a+A)^2+d^2}}\int_{-\frac{\phi}{2}}^{-\frac{\phi}{2}+\pi}\frac{1}{\sqrt{1-k^2\ \sin^2\theta'}}\,d\theta'$$

this last integral can be written as (see Gradshteyn tables)

$$\begin{aligned} &= \frac{2}{\sqrt{(a+A)^2+d^2}}\left[F(\theta',k)-E(\theta',k)\right]_{-\frac{\phi}{2}}^{-\frac{\phi}{2}+\pi} \\ &= \frac{4}{\sqrt{(a+A)^2+d^2}}K(k^2) \end{aligned} \tag{A.21}$$

as expected, this expression also is independent of ϕ and in order to obtain it we have used the relations A.20 once more.

Finally, we can write the expression A.18 for $L_{12}^{\uparrow\uparrow}$ as

$$L_{12}^{\uparrow\uparrow}=\frac{\mu_o aA}{2}\,(II-III)$$

and using A.19 and A.21 we obtain an analytical expression for the mutual inductance between two coaxial circular filaments of radii a and A separated a distance d

$$L_{12}^{\uparrow\uparrow}=\mu_o\sqrt{aA}\left[\left(\frac{2}{k}-k\right)\ K(k^2)-\frac{2}{k}\ E(k^2)\right] \tag{A.22}$$

where

$$k^2=\frac{4aA}{(a+A)^2+d^2}$$

This expression was first calculated by J.C. Maxwell in 1907[5].

A.5 Comparison with experiment

In this section the mutual inductance between two coaxial loops is measured, and the result is compared to the value predicted by Eq. A.22.

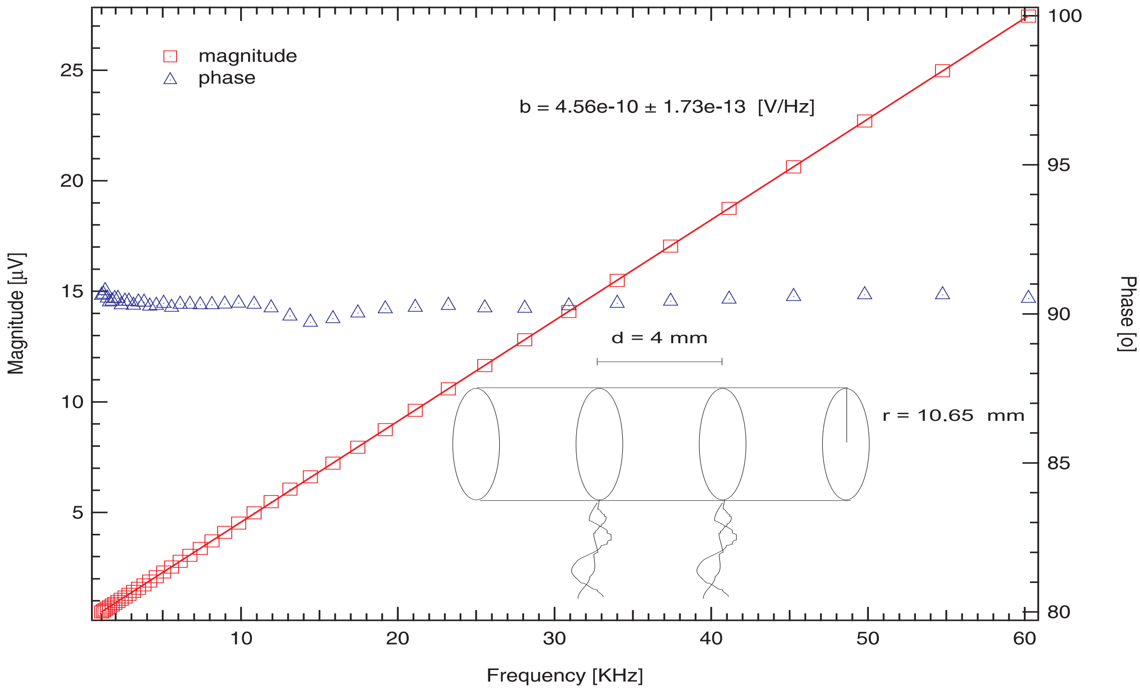

Figure A.4: The figure inside shows the geometrical configuration used for measuring the mutual inductance between two loops. The plot represents the frequency dependence of both the magnitude and phase difference measured by a lock-in technique. The slope of the line is related to the mutual inductance between both loops.

The geometrical configuration used to perform the measurement is shown inside the Fig. A.4. Both filaments consist of 100 μm diameter copper wires placed in respective grooves of 100 μm in depth on a cylinder of 21.5 mm in diameter. The distance between both loops is 4 mm.

The measurement has been performed with a lock-in technique. One of the loops is driven from the lock-in reference output at a fixed frequency and amplitude, and the signal from the other loop is fed into the input of the lock-in, which measures both its magnitude and phase difference between the signals in the loops.

[5]J. G. Coffin, *Extension of Maxwell's series formula for the mutual inductance of coaxial circles*, Phys. Rev. **2**, 65 (1913)

The amplitude of the driven signal was fixed at 5 V and the output impedance was of 1 $K\Omega$. In this way, a frequency sweep ranging from 1 KHz to 60 KHz has been performed.

We can express the drive current through the, let us say, loop 1 like

$$I_1 = I_{01} sin(\omega t) = \frac{V_{01}}{R} sin(2\pi\nu t), \tag{A.23}$$

where $R = 1\ K\Omega$ is the output impedance of the driven reference signal and $V_{01} = 5.0\ V$ its amplitude. The induced voltage in the other loop, let us say loop 2, will be

$$V_2 = -\frac{d\phi_{21}}{dt} = L_{21}\frac{dI_1}{dt} = L_{21}\frac{V_{01}}{R}\ 2\pi\nu\ cos(2\pi\nu t) = L_{21}\frac{V_{01}}{R}\ 2\pi\nu\ sin(2\pi\nu t + \frac{\pi}{2}). \tag{A.24}$$

where L_{21} is the mutual inductance between both loops. Hence, the magnitude and phase difference of the signal detected by the lock-in can be written as

$$magnitude = V_{02} = L_{21}\frac{V_{01}}{R}2\pi\nu = b\ \nu \qquad phase\ \ difference = \frac{\pi}{2}. \tag{A.25}$$

where

$$b = 2\pi L_{21}\frac{V_{01}}{R} \tag{A.26}$$

is the slope of the magnitude vs. frequency linear dependence.

As expected, we obtain a lineal relation for the frequency dependence of the magnitude measured by the lock-in, and a ninety degree phase difference, see Fig. A.4. Finally, from the measured slope $b = 4.56 \times 10^{-10}\ V/Hz$ and using A.26 we obtain for the mutual inductance

$$L_{21} = \frac{b}{2\pi\frac{V_{01}}{R}} = \frac{4.56 \times 10^{-10}}{2\pi\ (5 \times 10^{-3})} = 1.45 \times 10^{-8}\ H, \tag{A.27}$$

which has to be compared with the theoretical value $L_{21} = 1.51 \times 10^{-8}\ H$ that one obtains using the equation A.22, where the elliptic integrals has been evaluated using Mathematica.

Appendix B

Photolithography recipes

All the processes were carried out in a clean room. The temperature and relative humidity of the room were controlled to working values of approx. 20^{o}C and 65%, respectively, which are very important parameters for success and reproducibility (we observed for instance that working at 25^{o}C and 45%RH the resist stuck to the mask).

B.1 Substrate cleaning

Substrates consist of sapphire discs (Al_2O_3) 25.4 mm in diameter and 0.5 mm in thickness[1].

1) Ultrasound in Acetone (ACE) bath for 180s.
2) Ultrasound in Isopropyl alcohol (IPA) for 180s.
3) Rinse in running DI water for 60s.
4) Blow dry with N_2.
5) Bake 120 seconds @ 125^{o}C to remove adsorbed water, and allow to cool.

Acetone removes organic impurities but it high evaporation rate requires a subsequent cleaning step in another solvent as IPA in order to avoid striations on the substrate. The above simple cleaning procedure has been sufficient for us.

[1] www.comadur.com

B.2 Processing for the negative (image reversal) resist

We remember that a negative resist[2] *remains in the exposed areas after developing (briefly, if light then ↓).* Notice that if the resist bottle is refrigerated, it is obligatory to adapt the bottle to room temperature some hours before opening it, otherwise condensed water may deteriorate the resist.

Spin-coat:

1) Blow the substrate with N_2 to particle removal.

2) Center the substrate on the spin-coater and with a Pasteur pipette put approx. 20 drops of resist on it.

3) After 15-20 seconds, spin-coat the resist to 2000 RPM for 7 seconds followed by 4000 RPM for 33 seconds. Under these conditions the final thickness was approx. $3\mu m$.

4) Keep the substrate for 10 minutes at room temperature to let the solvent evaporates slowly.

Soft-bake:

5) Bake the coated substrate 2 minutes @ 100^oC on the hotplate to remove the solvent, and allow to cool.

Edge bead removal[3]:

6) Center the substrate on the spin-coater and while spinning it to 2000 RPM just put two drops on its border. Blow dry with N_2 and wait for two minutes.

Exposure:

7) Place the corresponding mask and the substrate on the mask aligner[4], and blow with N_2 on the sample. Use hard contact. Exposure for 5 seconds and keep the coated substrate at room temperature for 20 minutes. In this delay time nitrogen, generated during exposure, will diffuse out the resist.

Reversal bake:

8) Bake the coated substrate 2 minutes @ 125^oC on the hotplate and keep the substrate for 10 minutes at room temperature for rehydration.

---

[2]We have used the TI 35ES resist from www.microchemicals.com.

[3]During the spinning of photoresist on a sample, there is a build-up of material at the substrate edges. In order to avoid diffraction problems using contact lithography, it is necessary to have intimate contact between the sample and the mask. Therefore, the edge bead must be removed prior to pattern exposure. We have used for it the AZ EBR solvent from www.microchemicals.com.

[4]We have used the AL4-1 mask aligner from www.evgroup.com. In the hard contact mode the substrate is pushed up to the mask by N_2, while in the vacuum contact mode the air between the mask and the substrate is evacuated. The intensity of the Hg light source (i-line) is 12 mW/cm^2.

Flood exposure:

9) Exposure the coated substrate for 80 second without a mask.

Development:

10) Develop in AZ 826MIF developer (1:1 DI water) for approx. 2 minutes. Soak in a DI water bath immediately to stop the development and rinse for 60 seconds in DI water. Blow dry with N_2.

11) Check under the microscope.

B.3 Processing for the positive resist

We remember that a positive resist[5] *is removed away from the exposed areas after developing (briefly, if light then ↑).* Notice that if the resist bottle is refrigerated, it is obligatory to adapt the bottle to room temperature some hours before opening it, otherwise condensed water may deteriorate the resist.

Spin-coat:

1) Blow the substrate with N_2 to particle removal.

2) Center the substrate on the spin-coater and with a Pateur pipette put approx. 20 drops of resist on it.

3) After 15-20 seconds, spin-coat the resist to 2000 RPM for 7 seconds followed by 4000 RPM for 33 seconds. Under these conditions the final thickness was approx. $1\mu m$.

4) Keep the substrate for 3 minutes at room temperature to let the solvent evaporates slowly.

Soft-bake:

5) Bake the coated substrate 1 minutes @ 90^oC on the hotplate to remove the solvent, and allow to cool.

Edge bead removal:

6) Center the substrate on the spin-coater and while spinning it to 2000 RPM just put two drops on its border. Blow dry with N_2 and wait for two minutes.

Exposure:

7) Place the corresponding mask and the substrate on the mask aligner, and blow with N_2 on the sample. Use hard and vacuum contact. Exposure for 1 minute and keep the coated substrate at room temperature for 3 minutes.

[5]We have used the AZ MIR 701 resist from www.microchemicals.com.

Post Exposure Bake:

8) Bake the coated substrate 1 minutes @ 110^{o}C on the hotplate and keep the substrate for 4 minutes at room temperature for rehydration.

Development:

9) Develop in AZ 726MIF developer for 5 seconds. Soak in a DI water bath immediately to stop the development and rinse for 60 seconds in DI water. Blow dry with N_2.

10) Check under the microscope.